Regulation of platelet biogenesis in the native and myeloablated bone marrow niche

***

Die Regulation der Thrombozytenbiogenese im nativen und myeloablatierten Knochenmark

Doctoral thesis for a doctoral degree
at the Graduate School of Life Sciences,
Julius-Maximilians-Universität Würzburg,
Section: Biomedicine

submitted by

Kristina Mott

from Wertheim, Germany

Würzburg, 2022

Members of the Thesis Committee

Chairperson: Prof. Dr. Carmen Villmann

Primary Supervisor: Prof. Dr. Harald Schulze

Supervisor (Second): Prof. Dr. Katrin G. Heinze

Supervisor (Third): Prof. Dr. Süleyman Ergün

Summary

Megakaryocytes (MKs) are the largest cells of the hematopoietic system and the precursor cells of platelets. During proplatelet formation (PPF) bone marrow (BM) MKs extent large cytoplasmic protrusions into the lumen of sinusoidal blood vessels. Under homeostatic conditions PPF occurs exclusively in the direction of the sinusoid, while platelet generation into the marrow cavity is prevented. So far, the mechanisms regulating this process *in vivo* are still not completely understood, especially when PPF is deregulated during disease. This thesis investigated the mechanisms of PPF in native BM and after myeloablation by total body irradiation (TBI).

First, we have identified a specialized type of BM stromal cells, so called CXCL12-abundant reticular (CAR) cells, as novel possible regulators of PPF. By using complementary high-resolution microscopy techniques, we have studied the morphogenetic events at the MK/vessel wall interface in new detail, demonstrating that PPF formation preferentially occurs at CAR cell-free sites at the endothelium.

In the second part of this thesis, we analyzed the processes leading to BM remodeling in response to myeloablation by TBI. We used confocal laser scanning microscopy (CLSM) to study the kinetic of radiation-triggered vasodilation and mapped extracellular matrix (ECM) proteins after TBI. We could demonstrate that collagen type IV and laminin α5 are specifically degraded at BM sinusoids. At the radiation-injured vessel wall we observed ectopic release of platelet-like particles into the marrow cavity concomitantly to aberrant CAR cell morphology, suggesting that the balance of factors regulating PPF is disturbed after TBI. ECM proteolysis is predominantly mediated by the matrix metalloproteinase MMP9, as revealed by gelatin-zymography and by a newly established BM *in situ* zymography technique. In transgenic mice lacking MMP9 vascular recovery was delayed, hinting towards a role of MMP9 in vessel reconstitution after myeloablation.

In a third series of experiments, we studied the irradiated BM in the context of hematopoietic stem cell transplantation (HSCT). By using mice as BM donors that ubiquitously express the fluorescent reporter protein dsRed we tracked engraftment of donor cells and especially MKs in the recipient BM. We found a distinct engraftment pattern and cluster formation for MKs, which is different from other blood cell lineages.

Finally, we assessed platelet function after TBI and HSCT and were the first to demonstrate that platelets become massively hyporeactive, particularly upon stimulation of the collagen receptor GPVI.

In summary, our findings shed light on the processes of PPF during health and disease which will help to develop treatments for aberrant thrombopoiesis.

Zusammenfassung

Megakaryozyten (MKs) sind die größten Zellen des hämatopoetischen Systems und die Vorläuferzellen der Blutplättchen. Während der Ausbildung von Proplättchen schnüren MKs im Knochenmark (KM) große zytoplasmatische Ausläufer in das Lumen der sinusoidalen Blutgefäße ab. Unter homöostatischen Bedingungen erfolgt die Proplättchenbildung ausschließlich in Richtung der Sinusoide, während die Thrombozytenbildung in die Knochenmarkkavität verhindert wird. Bislang sind die Mechanismen, die diesen Prozess *in vivo* steuern, noch nicht vollständig aufgeklärt insbesondere, wenn die Thrombozytenbiogenese unter Krankheitsbedingungen dereguliert ist. In dieser Arbeit wurden die Mechanismen der Thrombopoese im nativen Knochenmark und nach Myeloablation durch Ganzkörperbestrahlung (*total body irradiation*, TBI) untersucht.

Zunächst haben wir einen spezialisierten Typ von KM-Stromazellen, die sog. *CXCL12-abundant reticular* (CAR) Zellen, als neue mögliche Regulatoren der Proplättchenbildung identifiziert. Durch den Einsatz komplementärer hochauflösender Mikroskopietechniken haben wir die morphogenetischen Vorgänge an der Schnittstelle zwischen MKs und Gefäßwand genauer untersucht und gezeigt, dass die Generierung von Proplättchen bevorzugt an CAR-Zell-freien Stellen am Endothel stattfindet.

Im zweiten Teil dieser Arbeit analysierten wir die Prozesse, die zum Knochenmarkumbau nach Myeloablation durch TBI führen. Mit Hilfe von konfokaler Laser-Scanning-Mikroskopie untersuchten wir die Kinetik der strahleninduzierten Vasodilatation und kartierten die extrazelluläre Matrix (EZM) Proteine nach TBI. So konnten wir zeigen, dass Kollagen Typ IV und Laminin α5 spezifisch an den Knochenmarksinusoiden abgebaut werden. An der strahlengeschädigten Gefäßwand beobachteten wir die ektope Freisetzung plättchenartiger Partikel in die Knochenmarkkavität, die mit einer abnormalen CAR-Zellmorphologie einherging. Dies weist darauf hin, dass das Gleichgewicht der Faktoren, die die gerichtete Proplättchenbildung regulieren, nach TBI gestört ist. Die EZM-Proteolyse wird vor allem durch die Matrix-Metalloproteinase MMP9 vermittelt, was durch Gelatine-Zymographie und durch eine neu etablierte *in situ* Zymographie-Technik für das Knochenmark nachgewiesen wurde. Bei transgenen Mäusen, die defizient für MMP9 sind, war die Regeneration der Vaskulatur verzögert, was auf eine Rolle von MMP9 bei der Gefäßrekonstitution nach Myeloablation hindeutet.

In einer dritten Versuchsreihe untersuchten wir das bestrahlte KM im Rahmen einer hämatopoetischen Stammzelltransplantation (HSZT). Mit Hilfe von Mäusen als KM-Spender, die ubiquitär das fluoreszierende Reporterprotein dsRed exprimieren, verfolgten wir das Anwachsen von Spenderzellen und insbesondere von MKs im Empfängerknochenmark. Wir beobachteten ein eindeutiges Muster bzw. Clusterbildung für anwachsende MKs, die sich von anderen Blutzelllinien unterschied.

Schließlich untersuchten wir die Funktion von Thrombozyten nach TBI und HSZT und konnten als erste zeigen, dass Thrombozyten eine massive Hyporeaktivität ausbilden, insbesondere nach Stimulation des Kollagenrezeptors GPVI.

Zusammenfassend geben unsere Ergebnisse Aufschluss über die Prozesse der Thrombopoese im nativen und pathologischen Knochenmark, was zur Entwicklung von Therapien zu Behandlung von defekter Thrombozytenbiogenese beitragen wird.

Contents

1. Introduction

1.1. Hematopoiesis and the HSC niche

The bone marrow (BM) is the main hematopoietic compartment in adult mammals. It constitutes a unique microenvironment referred to as “niche” for the precursor cells of all blood cells, the hematopoietic stem cells (HSCs). Pluripotent HSCs have the potential for self-renewal i.e., they are able to divide without differentiation, thereby generating new HSCs to ensure life-long hematopoiesis. The classical model of murine hematopoietic cell maturation describes a hierarchical differentiation process that begins with pluripotent long-term HSCs, that differentiate into multipotent progenitors (MPPs) and then either into common lymphoid progenitors (CLPs) or common myeloid progenitors (CMPs). While CLPs constitute the lymphoid blood cell lineage, CMPs give rise to the precursor cells of the myeloid lineage consisting of granulocyte macrophage progenitors (GMP) and megakaryocyte erythroid progenitors (MEPs) (Fig. 1). However, during the last years this model has been increasingly revised, as reviewed in [1], by the discovery of lineage-primed MPP subpopulations, suggesting that fate decisions occur already early during hematopoiesis (Fig. 1B). Recently, a self-renewing, myeloid-restricted progenitor population with the ability to bypass the MPP pathway has been identified by tracing single cells during hematopoietic cell differentiation (Fig. 1C) [2]. These findings demonstrate that our current understanding of hematopoiesis is still incomplete and that new insights contribute to a revision of the classical model.

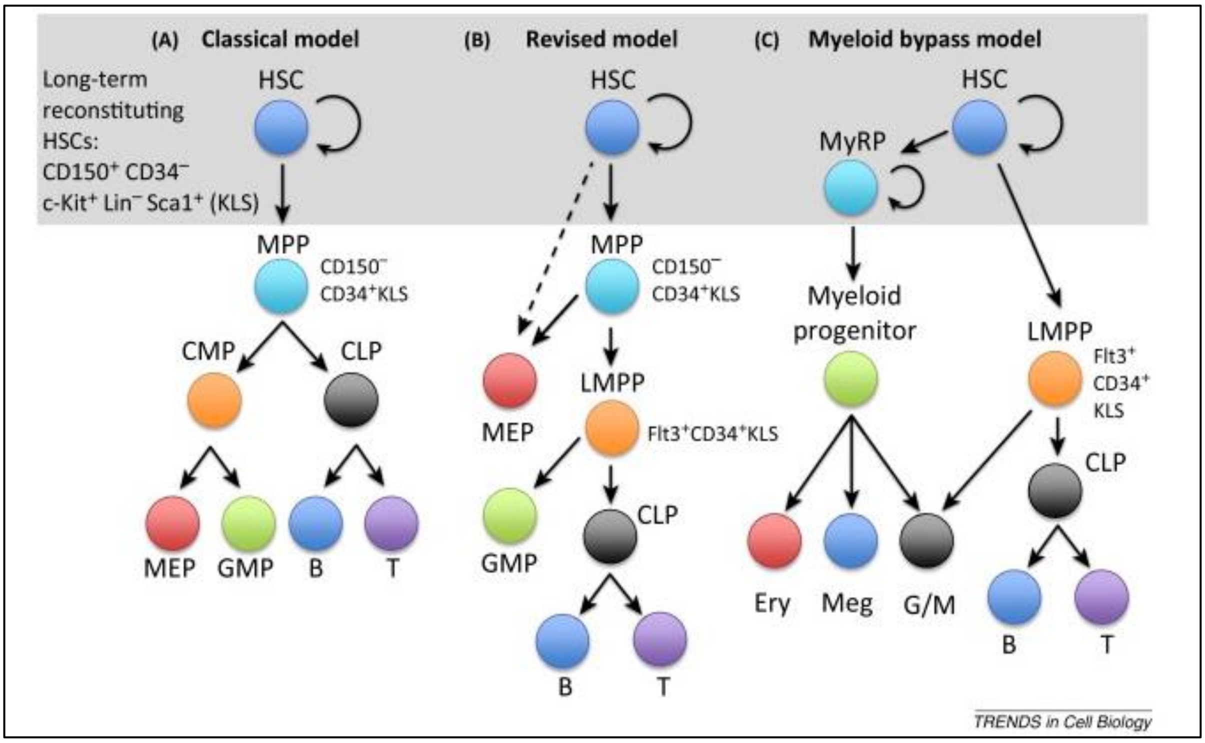

Fig. 1: Models of hematopoiesis. (A) The hierarchical model of lineage commitment during blood cell differentiation with long-term HSCs ($CD150^+$ $CD34^-$ c-kit^+ Lin^- $Sca1^+$) at top of the hierarchy that

differentiate to MPPs and further to CMPs or CLPs finally constituting MEPs, GMPs, B-cells and T-cells. (B) The revised hematopoiesis model was extended with the discovery of lympho/myeloid-restricted progenitors (LMPPs, Flt3$^+$ CD34$^+$ c-kit$^+$ Lin$^-$ Sca1$^+$) that have no potential to generate MEPs, postulating that megakaryocytic/erythroid lineage commitment is an early branching point during hematopoiesis. (C) The myeloid bypass model proposes that a megakaryocyte and myeloid-restricted progenitor (MyRP) is capable of self-renewal and myeloid lineage differentiation. HSC = hematopoietic stem cell; MPP = multipotent progenitor; CMP = common myeloid progenitor; CLP = common lymphoid progenitor; MEP = megakaryocyte erythroid progenitor; GMP = granulocyte macrophage progenitor; B = B lymphocyte; T = T lymphocyte; Ery = erythroid; Meg = megakaryocyte, G/M = granulocyte/monocyte (Image taken from [1]).

Stem cell maintenance is tightly regulated by a variety of cytokines, of which stem cell factor (SCF) and C-X-C motif chemokine ligand 12 (CXCL12) play an essential role [3-5]. SCF (also termed kit-ligand) binds to the receptor tyrosine kinase c-kit, which is expressed on HSCs [6]. Interaction of SCF with c-kit induces dimerization of c-kit monomers activating several downstream signaling pathways that regulate proliferation, survival, and adhesion [7]. CXCL12 binds to the C-X-C chemokine receptor 4 (CXCR4) and C-X-C chemokine receptor 7 (CXCR7, now referred to as ACKR3) respectively. CXCL12/CXCR4 signaling supports proliferation, homing after myeloablation and HSC retention in the BM [8, 9]. Consequently, disruption of the CXCL12 axis with CXCR4 antagonists, such as AMD3001, triggers the mobilization of HSCs from the BM to the peripheral blood. This mechanism is used to enrich HSCs prior to hematopoietic stem cell transplantation (HSCT) [10].

Besides hematopoietic cells that make up the majority of the cellular mass, the BM contains several other cell types and extracellular structures. The BM is embedded into a calcified bone matrix consisting of calcium hydroxyapatite and osteocalcium phosphate [11]. The endosteum at the medullary cavity of the bone is lined by osteoblasts and osteoclast, which regulate ossification as well as bone remodeling (Fig. 2) [11]. Blood vessels, including arterioles and sinusoids pervade the whole BM cavity and form together with the endosteum two anatomically defined HSC niches: the endosteal niche and perivascular HSC niche, with most HSCs residing adjacent to sinusoids [12].

The perivascular HSC niche is characterized by the high abundance of different cell types that synthesize factors, which promote HSC maintenance, such as SCF and CXCL12 (Fig. 2). These cells are of mesenchymal origin and can be found around blood vessel, thus they are termed “pericytes” [13]. Both arterioles and sinusoids, as well as the corresponding pericytes are associated with distinct vessel types and can be distinguished from each other on the basis of a specific set of surface markers. While BM arterioles can be identified by the expression of α-smooth muscle actin (α-SMA) derived from smooth muscle cells which ensheath arteriolar blood vessels, BM sinusoids express the glycoprotein endoglin (CD105) and the sialomucin endomucin on a high level [14, 15]. Arteriolar pericytes and sinusoidal pericytes can be discriminated by the expression of the proteoglycan neural-glial antigen 2 (NG2; arteriolar pericytes) and leptin receptor (LepR; sinusoidal pericytes) [16]. Studies with mice in which either NG2- or LepR- expressing pericytes were depleted show that the LepR^{+} sinusoidal niche is the predominant source of SCF and most important HSC niche [17]. A unique population of LepR^{+} sinusoidal pericytes in both, murine and human BM are CXCL12-abundant reticular (CAR) cells [3, 4, 18]. Characterized by their strong expression of CXCL12 and SCF, CAR cells are essential for the maintenance of HSC numbers and quiescence [3, 4].

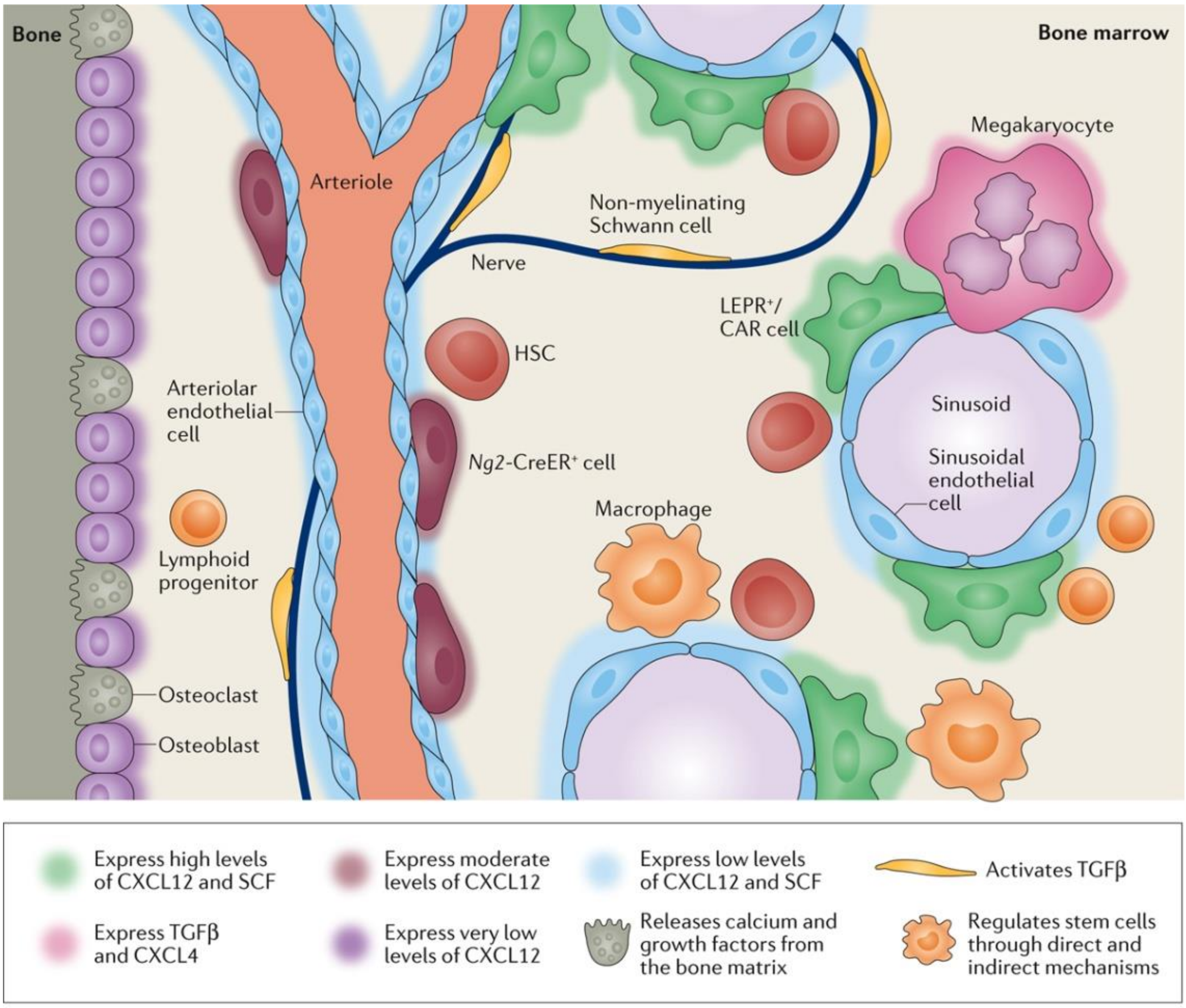

Nature Reviews | Immunology

Fig. 2. The BM HSC niche. Most BM HSCs reside in close proximity to LepR^{+} CXCL12 abundant (CAR) cells at sinusoidal blood vessels, which are a rich source of CXCL12 and SCF. NG2^{+} arterioles constitute an additional perivascular HSC niche, as studies using tamoxifen-inducible Cre-driven knockout of NG2 (Ng2-CreER^{+}) have demonstrated. Osteoblast are thought to play a role in the maintenance of lymphoid progenitor numbers. (Image taken from [12]).

Although the BM is the main site of hematopoiesis, the development and maturation of blood cells can under certain conditions occur outside of the BM, a phenomenon known as extramedullary hematopoiesis. One example for this is the hematopoietic cell maturation in mice: Mammalian primitive hematopoiesis begins in the yolk sac and transitions to the aorta-gonad mesonephros (AGM) region during fetal development. At day 13.5, the fetal liver is the main site of hematopoiesis before HSCs finally transfer from there to the BM shortly before birth [19]. In adult mammals, the spleen is a common site of extramedullary hematopoiesis e.g., during conditions of BM failure, and recently the lung has been discovered to be a hematopoietic organ besides the BM and the spleen [20, 21].

1.2. Megakaryopoiesis

Megakaryocytes (MKs) are the largest hematopoietic cells and the direct precursors of blood platelets. Mature MKs can be phenotypically defined by several characteristic features: (1) Next to their size with a diameter of up to 60 µm, (2) MKs have a polylobulated nucleus indicative of their polyploid chromosome set ranging from 4N to 128N. Polyploidy is achieved by endomitosis, which describes the process of several DNA replication steps without cytokinesis. (3) MKs contain a prominent invaginated membrane system referred to as demarcation membrane system (DMS) which serves as a membrane reservoir for the generation of up to 1000 platelets per MK. (4) The megakaryocytic lineage can be identified by the expression of various specific surface receptors, such as CD41 (integrin α_{IIb}) which is part of the fibrinogen receptor [22]. Although all MKs have these common features, it is challenging to specify one mature MK population based on polyploidy or size, as also smaller MKs with lower ploidy are still able to form proplatelets and platelets.

Our current concept of megakaryopoiesis is based on studies using classic histological staining techniques, BM transplantation and clonogenic assays to assess the hematopoietic potential of different precursor cells. Thus, the current model of megakaryopoiesis describes differentiation of HSCs into MEPs that give rise to megakaryoblasts, representing the first maturation stage of the megakaryocytic lineage. During further differentiation to (pro)-megakaryocytes (stage II), megakaryoblasts enrich granules and increase in size. Mature polyploid MKs finally represent the third stage of megakaryopoiesis [23, 24]. Immunophenotyping of surface markers is usually the method of choice to characterize differentiation of hematopoietic cells. Several MK-specific surface antigens become highly expressed on MKs during maturation. However, so far, no specific set of markers has been identified that could be attributed to a defined stage of megakaryopoiesis.

The most important cytokine driving megakaryopoiesis is thrombopoietin (TPO). Upon TPO binding to its receptor c-Mpl, receptor dimerization and an intracellular signaling cascade is induced, which involves among others Janus kinase (JAK) signaling, the MAPK pathway and phosphatidylinositol 3-kinases (PI3K) [25]. Loss of either TPO or c-Mpl lead to severe thrombocytopenia and exhaustion of the stem cell pool, further resulting in pancytopenia [26]. In humans the essential role of TPO for hematopoiesis and megakaryopoiesis is reflected by diseases of defective c-Mpl signaling, such as congenital amegakaryocytic thrombocytopenia (CAMT) or thrombocytopenia with absent radii (TAR) syndrome [27, 28].

TPO is constitutively synthesized in the liver. Regulation of TPO plasma concentration is mediated by TPO binding to c-Mpl and subsequent clearance from the plasma [29]. TPO levels are therefore inversely linked to the platelet count: thrombocytopenia leads to increased TPO levels, this can e.g., be observed in patients with CAMT. In addition to TPO, CXCL12 is a crucial regulator of megakaryopoiesis. A seminal study using TPO- and c-Mpl-deficient mice has demonstrated that TPO-independent megakaryopoiesis and thrombopoiesis is mediated by stroma cell-derived CXCL12 [30]. Furthermore, the authors describe CXCL12 to be involved in MK localization at the vascular niche, thereby regulating thrombopoiesis. These findings highlight the importance of niche factors for MK maturation and platelet biogenesis.

1.3. Platelet biogenesis and platelet function

Blood platelets are essential for hemostasis and are generated by the release of cytoplasmic MK fragments into the blood stream. For this, mature MKs that reside adjacent to BM sinusoids penetrate the endothelial lining with long protrusions, referred to as proplatelets. Once in the circulation, proplatelets then fragment due to shear forces to platelets [31].

The molecular mechanisms underlying *in vitro* PPF have been comprehensively studied [22, 32-34] contributing greatly to the understanding of platelet biogenesis. During the last years, major efforts were made to produce platelets *in vitro* [35-37]. However, so far it has not been possible to generate “lab-grown” platelets in a high amount and with sufficient hemostatic function. This implies that still unknown and crucial niche factors regulate thrombopoiesis *in vivo* that are not present during *in vitro* PPF.

In vivo PPF has to meet several requirements: (1) MKs have to be localized at sinusoids and polarize towards the vessel in order to avoid ectopic release of platelets into the cavity. (2) MK protrusions have to breach the vessel wall, which constitutes of sinusoidal endothelial cells (SECs), the extracellular matrix of the basement membrane and perivascular cells, such as CAR cells. (3) MKs are in permanent contact to matrix proteins, which are strong platelet activating agents. However, (pro)platelets must not be activated while being generated. Recently, advanced imaging techniques were used to describe the MK/vessel wall in more detail. Brown et al. postulate that MKs hold onto the sinusoidal lining with anchor points to release large cytoplasmic fragments into the blood stream [38]. Furthermore, it was demonstrated that podosome-like structures are involved in the diapedetic transit of MK protrusions through newly formed endothelial pores [39-41]. The underlying mechanisms regulating these processes remain elusive.

The primary function of platelets is to form a hemostatic plug upon vessel injury to prevent bleeding. Under steady-state conditions, platelet counts in humans are between 150 and $450x10^3/\mu l$ with a life span of approx. ten days. Platelets contain several organelles and granules of which α- and dense granules (also called δ-granules) play an essential role for platelet function. α-granules act as a reservoir for fibrinogen and other components that mediate coagulation and adhesion, such as P-selectin (CD62P), while δ-granules store compounds that support aggregate formation (e.g., ADP, serotonin, Ca^{2+}) [42, 43].

Upon vessel injury, platelets are initially immobilized by binding of the GPIb-V-IX von Willebrand factor (vWF) receptor complex to exposed vWF and collagen, which only become accessible at the damaged endothelial lining. This tethering leads to the deceleration and rolling of platelets along the vessel, allowing additional surface receptors to bind (Fig. 3). Next, the glycoprotein GPVI binds to exposed collagen, thereby inducing receptor dimerization and activation of an intracellular downstream signaling cascade. GPVI is non-covalently associated to an Fc receptor γ-(FcRγ) chain containing an immunoreceptor tyrosine-based activation motif (ITAM) that becomes phosphorylated by the Src family kinases (SFKs) Fyn and Lyn after GPVI activation. Further downstream signaling include phosphorylation of spleen tyrosine kinase (Syk), linker of activated T-cells (LAT) and phospholipase Cγ2 (PLCγ2) finally leading to release of intracellular Ca^{2+} and second wave mediators, such as thromboxane A_2. Second wave mediators as well as thrombin support platelet activation through the activation of G-protein coupled receptors. Firm adhesion and thrombus growth is facilitated by integrins, of which the fibrinogen receptor $\alpha_{IIb}\beta_3$ is most important [44]. This is emphasized by the severe bleeding risk of patients that suffer from lack or dysfunction of $\alpha_{IIb}\beta_3$, a disease termed Glanzmann thrombasthenia [45].

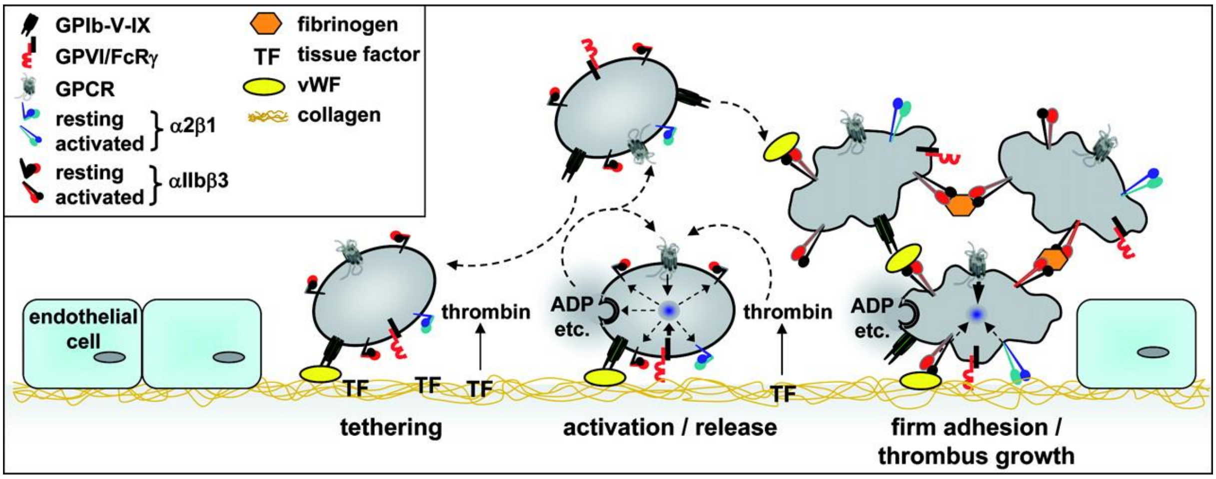

Fig. 3: Platelet activation and adhesion. Upon blood vessel damage platelets become activated by collagen binding via GPVI and integrin $\alpha_2\beta_1$. Tethering is mediated by binding of GPIb-V-IX to vWF. Platelets then release their granule contents to enable further activation, firm adhesion and thrombus growth. vWF = von Willebrand factor (Image was taken from [44]).

1.4. The bone marrow extracellular matrix

Hematopoietic and non-hematopoietic cells in the BM reside in a complex microenvironment composed of extracellular matrix (ECM) proteins that build a three-dimensional scaffold. ECM proteins provide mechanical stability, regulate cell adhesion and migration, and influence proliferation and differentiation. The main components of the BM ECM are proteoglycans, glycosaminoglycans, and fibrous proteins, such as laminins, fibronectin, and collagens [46].

Collagens are the most abundantly expressed proteins found in mammals. So far, 28 members of the collagen protein family have been identified in vertebrates. The primary structure of all collagens is based on left-handed polypeptide α-chains of repetitive glycine-proline-hydroxyproline sequences, also referred to as “GPO-motif”. Three intertwined α-helices assemble into hetero- or homotrimeric collagen fibrils that are crosslinked to collagen fibers. The fibrillar collagen type I is present throughout the BM and enriched in the bone cortex. Collagen type IV is a network-forming collagen and the most abundant protein in the basement membrane (basal lamina) of blood vessels. Although there are varying reports on the distribution of these collagen isoforms, studies using immunofluorescence staining to detect collagen type I and type IV in the murine BM have shown that they have in part overlapping localization in the marrow cavity and around blood vessels [14, 47].

MKs and platelets express several collagen receptors, of which the glycoprotein GPVI and integrin $\alpha_2\beta_1$ are the main ones. In addition, early MKs express other collagen receptors (DDR-1 and LAIR-1) which are downregulated in the course of maturation and not expressed on platelets [48, 49]. Adhesion of MKs and platelets to collagen is predominantly mediated by $\alpha_2\beta_1$, while collagen-triggered signaling is transduced by GPVI. The interaction of collagen type I with MKs has an inhibitory effect on *in vitro* PPF, in contrast to other collagen isoforms such as collagen type IV [14]. This implies a regulatory role of collagens in platelet production. However, mice lacking both GPVI and $\alpha_2\beta_1$ exhibit unaltered platelet counts, suggesting that PPF *in vivo* is not influenced by the ability to sense collagen [50].

Another ECM protein of the BM and crucial component of the basement membrane are laminins. Laminins are heterotrimeric proteins composed of one out of five α-, one out of five β- and one out of three γ-chains, forming a tissue-dependent set of distinct laminin isoforms based on their combination of subunits. So far, 18 out of 45 possible laminin isoforms have been detected. The main laminins in the BM are the α4- and α5-containing laminin-411/421 and laminin-511/521. While the α5-chain can be detected at arterioles as well as sinusoids, α4-chain expression is restricted to the arteriolar basement membrane. The essential role of laminins is highlighted by studies using murine laminin knockout models. A constitutive loss of single laminin subunits is generally embryonic lethal, with laminin α4 being an exception. Although Lama4 null mice exhibit impaired blood vessel formation due to abnormal basement membrane formation and hemorrhage during embryonic development, up to now they represent the only viable constitutive laminin knockout model [51]. The interaction of MKs and platelets with laminins is mediated by the integrin $\alpha_6\beta_1$ (VLA-6) [52]. Platelet-specific deletion of the α_6-subunit leads to protection from thrombosis without affecting normal hemostasis, which makes $\alpha_6\beta_1$ a possible antithrombotic target [53].

1.5. Extracellular matrix remodeling by matrix metalloproteinases

The ECM of the BM constantly undergoes reorganization, which is catalyzed by a family of zinc-dependent peptidases designated as matrix metalloproteinases (MMPs). The basic structure of all MMPs constitutes a catalytic domain and an autoinhibitory pro-domain, which has to be removed in order to expose the enzyme active site for substrate cleavage. Substrate recognition and protein-protein interaction is mediated by a hemopexin domain. The catalytic domains of the gelatinases MMP2 and MMP9 additionally have fibronectin type II repeats which facilitate binding to collagens [54]. Most MMPs are secreted into the extracellular space where activation occurs e.g., by proteolytic cleavage of the pro-domain or allosteric activation via distortion of the pro-domain away from the catalytic site. The latter mechanism is used to activate proMMP2 and proMMP9 *in vitro* with *p*-aminophenylmercuric acetate (APMA) [55].

The different members of the MMP family can be subdivided based on their protein structure and substrate specificity into collagenases, gelatinases, stromelysins, matrilysins, membrane-type MMPs and others [56]. Still, MMPs were shown to have redundant substrate specificity and exhibit overlapping enzymatic compensation, which was demonstrated in MMP double-mutant mouse models [57, 58]. Due to their role in cancer metastasis and inflammation potent small molecule MMP inhibitors, such as GM6001 (also known as Ilomastat), were introduced into clinical trials. However, lack of specificity and efficacy of these caused early termination of several trials further emphasizing the redundancy of MMP activity [59].

MMPs regulate several cellular processes through proteolysis of matrix proteins e.g., cell migration, proliferation, survival and chemoattraction by release of matrix-bound signaling molecules. One example for the biological role of MMPs is the vascular niche remodeling and angiogenesis mediated by MMP2 and MMP9. Studies using a murine model of choroidal neovascularization have demonstrated that corneal angiogenesis is attenuated in both single MMP2 and MMP9 knockouts, and strongly reduced in MMP2/MMP9-double deficient mice, suggesting synergetic function of MMP2 and MMP9 [60]. MMP9$^{-/-}$ animals display a defective endochronal ossification resulting in shortened femurs [61]. Moreover, MMP9 was shown to be involved in VEGF signaling by catalyzing the cleavage of VEGF, which then modulates vessel diameters [62]. Under homeostatic conditions MMP2 and MMP9 are expressed in the BM and play a role in hematopoiesis and reconstitution of the BM after myeloablation by proteolysis of ECM proteins and release of chemokines, such as kit ligand [63].

1.6. Total body irradiation and hematopoietic stem cell transplantation

During pathological conditions of the hematopoietic system e.g., leukemia, lymphomas, or non-malignant diseases such as BM failure syndromes, HSCT is often the only curative therapy option. HSCs used for transplantation can either be isolated from umbilical cord blood, enriched from the peripheral blood or from whole BM. In order to obtain a sufficient amount of peripheral blood stem cells (PBSCs) for transplantation, $CD34^+$ HSCs can be released from the BM by “steady-state” mobilization with G-CSF or mobilization with chemotherapeutic agents [64]. HSCs are then collected by leukapheresis with a target quantity of $2x10^6$ cells/kg body weight. Although PBSCs are used for the majority of HSCTs, whole BM is still an important stem cell source. BM is aspirated from the posterior superior iliac crest under general anesthesia with a goal of $3x10^8$ nucleated cells/kg. During the actual transplantation procedure, collected stem cells are irrespective of the stem cell source intravenously transfused into the recipient. The transplanted HSCs then home to the BM. This ideally leads to engraftment and reconstitution of the recipient’s hematopoietic system. The mechanisms by which HSCs find their way back to the BM are still not completely deciphered.

HSCT is typically preceded by myeloablative conditioning of the recipient BM to eradicate malignant cells, provide immunosuppression in order to prevent graft vs host disease (GvHD) and create space for the new graft. Myeloablation can be achieved by a combination of total body irradiation (TBI) with chemotherapy, typically with a dosage of 12Gy and subsequent cyclophosphamide treatment, or by chemotherapy alone (e.g., with busulfan and fludarabine). During the last 20 years, non-myeloablative/reduced intensity conditioning (NMA/RIC) has been introduced in order to minimize toxicity. However, NMA/RIC bears a higher risk of relapse in advanced disease [65]. The choice of a suitable conditioning type and intensity depends on multiple factors, such as the HSC donor age and type (autologous, allogeneic), the underlying disease, comorbidities, and toxicity risk. While TBI is used in only about 10% of patients after autologous HSCT, about 50% of patients with allogeneic HSCT receive TBI, with the main indications being BM malignancies, such as acute lymphoblastic leukemia (ALL), acute myeloid leukemia (AML), or chronic myeloid leukemia (CML) [66]. The essential role of TBI as a conditioning regimen, was recently demonstrated in a multinational, randomized clinical trial with pediatric ALL patients. The *For Omitting Radiation Under Majority age* (FORUM) study was conducted to determine whether TBI can be avoided prior to HSCT for childhood ALL. However, FORUM was discontinued ahead of schedule due to significantly reduced overall survival in the chemo-conditioning only cohort [67].

Myeloablation does not only result in the eradication of hematopoietic cells in the BM but leads also to depletion of peripheral blood cells (including platelets), leading to immunodeficiency and an elevated risk of life-threating infections. Another consequence of BM ablation is that although old, potentially malignant recipient cells are destroyed, at the same time the engraftment of donor cells is impaired by so-called "bystander" effects, which affect stromal cells at the vascular HSC niche [68]. A common complication associated with this is the delayed recovery of the megakaryocytic lineage and thrombocytopenia lasting for several weeks, which increases the risk of severe bleeding and the need for platelet transfusions. So far, the mechanisms leading to long-lasting thrombocytopenia after HSCT are not known. In addition to an increased risk of bleeding, other causes of morbidity and mortality in HSCT patients include thromboembolic complications, such as venous thromboembolism (VTE), thrombotic microangiopathy after transplantation (TMA), or sinusoidal obstruction syndrome (SOS). While endothelium-associated thrombotic events after transplantation have been investigated in previous studies [69], the role of platelets in these is completely unknown.

1.7. Aim of this study

Under homeostatic conditions thrombopoiesis is a process which is exclusively aimed in the direction of the vascular lumen. This directed process requires mechanisms by which MKs can perceive their position within the BM and at the vessel wall. Although several MK-intrinsic mechanisms and extracellular factors have been identified that modulate PPF, the triggers leading to platelet release *in vivo*, especially during aberrant thrombopoiesis are still enigmatic.

Thus, the aim of this study was to investigate the interaction of MKs with the vessel wall both under homeostatic and myeloablative conditions. First, we identified CAR cells as novel possible modulators of PPF using several high-resolution microscopy techniques. In a next set of experiments, we studied the MK/vessel wall interface in the irradiated BM with an emphasis on matrix remodeling by MMP9.

Poor or delayed engraftment of the megakaryocytic lineage after HSCT and thrombocytopenia-related hemorrhage are possibly life-threating complications. The increased demand for platelet transfusions that accompanies this, is a considerable financial burden and carries the risk of allo-immunization. Therefore, we aimed to investigate the impact of TBI-induced BM and vessel remodeling on MK engraftment in a murine HSCT model.

Paradoxically, HSCT is not only associated to bleeding but also to thromboembolic events. The contribution of platelets to post-HSCT thromboembolism has so far never been studied. Hence, we used a murine HSCT model to assess platelet function at early time points after transplantation.

2. Material and Methods

2.1. Material

2.1.1. Devices and Material

Table 1: Devices

Device	Manufacturer
7500 Fast Real Time PCR System	Applied Biosystems (Foster City, CA, USA)
Amersham Imager 600	GE Healthcare (Solingen, Germany)
APACT 4 aggregometer	LABitech (Ahrensburg, Germany)
Centrifuge 5415 C	Eppendorf (Hamburg, Germany)
Centrifuge 5424	Eppendorf (Hamburg, Germany)
Centrifuge 5424 R	Eppendorf (Hamburg, Germany)
Cryotom CM1900	Leica (Wetzlar, Germany)
FACS Celesta	BD Biosciences (Heidelberg, Germany)
Gene Touch Thermal Cycler	BIozym Scientific GmbH (Oldenburg, Germany)
Herolab	Herolab GmbH (Wiesloch, Germany)
Irradiation device CP-160 X-ray	Faxitron X-ray (Lincolnshire, USA)
Nanodrop 2000c	Thermo fisher (Waltham, MA, USA)
ScilVet abc Plus+	Scil animal care company GmbH (Viernheim, Germany)
Sysmex XP-300	Sysmex (Norderstedt, Germany)
TCS SP8 CLSM	Leica (Wetzlar, Germany)
Thermomixer comfort	Eppendorf (Hamburg, Germany)
Univet Isoflurane vaporizer	Groppler Medizintechnik (Deggendorf, Germany)
VWR MEGA STAR 1.6R	VWR part of avantor (Darmstadt, Germany)

Table 2: Material

Material	Manufacturer
18G, 26G canula	BD Biosciences (Heidelberg, Germany)
Adhesive cryofilm	Section lab (Hiroshima, Japan)

Cell strainer (70µm)	Pluriselect (Leipzig, Germany)
Coverslips 24x24mm	Carl Roth (Karlsruhe, Germany)
EDTA-K Microvettes	Sarsted (Nümbrecht, Germany)
FACS tubes	Corning (New York, USA)
Glass slides Superfrost plus	Thermo fisher scientific (Dreieich, Germany)
Heparinized capillaries	Hartenstein (Würzburg, Germany)
Low profile disposable blades DB80LX	Leica (Wetzlar, Germany)
Microcapillaries (50µl, 100µl)	Harteinstein (Würzburg, Germany)
Nitrocellulose membrane (0.45µm)	GE Healthcare (Solingen, Germany)
qPCR 96-well plates	Sarstedt (Nümbrecht, Germany)
qPCR sealing tape	Sarstedt (Nümbrecht, Germany)
Round coverslips Ø18mm #1	Carl Roth (Karlsruhe, Germany)
Round coverslips Ø24mm	Hartenstein (Würzburg, Germany)
Syringes (1ml)	Dispomed (Gelnhause, Germany)
Tissue Tek Cryomolds	Sakura Finetek Europe B.V. (Umkirch, Germany)

2.1.2. Chemicals and reagents

Table 3: Chemicals and reagents

Reagent	**Manufacturer**
Adenosine diphosphate (ADP)	Sigma-Aldrich (Schnelldorf, Germany)
Agarose	Roth (Karlsruhe, Germany)
Ammonium peroxidsulfate (APS)	Carl Roth (Karlsruhe, Germany)
Apyrase	Sigma Aldrich (Schnelldorf, Germany)
Bovine Serum Albumin (BSA)	Carl Roth (Karlsruhe, Germany)
Bradford solution	Bio-Rad Laboratories, Inc. (Hercules, CA, USA)
Claritiy Western ECL Substrate (ECL)	Bio-Rad Laboratories, Inc. (Hercules, CA, USA)
Chloroform	Carl Roth (Karlsruhe, Germany)
Collagen Related Peptide (CRP-X_L)	CRB Cambridge Research Biochemicals (Billingham, UK)

Convulxin	Prof. Elbe (Münster, Germany)
Coomassie Brilliant Blue R-250	Bio-Rad Laboratories, Inc. (Hercules, CA, USA)
CXCL12 mouse ELISA kit	Thermo Fisher Scientific (Waltham, USA)
dNTPs	Fermentas (St. Leon-Rot, Germany)
DQ-collagen type I	Thermo Fisher Scientific (Waltham, USA)
DQ-collagen type IV	Thermo Fisher Scientific (Waltham, USA)
DQ-gelatin	Thermo Fisher Scientific (Waltham, USA)
Dream Taq Polymerase	Fermentas (St. Leon-Rot, Germany)
Dream Taq Polymerase 10x buffer	Fermentas (St. Leon-Rot, Germany)
Dulbecos modified eagle medium (DMEM)	Thermo Fisher Scientific (Waltham, USA)
Fat-free dry milk	AppliChem (Darmstadt, Germany)
Fetal calf serum (FCS)	Sigma Aldrich (Schnelldorf, Germany
Fibrinogen	Sigma Aldrich (Schnelldorf, Germany)
Fluoroshield mounting medium	Sigma-Aldrich (Schnelldorf, Germany)
Fluoroshield mounting medium with DAPI	Sigma-Aldrich (Schnelldorf, Germany)
Gelatin solution, type B, 2%	Sigma-Aldrich (Schnelldorf, Germany)
GeneRuler 100bp DNA Ladder	Fermentas (St. Leon-Rot, Germany)
Glucose	Carl Roth (Karlsruhe, Germany)
GM6001	Santa Cruz (Dallas, Texas, USA)
Goat serum	Jackson Laboratory (Bar Harbor, Maine, USA)
Heparin	Ratiopharm (Ulm, Germany)
HORM Collagen	Takeda (Linz, Austria)
Human recombinant MMP2/MMP9	Biotez (Berlin, Germany)
Indomethacin	Alfa Aesar (Karlsruhe, Germany)
iScript cDNA Synthesis kit	Bio-Rad Laboratories, Inc. (Hercules, CA, USA)
Isoflurane CP	Cp-pharma (Burgdorf, Germany)
Isopropanol	Carl Roth (Karlsruhe, Germany)
iTaq Universal SYBR Green Supermix	Bio-Rad Laboratories, Inc. (Hercules, CA, USA)

Methanol	VWR Chemicals (Darmstadt, Germany)
Midori Green DNA stain	Nippon Genetics (Düren, Germany)
Murine Adiponectin ProcartaPlex Simplex kit	Thermo Fisher Scientific (Waltham, USA)
Murine TGF-β ProcartaPlex Simplex kit	Thermo Fisher Scientific (Waltham, USA)
PageRuler^{TM} Plus Prestained Protein Ladder	Thermo Fisher Scientific (Waltham, USA)
p-aminophenylmercuric acetate (APMA)	Sigma Aldrich (Schnelldorf, Germany)
Paraformaldehyde (PFA)	Sigma Aldrich (Schnelldorf, Germany)
Ponceau S Solution	Carl Roth (Karlsruhe, Germany)
ProcartaPlex murine custom 16 Plex kit	Thermo Fisher Scientific (Waltham, USA)
Prostacyclin (PGI_2)	Sigma Aldrich (Schnelldorf, Germany)
Protease inhibitor cocktail tablets	Roche (Basel, Schweiz)
Proteinase K	Fermentas (St. Leon-Rot, Germany)
RapiClear 1.52	SunJin Lab Co. (Hsinchu City, Taiwan)
RNEasy Mini Kit	QUIAGEN (Hilden, Germany)
Rotiphorese gel 30% acrylamide/bis-acrylamide	Roth (Karlsruhe, Germany)
SB-3CT	Santa Cruz (Dallas, Texas, USA)
SCF mouse ELISA kit	Thermo Fisher Scientific (Waltham, USA)
Sucrose	Carl Roth (Karlsruhe, Germany)
Super cryo embedding medium (SCEM)	Section Lab (Hiroshima, Japan)
Tetramethylethylendiamine (TEMED)	Carl Roth (Karlsruhe, Germany)
Thrombin	Roche (Basel, Schweiz)
TPO mouse ELISA kit	Thermo Fisher Scientific (Waltham, USA)
Triton X-100	AppliChem (Darmstadt, Germany)
Tween-20	Carl Roth (Karlsruhe, Germany)
TRIzol reagent	Thermo Fisher Scientific (Waltham, USA)

2.1.3. Antibodies

Table 4: Commercial Antibodies

Antibody	Manufacturer
anti-CD105 (MJ7/18)	eBioscience (San Diego, CA, USA)
anti-endomucin (V.7C7)	Santa Cruz (Dallas, Texas, USA)
anti-collagen type I (pAb)	Abcam (Cambridge, UK)
anti-collagen type IV (pAb)	Merck Millipore (Darmstadt, Germany)
anti-Ly6G (1A8)	BD Biosciences (Heidelberg, Germany)
anti-Ly6C Alexa 647 (HK1.4)	Biolegend (San Diego, Ca, USA)
anti-B220	Santa Cruz (Dallas, Texas, USA)
anti-Ter119	Santa Cruz (Dallas, Texas, USA)
anti-MMP9	Abcam (Cambridge, UK)
anti-GAPDH	Santa Cruz (Dallas, Texas, USA)
anti-cleaved collagen (pAb, Col1-¾C)	immunoGlobe GmbH (Himmelstadt, Germany)
anti-Syk	Cell Signaling Technologies (Danvers, MA, USA)
anti-pSyk525/526	Cell Signaling Technologies (Danvers, MA, USA)
anti-rat IgG Alexa 546 and 647	Life Technologies (Carlsbad, CA, USA)
anti-rabbit IgG A647	Life Technologies (Carlsbad, CA, USA)
anti-goat Alexa 647	Life Technologies (Carlsbad, CA, USA)
anti-rabbit IgG HRP	Dako (Hamburg, Germany)
anti-mouse IgG HRP	Dako (Hamburg, Germany)
anti-rat IgG HRP	Dako (Hamburg, Germany)

All listed antibodies are raised against mouse proteins.

Table 5: Non-commercial antibodies

Antibody	Manufacturer
anti-GPIb-FITC (15E2)	Nieswandt laboratory (Würzburg, Germany)
anti-GPIX-FITC and Alexa 488 (56F8)	Nieswandt laboratory (Würzburg, Germany)
anti-GPV-FITC (89H11)	Nieswandt laboratory (Würzburg, Germany)
anti-GPVI-FITC (JAQ1)	Nieswandt laboratory (Würzburg, Germany)
anti-integrin α_2-FITC (12C6)	Nieswandt laboratory (Würzburg, Germany)
anti-CD9-FITC (96H10)	Nieswandt laboratory (Würzburg, Germany)
anti-$\alpha_{IIb}\beta_3$-FITC (14A3)	Nieswandt laboratory (Würzburg, Germany)
anti-CLEC-2-FITC (INU1)	Nieswandt laboratory (Würzburg, Germany)

anti-CD62P-FITC (5C8)	Nieswandt laboratory (Würzburg, Germany)
anti-active $\alpha_{IIb}\beta_3$-PE (JON/A)	Nieswandt laboratory (Würzburg, Germany)
anti-laminin α5 (504)	Sorokin laboratory (Münster, Germany)

2.1.4. Buffers and solutions

All buffers used for this study were prepared using water from a MilliQ Purification system. For pH adjustment HCl or NaOH were used.

Dulbecco's Modified Eagle Medium + GlutaMAX (Gibco)

Phosphate buffered saline (PBS), pH 7.14

NaCl	137 mM
KCl	2.7 mM
KH_2PO_4	1.5 mM
Na_2HPO_4	8.0 mM

HEPES-Tyrode's buffer without Ca^{2+}

NaCl	137 mM
KCl	2.7 mM
$NaHCO_3$	12 mM
NaH_2PO_4	0.43 mM
$MgCl_2$	1 mM
HEPES	5 mM

(BSA fraction V solution 0.36% v/v) freshly added

(Glucose solution 0.1% v/v) freshly added

HEPES-Tyrode's buffer with Ca^{2+}

NaCl	137 mM
KCl	2.7 mM
$NaHCO_3$	12 mM
NaH_2PO_4	0.43 mM
$CaCl_2$	2 mM
$MgCl_2$	1 mM
HEPES	5 mM

(BSA fraction V solution 0.36% v/v) freshly added

(Glucose solution 0.1% v/v) freshly added

Protein lysis buffer, 2x, pH 7.4

HEPES	15 mM
NaCl	150 mM
EGTA	10 mM
Triton X-100	2% v/v
Protease inhibitor cocktail	1x freshly added

Separation gel buffer, pH 8.8

Tris-HCl	1.5 M

Stacking gel buffer, pH 6.8

Tris-HCl	1 M

SDS sample buffer, 4x reducing

Tris-HCl	200 mM
Glycerol	40% v/v
SDS	8% w/v
Bromphenol blue	0.04% w/v
β-Mercaptoethanol	2% v/v

Blocking buffer

TBS-T

BSA or fat-free dry milk 5% w/v

SDS sample buffer, 2x non-reducing

Tris-HCl	80 mM
Glycerol	10% v/v
SDS	2% w/v
Bromphenol blue	0.02% w/v

Laemmli buffer

Tris	40 mM
Glycine	0.95 mM
SDS	0.5% w/v

Transfer buffer

$NaHCO_3$	10 mM
Na_2CO_3	3 mM

(Methanol 20% v/v) freshly added

Tris buffered saline (TBS), pH 7.3 (10x)

NaCl	137 mM
Tris-HCl	20 mM

Washing buffer (TBS-T)

TBS (1x)	
Tween-20	0.1% v/v

Gelatin-zymography washing buffer I, pH 7.5

Tris-HCl	50 mM
$CaCl_2$	10 mM
Triton X-100	2.5% v/v
NaN_3	0.02% w/v
$ZnCl_2$	50 µM

Gelatin-zymography washing buffer II, pH 7.5

Tris-HCl	50 mM
NaCl	150 mM
$CaCl_2$	10 mM
NaN_3	0.02% w/v
$ZnCl_2$	50 µM

In situ zymography reaction buffer

Tris-HCl	50 mM
NaCl	150 mM
$CaCl_2$	5 mM
$ZnCl_2$	1 mM

Coomassie destaining solution

MetOH	10% v/v
Acetic acid	10% v/v

Gitschier buffer (10x)

Tris	670 mM, pH 8.8
$(NH_4)_2SO_4$	166 mM
$MgCl_2$	65 mM
Triton X-100	0.5% v/v

DNA lysis buffer

Gitschier (10x)	10%
Proteinase K	1 mg/ml
β-Mercaptoethanol	1% v/v

TAE buffer, 50x, pH 8.0

TRIS	200 mM
Acetic acid	5.7% v/v
EDTA	50 mM

Orange G, loading dye 6x

Tris-HCl	10 mM, pH 7.6
Glycerol	60% v/v
EDTA	60 mM
Orange G	0.15% w/v

Washing buffer (immunofluorescence)

PBS	
FCS	5% v/v
Tween-20	0.1% v/v

Blocking buffer (immunofluorescence)

Washing buffer	-
Serum	10% v/v

Blocking solution (3D staining)

PBS	
BSA	1% v/v
Serum	10% v/v
Triton X-100	0.2% v/v

2.1.5. Mouse models

Table 6: Mouse models

Mouse line	Background	Source
CXCL12-dsRed	C75BL/6J	Jackson Laboratory [17]
L2G85.90-2 DsRed (Actb^{dsRed})	C75BL/6J	Andreas Beilhack, Würzburg, Germany [70]
MMP9$^{-/-}$	FVB -> C75BL/6J (mixed)	Charles River FVB/N-Tg(Eno2-MMP9)1Pfi [61]
Lama5.Cdh5-Cre	C75BL/6J	Jeffrey Miner, St. Louis, MO, USA; Erik Henke, Würzburg, Germany

2.1.6. Primers

All primers were ordered from Metabion (Planegg, Germany). The following primer pairs were used for genotyping or qPCR analysis.

Table 7: Primers

Primer	Sequence 5’ -> 3’
MMP9_WT_for	GTGGGACCATCATAACATCACA
MMP9_rev1_WT	CACCAAACTGGATGACAATGTC
Jax_Common_fw	TCCTCCATCCACAGGCATAC
Jax_Mutant_rev	CCTTCTATCGCCTTCTTGACG
CXLC12-dsRed_Common_rev	CAG AGC TGC GAG CCT TTC
CXCL12-dsRed_WT_fw	CTG GTT TTC GCC TCT AAA GC
CXCL12-dsRed_Mutant_fw	TCG GCA AAA TCC CTT ATA AAT C
Lama5_F17	GTGCCGCCCTAACACCCAAGG

Lama5_R17	GTTGCCAAAGCGTACAGCG
Cre_fw	GCCTGCATTACCGGTCGATGCAACGA
Cre_rev	GTGGCAGATGGCGCGGCAACACCATT
MMP2_RT_fw (qPCR)	GACATTGTCTTTGATGGCATCG
MMP2_RT_rev (qPCR)	CAGTGTCCGCCAAATAAACCG
MMP9_RT_fw (qPCR)	GCGTGGATAAGGAGTTCTCTG
MMP9_RT_rev (qPCR)	GCAGAAATAGGCTTTGTCTTGG
RT_MMP8_fw (qPCR)	TTGAGAAAGCTTTTCACGTCTG
RT_MMP8_rev (qPCR)	CTTGAGACGAAAGCAATGTTGA
RT_MMP13_fw (qPCR)	CTTCCTGATGATGACGTTCAAG
RT_MMP13_rev (qPCR)	GTCACACTTCTCTGGTGTTTTG
RT_MMP14_fw (qPCR)	TATGGTTTACAAGTGACAGGCA
RT_MMP14_rev (qPCR)	AAACTTATCCGGAACACCACAG
RT_MMP19_fw (qPCR)	CTTCTTCAAGCTGCATCCAG
RT_MMP19_rev (qPCR)	CTTCCTCCTCATCTCTTGTCTC
GAPDH_mus_RT_fw (qPCR)	GGGTTCCTATAAATACGGACTGC
GAPDH_mus_RT_rev (qPCR)	CCAATACGGCCAAATCCGTTC

2.2. Methods

2.2.1 Mouse Studies

Animal husbandry and Generation of transgenic mice

Animal husbandry was performed according to institutional guidelines and approved by the local authorities (Regierung von Unterfranken, AZ 55.2-2532-2-387).

Constitutive MMP9-deficient mice were obtained from Charles River and originally characterized in [61]. CXCL12-dsRed reporter mice were described in [17] and donated to the Jackson Laboratory from which this mouse line was imported into the animal facility of the institute. Actb^{dsRed} mice were kindly provided by Prof. Dr. Andreas Beilhack. Conditional laminin α5 knockout mice were generated by cross breeding of Lama5$^{fl/fl}$ mice (from Dr. Jeffrey Miner) with Cdh5-Cre mice (from Dr. Erik Henke).

Genotyping of transgenic mice

<u>Isolation of genomic DNA from ear biopsies</u>

Ear punches were lysed in 100 µl DNA lysis buffer for at least 2 h at 56°C and 1400 rpm. Afterwards samples were boiled for 5 min at 95°C, centrifuged at 16.215 g for 10 min and stored at -20°C.

Genotyping of MMP9 mice

Primers used for genotyping of MMP9 mice are listed in Table 7. The expected band sizes are 350 bp for wildtype and 370 bp for knockout. For genotyping 2 µl DNA was used.

Table 8. PCR mix for MMP9 genotyping

Reagent	Volume [µl]
H2O	18.55
10x PCR Buffer	2.5
$MgCl_2$	0.5
dNTPs	1
Primer forward	0.1
Primer reverse	0.1
DreamTaq Polymerase	0.25

Table 9. PCR cycler program for MMP9$^{+/+}$ mice

Step	Temperature [°C]	Duration [min]
1	95	5
2	95	1
3	56.8	1
4	72	2
5	72	10
6	4	∞

Repeat steps 2 – 4 for 35 cycles

Table 10. PCR cycler program for MMP9$^{-/-}$ mice

Step	Temperature [°C]	Duration [min]
1	95	5
2	95	1
3	52.1	1
4	72	2
5	72	10
6	4	∞

Repeat steps 2 – 4 for 35 cycles

Genotyping of CXCL12-dsRed mice

Primers used for genotyping of CXCL12-dsRed mice are listed in Table 7. The expected band sizes are 229 bp for wildtype and 184 bp for transgenic mice. For genotyping 1 µl DNA was used.

Table 11. PCR mix for CXCL12-dsRed genotyping

Reagent	Volume [µl]
H_2O	13.8
10x PCR Buffer	5
$MgCl_2$	2
dNTPs	1
Primer forward	1
Primer reverse	1
Taq Polymerase	0.2

Table 12. PCR cycler program for CXCL12-dsRed mice

Step	Temperature [°C]	Duration [min]
1	95	5
2	95	0.5
3	52.1	0.5
4	72	1
5	72	10
6	4	∞

Repeat steps 2 – 4 for 35 cycles

Genotyping of Lama5.Cdh5-Cre mice

Primers used for genotyping of Lama5.Cdh5-Cre mice are listed in Table 7. The expected band sizes are 296 bp for the wildtype and 460 bp for the floxed allele. For genotyping 1 µl DNA was used.

Table 13. PCR mix for Lama5.Cdh5-Cre mice

Reagent	Volume [µl]
H_2O	15.75
10x PCR Buffer	2.5
$MgCl_2$	2.5
dNTPs	1
Primer forward	1
Primer reverse	1
Taq Polymerase	0.25

Table 14. PCR cycler program for Lama5.Cdh5-Cre mice

Step	Temperature [°C]	Duration [min]
1	95	5
2	95	1
3	62	1
4	72	1
5	72	10
6	4	∞

Repeat steps 2 – 4 for 35 cycles

Table 15. PCR mix for Cdh5-Cre

Reagent	Volume [µl]
H_2O	17.8
10x PCR Buffer	2.5
$MgCl_2$	2.5
dNTPs	1
Primer forward	0.1
Primer reverse	0.1
Taq Polymerase	0.5

Table 16. PCR cycler program for Cdh5-Cre

Step	Temperature [°C]	Duration [min]
1	96	3
2	94	0.5
3	62	0.5
4	72	0.75
5	72	10
6	4	∞

Repeat steps 2 – 4 for 35 cycles

Agarose gel electrophoresis

For visualization of PCR products samples were loaded on a 1.5% (w/v) agarose gels. Agarose was dissolved in TAE buffer by boiling. Afterwards 5 µl Midori green per 100 ml was added and samples were mixed 1:6 with orange G loading dye. DNA separation was achieved by application of a constant voltage of 100 – 120 V for 20 – 45 min. PCR products were visualized by UV light in a Herolab transilluminator.

Irradiation of mice and transplantation of whole bone marrow

For irradiation studies mice received a sublethal (5Gy) total body irradiation using a CP-160 X-ray irradiation system (Faxitron X-Ray, Lincolnshire, IL, USA). HSCT studies were performed by transplantation of whole BM into C57BL/6J mice. For this BM was harvested from Actb^{dsRed} femora and tibiae by centrifugation as described in [71]. Recipient mice were conditioned by lethal (10 Gy) TBI and were retro-orbitally injected using a 26 G needle with 1 to 6x10^{6} BM cells. To prevent infections following irradiation and transplantation mice were treated with neomycin (2 g/l) drinking water. General health conditions (weight, fur structure and behavior) were monitored daily after radiation treatment.

2.2.2. *In vitro* analyses

Isolation of platelets for aggregometry

Mice were anesthetized by isoflurane inhalation and fully bled using a heparinized glass capillary into reaction tubes containing 300 µl heparin (20 U/ml). Platelet rich plasma (PRP) was obtained by centrifugation of anticoagulated whole blood at 300 g for 6 min without brakes. The upper phase was then transferred to a new reaction tube containing 200 µl heparin and centrifuged again at 300 g for 6 min. The upper phase was again transferred to a new reaction tube and afterwards centrifuged at 736 g for 5 min. After discarding of the supernatant 1 ml HEPES-Tyrode's (HT) buffer without Ca^{2+} containing BSA, glucose, apyrase (f.c. 0.02 U/ml) and PGI$_2$ (f.c. 0.1 µg/µl) were used to wash the platelet pellet twice. Platelet counts were then adjusted to $500x10^3$/µl with a Sysmex KX21N automated hematology analyzer and let rest for 30 min at 37°C. For platelet activation thrombin (f.c. 0.001 U/ml), Horm collagen (f.c. 4 µg/µl) and CRP-X_L (f.c. 0.1 µg/µl) were used. All agonists were diluted with HT-buffer with Ca^{2+} to which fibrinogen (f.c. 70 µg/µl) was added, except for thrombin. The APACT 4 aggregometer was blanked using 110 µl of HT-buffer with Ca^{2+} (± fibrinogen). For measurement of platelet aggregation, 50 µl platelet suspension were mixed with 110 µl of HT-buffer with Ca^{2+} in an aggregometry cuvette. 30 sec after start of the measurement 1.6 µl diluted agonist was added and the changes in light transmission were recorded by the APACT LPC software over a period of 10 min.

Analysis of platelets by flow cytometry

Determination of platelet surface receptor expression and function was done using flow cytometry. For this, 50 µl of blood was collected by retro-orbital bleeding under isoflurane anesthesia and diluted with 700 µl of HT-buffer without Ca^{2+}. In order to detect glycoproteins and integrins, 10 µl of fluorescein-5-isothiocyanate (FITC)-coupled antibodies listed in Table 5 were added to 50 µl of the diluted blood. The samples were then incubated in the dark for 15 min, after which the staining was stopped with 500 µl PBS. For platelet activation blood was centrifuged at 736 g for 5 min, the supernatant was discarded, and the pellet was resuspended in 1 ml of HT-buffer without Ca^{2+}. After centrifugation at 736 g for 5 min, the supernatant was removed again, and the pellet was finally resuspended in HT-buffer with Ca^{2+}. Platelets were stimulated with thrombin (f.c. 0.1, 0.01, and 0.001 U/ml), CRP-X_L (f.c. 10, 1, and 0.1 µg/ml), and convulxin (f.c. 1 µg/ml) for 6 min at 37°C and additional 6 min at room temperature (RT). Degranulation was measured by a FITC-coupled antibody against P-selectin (CD62P, Table 5). Active integrin $\alpha_{IIb}\beta_3$ was detected by addition of JON/A-PE antibody. Samples were stopped with 500 µl PBS and measured with a FACS Celesta (BD Biosciences).Data was acquired using Diva software (BD Biosciences) and analyzed with FlowJo (BD Biosciences).

RNA isolation and cDNA synthesis

For isolation of RNA from whole BM samples mice were sacrificed and BM was isolated as described in [71]. BM cells were then resuspended in 1 ml TRIzol and frozen at -80°C until use. Frozen tissue samples were thawed and 200 µl chloroform were added. After centrifugation at 12.000 g at 4°C for 15 min the upper phase was transferred to a new reaction tube and mixed with 70% EtOH at an equal volume. Further extraction steps were carried out using the RNEasy RNA extraction kit (QIAGEN) according to the manufacturer’s instructions. Concentration of isolated RNA was measured with a Nanodrop 2000c. For cDNA synthesis the iScript cDNA Synthesis kit (Bio-Rad Laboratories) with 500 ng RNA was used according to the manufacturer’s recommendations.

Analysis of MMP mRNA expression by qPCR

To assess MMP mRNA expression quantitative real time PCR (qPCR) was performed. Data was evaluated using the ΔΔCt method in which Ct values of the analyzed MMPs were normalized to Ct values of the house keeping gene *Gapdh*. The primers used for qPCR analysis are listed in Table 7.

Table 17. qPCR mix

Reagent	Volume [µl]
H_2O	6.8
SYBR Green Master Mix	10
Primer forward	0.6
Primer reverse	0.6
cDNA	2

Table 18. qPCR cycler program

Step	Temperature [°C]	Duration [min]
1	50	2
2	95	10
3	95	0.25
4	60	1
5	95	0.25
6	60	1
7	95	0.5
8	60	0.25

Repeat steps 3 – 4 for 40 cycles. Steps 5 – 8: melt curve

2.2.3. Biochemical analyses

Protein lysate preparation

Whole BM lysates for immunoblot analysis were prepared by isolation of BM as described in [71] and incubation in protein lysis buffer containing protease inhibitors for 30 min on ice. Lysed samples were centrifuged at 16.215 g for 10 min at 4°C and the supernatant was transferred into a new reaction tube. Protein lysates were stored at -20°C until use. For analysis of phoshoproteins in platelet lysates PRP was prepared as described above. Platelet counts in all samples were adjusted to $500x10^3$/µl. Samples were then incubated with indomethacin (f.c. 10 µM), EDTA (f.c. 5 mM) and apyrase (f.c. 2 U/ml) for 5 min at 37°C. Next, at least 260 µl of the platelet suspension was transferred into an aggregometry cuvette. For unstimulated samples 50 µl of the platelet suspension was taken and lysed in an equal amount of 2x protein lysis buffer. For stimulated samples, CRP-X_L (f.c. 30 µg/ml) was added to the sample with stirring. 60 sec after activation 50 µl platelet suspension was taken and mixed with an equal amount of lysis buffer. All samples were then incubated for 10 min on ice and centrifuged at 16.215 g for 10 min at 4°C. Protein lysates were aliquoted (25 µl each) and stored at -80°C until use.

Measurement of protein concentration according to Bradford

The protein content of lysates was determined by Bradford protein assay. In order to measure a standard curve 25 µl of BSA samples ranging 100 µg/ml to 1000 µg/ml were mixed with 1:6 diluted Bradford solution in micro cuvettes. Subsequently 5µl of protein lysates were added to 995 µl diluted Bradford dye. Samples and standards were incubated for 5 min in the dark and the protein content was then measured by photometrical determination of the absorbance at 595 nm with a Nanodrop 2000c.

Immunoblotting by classical Western blotting and Simple Jess

The protein expression levels of MMP9 and cleaved collagen were analyzed by classical Western Blotting. Separation of proteins based on their molecular weight was done by SDS-polyacrylamide electrophoresis. For this 20 µg of protein lysates were mixed with 4x reducing sample buffer and boiled at 95°C for 5 min. Cooled samples were then loaded onto a 10% SDS gel and a constant voltage of 120 V was applied for approx. 1.5 hours. Separated proteins were then wet transferred onto a 0.45 µm nitrocellulose membrane at 350 mA for 60 min. Free antibody binding sites were afterwards blocked with 5% milk in TBS-T for 1 h and membranes were probed with primary antibodies overnight at 4°C. Membranes were washed 3 times for 5 min with TBS-T and incubated with respective HRP-coupled secondary antibodies for 1 h at RT. After washing for 3 times for 5 min with TBS-T membranes were coated with an enhanced chemiluminescence (ECL) substrate and detected in a digital Western blot imager (Amersham Imager 680, GE Healthcare). For the immunoblots shown in Fig. 9, Coomassie staining was used to visualize protein bands as loading controls. After electrophoresis SDS gels were stained in Coomassie Brilliant Blue R-250 for 30 min and destained in Coomassie destaining solution until protein bands were adequately visible.

Phosphorylation levels of Syk were determined using the automated capillary-based immunoassay system Jess (ProteinSimple) in cooperation with Dr. Zoltan Nagy as described in [72].

Assessment of MMP2 and MMP9 activity by gelatin-zymography

The gelatinolytic activity of MMP2 and MMP9 in whole BM lysates was determined by gelatin-zymography. Zymography lysates were prepared as described in section “Protein lysate preparation”, except that no protease inhibitors were added to the lysis buffer. Gelatinase activity was compared to recombinant MMP2 and MMP9 standards, which were activated prior to zymography by incubation with APMA (f.c. 2 mM) for 1 h at 37°C. MMP standards and 20 µg of zymography protein lysates were mixed with 2x non-reducing sample buffer and incubated for 30 min at 37°C. Standards and samples were then loaded onto a 7.5% SDS zymography gel that was supplemented with 0.1% gelatin. After electrophoresis at first 100 V for 10 min and then 200 V for 30 min zymography gels were washed in zymography washing buffer I for 2 h at 4°C. To facilitate gelatinase activity zymography gels were then incubated in zymography washing buffer II overnight at 37°C under agitation. To visualize gelatinolytic activity zymography gels were stained with Coomassie Brilliant Blue R-250 for 30 min and destained in Coomassie destaining solution until negative bands became visible. Gelatin-zymography results were documented in a Herolab transilluminator.

Determination of chemokine levels using ProcartaPlex Multiplex Immunoassay

Serum chemokine levels were measured by ProcartaPlex immunoassay according to the manufacturer’s instructions. A custom designed chemokine panel was chosen using the ThermoFisher Scientific ProcartaPlexTM panel. Mice were fully bled from the retro-orbital plexus and blood was allowed to clot for 20 min at RT. Samples were then centrifuged at 1000 g for 10 min and supernatant transferred to new reaction tubes. Serum was then stored at -80°C until use. Samples that were used for adiponectin detection were diluted 1:2000. Serum used for measurement of TGF-β were activated by addition of 1N HCl and subsequent neutralization with 1.2N NaOH. The immunoassay was performed using a Luminex200 instrument and the Luminex xPONENT software.

Measurement of TPO, CXLC12 and SCF by ELISA

TPO, CXCL12 and SCF expression levels were determined in blood serum using Invitrogen mouse ELISA kits. Samples were generated as described in the previous section and TPO, CXLC12 and SCF levels were analyzed according to the manufacturer’s instructions. Plates were analyzed with a Tecan Infinite 200Pro plate reader at 450 nm.

2.2.4. *In situ* analyses

Organ preparation

Mice were anesthetized with isoflurane and sacrificed by cervical dislocation. After the abdominal wall was opened femora, tibiae, sternae and spleens were isolated and transferred to a reaction tube containing 1 ml 4% paraformaldehyde (PFA). Organs were fixed for 4h at 4°C and then dehydrated in 10, 20 and 30% sucrose (w/v) each for 24 h at 4°C. Prior to cryosectioning organs were embedded in SCEM cryomatrix and frozen at -80 °C overnight. Frozen samples were either sliced into 7 µm thin sections onto Kawamoto's adhesive film or used for thick sectioning (> 200 µm). For this cryoblocks were trimmed from both sides until organs became sufficiently visible.

Immunofluorescence staining and optical clearing

For immunofluorescence staining of thin sections samples were thawed and rehydrated with PBS. Unspecific binding sites were blocked for 20 min in blocking buffer and sections were then probed with primary antibodies for 45 min at RT and afterwards washed 3 times for 5 min with washing buffer. Sections were next incubated with respective secondary antibodies for 45 min at RT. After washing 3 times for 5 min incubation and wash steps were repeated for each antigen of interest. After staining sections were dried at 4°C and mounted with DAPI-containing Fluoroshield. Staining for 3D BM reconstruction was done by incubation of samples in blocking solution (for 3D staining) overnight and subsequently in primary antibody for three days at 4°C. After washing in PBS overnight at 4°C organs were transferred to buffer containing the respective secondary antibody and were incubated for three days at 4°C. The PBS wash and antibody incubation steps were repeated for all proteins of interest and organs were then optically cleared using RapiClear 1.52.

In situ Zymography

For analysis of MMP activity by *in situ* zymography femora were extracted as described in section "Organ preparation" and directly embedded and frozen in SCEM medium at -80°C without prior fixation. Unfixed femur sections were prepared using Kawamoto's adhesive film and post-fixated with 100% EtOH for 5 min at RT. For MMP inhibitor studies sections were permeabilized for 20 min with washing buffer and incubated with GM6001 (f.c. 1mM), SB-3CT (f.c. 1 mM) or PMSF (f.c. 1 mM) for 1 h covered with parafilm. DQ-substrates (DQ-gelatin, DQ-collagen type I or DQ-collagen type IV) were diluted to a final concentration of 20 µg in *in situ* zymography reaction buffer. Sections were covered with 250 µl diluted DQ-substrate and incubated for 2 h at 37°C in a humid chamber to facilitate gelatinase activity. Next, sections were washed with Millipore water and fixed with 4% PFA for 10 min at RT. After washing 3 times with PBS for 5 min nuclei were counterstained with DAPI for 3 min. Sections were again washed 3 times for 5 min with PBS and dried overnight at 4°C. *In situ* zymography samples were mounted using Fluoroshield without DAPI.

2.2.5. Imaging

Serial-blockface scanning electron microscopy (SBF-SEM)

Ultrastructural analysis of the MK/vessel wall interface was done by SBF-SEM in cooperation with PD Dr. Nicole Wagner and Prof. Dr. Süleyman Ergün (Institute of Anatomy and Cell Biology, University of Würzburg) according to the protocol in [73].

Confocal laser scanning microscopy (CLSM) and image analysis

Fluorescence images were acquired using a confocal laser scanning microscope (TCS SP8, Leica Microsystems CMS) with a 10x/NA 0.3 air objective and 40x/NA 1.3 oil objective. LAS X software was used for image documentation, analysis, and 3D reconstruction of BM volumes. Processing of thin section images, evaluation of MK number and size, and intersinusoidal distance was performed with Image J (Version 2.0.0-rc-43/1.51g, NIH, MD, USA) software. The number of proplatelet-forming MKs in contact to CAR cells was determined with seven whole femur scans. The total MK number (3679) and the number of proplatelet-forming MKs (54) was counted and "no contact" or "contact" was defined by the presence of CAR cell staining at the site of protrusions, as shown in the representative images in Fig. 4.

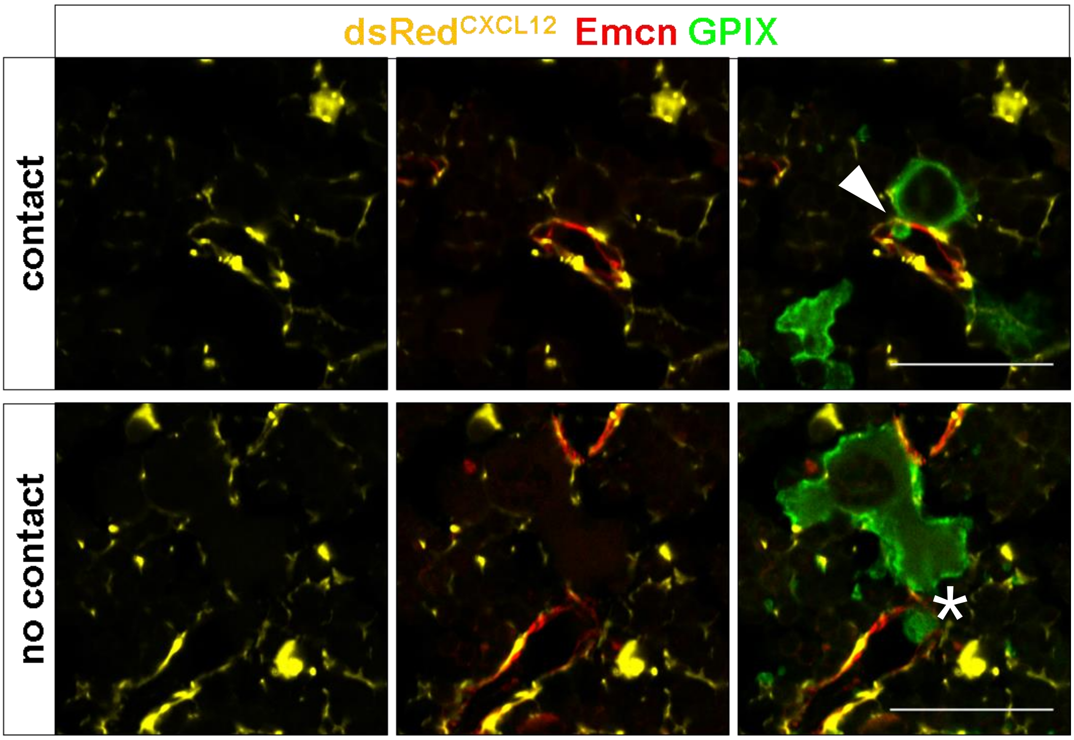

Fig. 4. Representative images of MKs in contact vs. no contact to CAR cells. The white arrowhead marks a contact site between a protruding MK and a CAR cell; no contact area is marked with a white asterisk. Scale bar 40 µm.

The intersinusoidal distance was determined by measuring of the distance of neighboring vessel to each other as shown in Fig. 5.

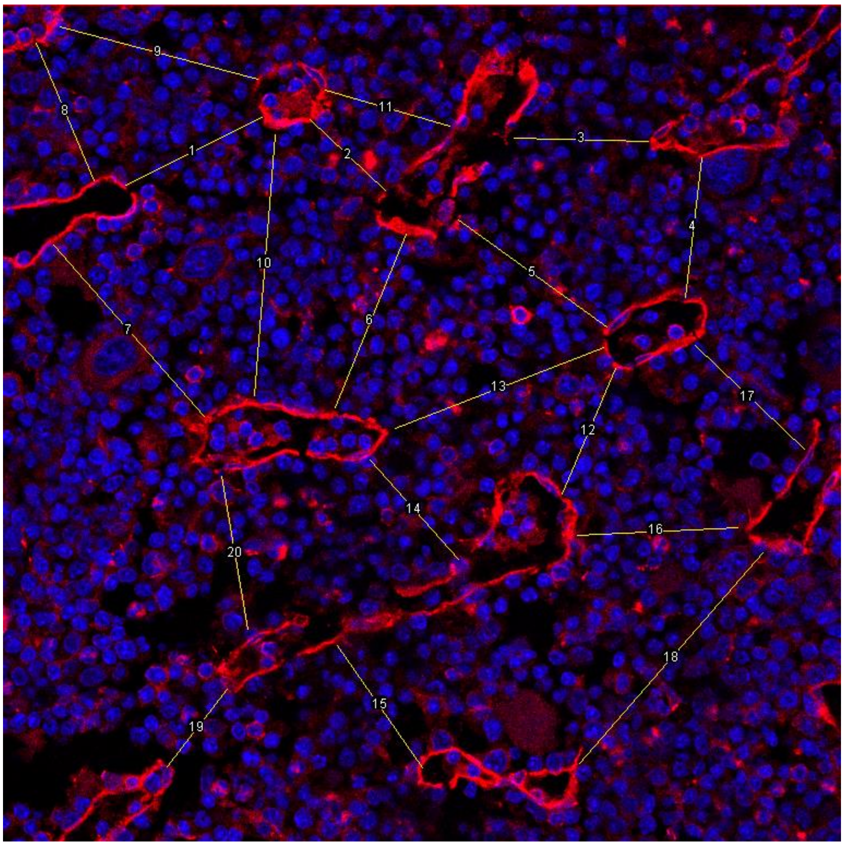

Fig. 5. Measurement of the intersinusoidal distance on femur sections. Sinusoids are indicated in red.

2.2.6. Statistical data analyses

Results are presented as mean ± standard deviation (SD) from at least three independent experiments, unless indicated otherwise. All data was tested by Shapiro Wilk test for their distribution curve using GraphPad Prism 9 software (GraphPad Software Inc, San Diego, CA, USA). Significant differences of lognormal data were analyzed by Kruskal-Wallis test with Dunn’s multiple comparison. Normally distributed data sets were evaluated with ANOVA. *P*-values < 0.05 were considered as statistically significant (* $P < 0.05$; ** $P < 0.01$; *** $P < 0.001$).

3. Results

3.1. Megakaryocyte-sinus wall interaction

While proplatelet formation has been studied extensively *in vitro* since recombinant TPO became available in 1994 [74, 75] the transition of MKs into proplatelets and finally platelets *in vivo* is far less well characterized, in part due to poor accessibility of the hematopoietic compartment which is located within the calcified bone cortex. The development of advanced sectioning and staining techniques for calcified tissue [14, 76] as well as intravital multicolor microscopic approaches of the BM [31] have led to the generally accepted model of thrombopoiesis, where mature MKs start to polarize at BM sinusoids and then penetrate the endothelial barrier with cytoplasmic protrusions to release proplatelets and platelets into the blood stream. However, most studies focus on the interaction of MKs with SECs and overlook additional components of the sinus wall, including the vascular basement membrane ECM as well as reticular cells (RC), including CAR cells. We thus raised the question whether perivascular CAR cells influence MKs and the transmural passage of proplatelet protrusions.

3.1.1. CXCL12-abundant reticular cells enwrap sinusoids and megakaryocytes

The BM microenvironment is composed of a variety of stromal reticular cells, which are derived from mesenchymal stem cells [77]. Despite being a heterogeneous cell population with a lack of one common (or yet unknown) specific lineage marker, these cells share several characteristics, such as the expression of typical mesenchymal markers (CD105, CD90, CD73) and their perivascular localization and are therefore being referred to as “pericytes” [78]. Several studies using reporter mouse strains e.g., Nestin-GFP mice, have shown that BM pericytes produce regulatory cytokines and chemokines crucial for HSC homeostasis, for instance CXCL12, that was formally referred to as stromal cell-derived factor 1α (SDF-1α) [3, 16, 79]. Depletion of pericytes that express high amounts of CXCL12, so called CXCL12-abundant reticular cells, leads to reduced proliferation, and induces early myeloid differentiation of HSCs demonstrating the role of CAR cells in HSC maintenance [3]. A recent report from Gomariz et al. demonstrated that CAR cells cover the murine bone marrow vasculature suggesting that virtually all BM resident cells are in contact to CAR cells. Considering their close association to SECs and the vascular niche however, there are only few reports on the interaction of CAR cells with MKs [80, 81]. We therefore aimed to study (1) the localization and distribution of CAR cells in regard to the BM vasculature and MKs as well as (2) the interaction of CAR cells with transendothelial MK protrusions at the site of direct vessel wall contact by visualization of CAR cells, sinusoids and MKs with different microscopy techniques.

For the following experiments we used a reporter mouse line in which the red-fluorescent protein dsRed is expressed under control of the CXCL12-promoter (dsRed^{CXCL12}) [73]. Femurs of these mice were subjected to longitudinal thin cryosectioning and multicolor IF-staining for CLSM. Whole femur imaging of one focal plane showed an extensive distribution pattern of CAR cells within the BM and co-localization with CD105^{+} sinusoids (Fig. 6A, inset), which is in line with the observations described in previous studies.

In addition to thin sectioning (7 µm), we adopted a protocol to generate thick cryosections (>200 µm) with subsequent optical clearing [15]. This allows to generate high-resolution three-dimensional images of CAR cell structure and the interaction surface of CAR cells with vessels and MKs without applying complex microscopic methods like light sheet fluorescence microscopy (LSFM) [82]. This imaging technique enables deep penetration of light into the BM and relies on efficient decalcification of bones and dehydration for optical clearing with the organic solvents benzyl alcohol and benzyl benzoate (BABB). BABB is known to destroy the integrity of endogenous fluorophores like GFP or dsRed. The protocol introduced by Gomariz et al. uses a water-soluble clearing reagent making dehydration unnecessary and thereby preserving the endogenous fluorescence. Maximum projection of ten optical sections from a 170 µm z-stack (Fig. 6B) revealed a dense network of CAR cells which is underappreciated when merely one optical section is depicted. Reticular cells ensheath ECM fibers and provide structural stability by forming thin cellular extensions throughout the BM that became visible with higher magnification. CAR cell extensions, as shown in Fig. 6C, create contact areas both with MKs that reside directly at sinusoids as well as MKs in the BM cavity, suggesting interplay of both cell types.

These results demonstrate that with the here newly established and adapted microscopic techniques used for our analyses, we can achieve sufficient tissue penetration and adequate resolution to generate 3D reconstruction of BM volumes on a cellular level by maintaining a sufficient three-dimensional tissue integrity.

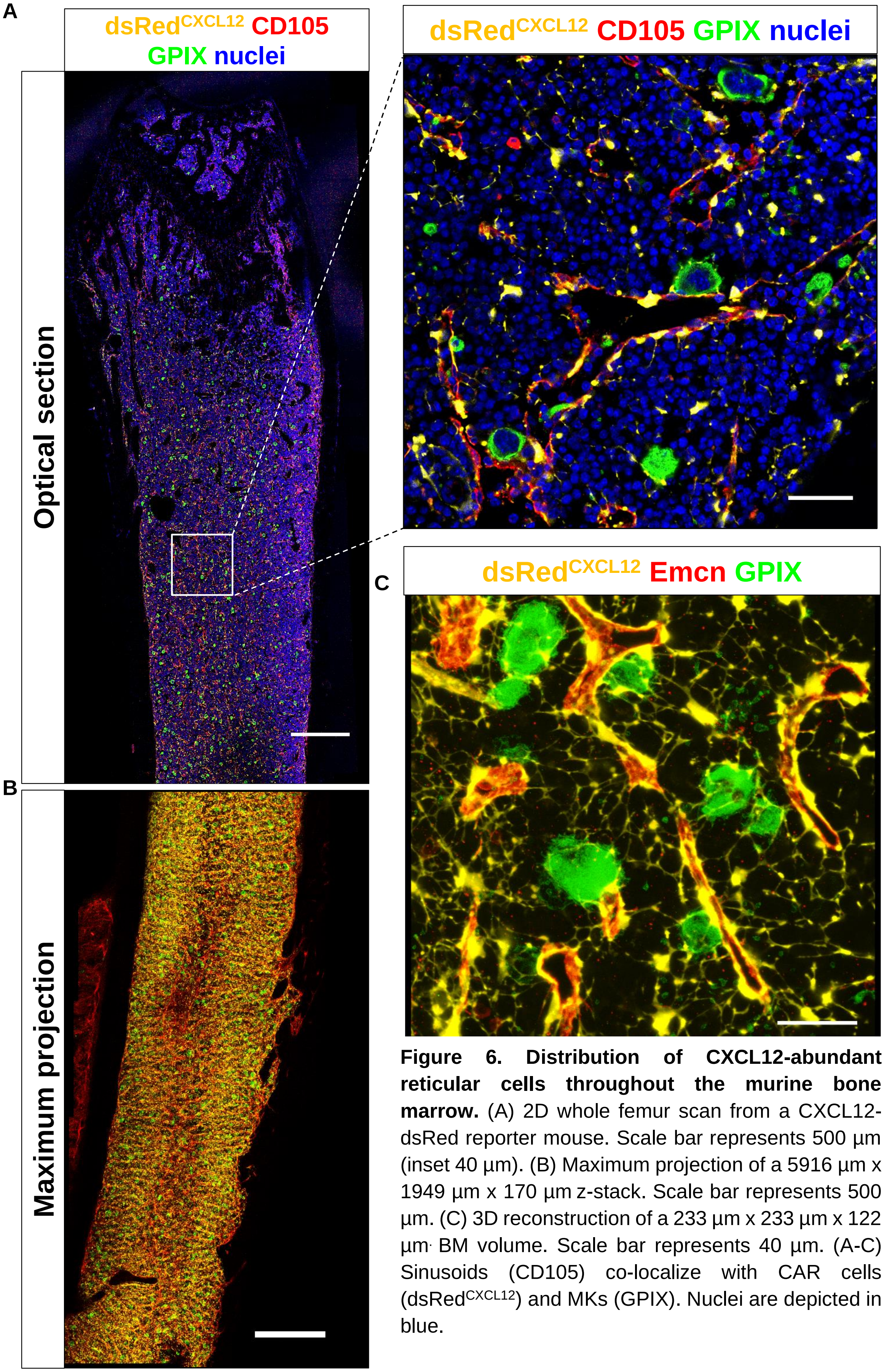

Figure 6. Distribution of CXCL12-abundant reticular cells throughout the murine bone marrow. (A) 2D whole femur scan from a CXCL12-dsRed reporter mouse. Scale bar represents 500 µm (inset 40 µm). (B) Maximum projection of a 5916 µm x 1949 µm x 170 µm z-stack. Scale bar represents 500 µm. (C) 3D reconstruction of a 233 µm x 233 µm x 122 µm BM volume. Scale bar represents 40 µm. (A-C) Sinusoids (CD105) co-localize with CAR cells (dsRed^{CXCL12}) and MKs (GPIX). Nuclei are depicted in blue.

3.1.2. CAR cells direct MK protrusions across the BM sinus wall

The ultrastructure of the vessel wall and perivascular cells has been studied by diverse microscopic techniques, especially transmission electron microscopy (TEM), that have shaped the current concept of platelet release *in situ* and *in vivo*. So far, however, there are no reports on the interaction of RCs or particularly CAR cells with proplatelet-forming MKs. We thus sought to apply the imaging approach described in the previous section to femur cryosections of CXCL12-dsRed reporter mice, which allows mapping of CAR cells as well as the quantification of CAR cell/MK interaction sites at the BM vascular niche in a three-dimensional context. The results presented in the following chapter have been published in [73].

We first used 2D images of seven whole femurs scans from CXCL12-dsRed reporter mice to analyze the areas of MK/vessel wall interaction. MKs that reside at BM sinusoids polarize towards the vessel and build cytoplasmic protrusions across the endothelial barrier to shed (pro-)platelets into the blood stream. At the sites of SEC penetration by MKs, CAR cells were absent while the endothelial lining appeared to be interrupted (Fig. 7Ai). In contrast, resting MKs, which reside directly at SECs, were in close contact to CAR cell extensions that cover the endothelial barrier (Fig. 7Aii). The total MK number around the complete femur section was determined to be n = 3679, while the number of vessel-protruding MKs was 54 and thus only 1.5% of the total MK count. We could determine that the majority of SEC-protruding MKs (42 of 54) was not in contact to CAR cells (Fig. 7B).

With the help of 3D BM reconstructions, as described in the previous section, we further analyzed proplatelet-forming MKs. Femurs from two CXCL12-dsRed mice were used for thick sectioning and co-staining of vessels (Emcn) with MKs (GPIX). A total of six BM volumes ranging from 16 µm to 170 µm (200 to 400 z-sections) were then captured by confocal microscopy. This microanatomical visualization of vessel-protruding MKs revealed pore formation in the Emcn$^+$ endothelial lining (Fig. 8A) and clustering of CAR cell extensions around the pore (Fig. 8A, inset).

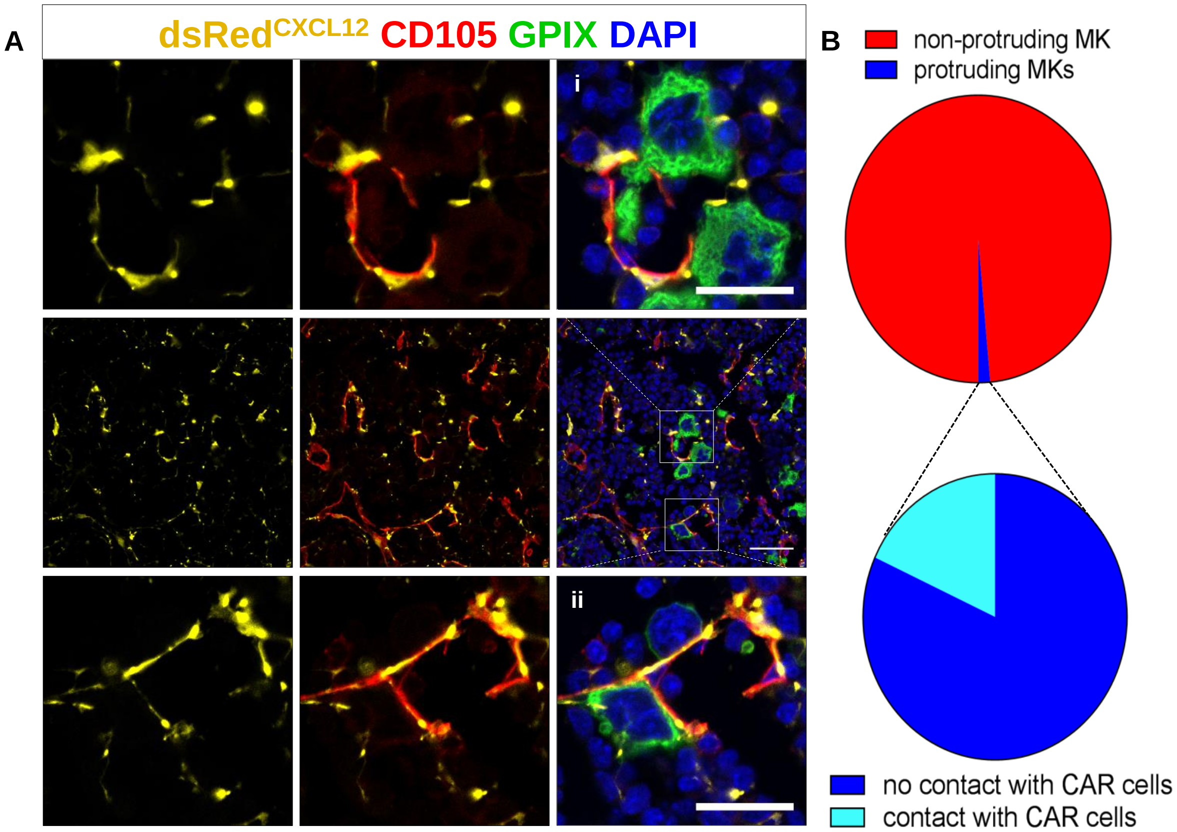

Figure 7. Resting MKs are in contact to CAR cells. (A) Representative images of CXCL12-dsRed mouse femurs. dsRed^{+} CAR cells (dsRed$^{\text{CXCL12}}$) have a mesh-like distribution in the BM (middle row). Non-protruding MKs (GPIX) are in contact with CAR cells (bottom row, ii). At sites of proplatelet formation the endothelial lining (CD105) shows pores and CAR cell staining was not detectable (top row, i). Scale bars represent 40 µm (insets 20 µm). (B) For quantification of MK-CAR cell interaction seven whole femur tilescans with a total number of 3679 MKs were analyzed. 1.5% of total MKs are breaching the endothelial lining, of which less than 25% are in contact to CAR cells. The figure was adapted from [73].

We next performed SBF-SEM, segmentation and 3D reconstruction of different cellular components at the site of vessel penetration for ultrastructural analysis of MK protrusions. Proplatelets inside blood vessels (as shown in Fig. 8B) were still connected to the MK through a newly formed pore in the SEC (Fig. 8B,D, black arrows). Fine extensions interconnect proplatelet fragments and anchor them to the luminal SEC surface (Fig. 8B,C, red arrowhead). At the site of transendothelial passage reticular cells seem to be locally retracted (Fig. 8D, RC1, RC3), independently confirming our confocal microscopy data. These results imply that CAR cells may play an unexpected role as gatekeepers of proplatelet formation enabling or rather preventing MK-SEC interaction.

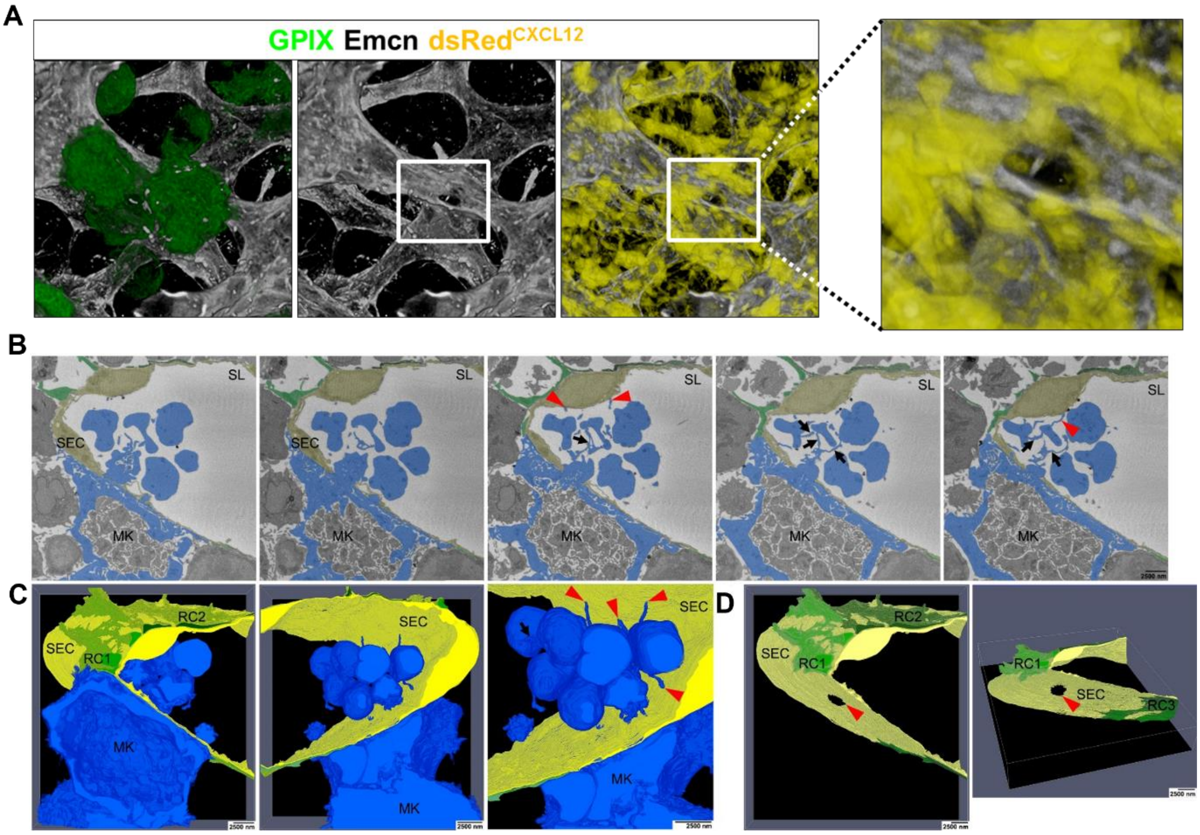

Figure 8. MKs protrude BM vessels by transendothelial pore formation. (A) Representative 3D reconstructed BM volumes showing vessel (Emcn) penetration by MKs (GPIX). CAR cells (dsRed^{CXCL12}) surround the SEC aperture. (B) Single SBF-SEM slices show a MK (blue) adjacent to SECs (yellow) and locally retracted RCs (green). Fine cellular protrusions that interconnect proplatelets (black arrows) and SECs (red arrowheads). (C) 3D reconstruction of a 5 µm BM volume consisting of 168 sections. Images (B), (C) and (D) were generated in collaboration with PD Dr. Nicole Wagner and Prof. Dr. Süleyman Ergün (Institute of Anatomy and Cell Biology, University of Würzburg). SL: sinusoidal lumen, RC: reticular cell. This figure was adapted from [73].

3.2. Total body irradiation-induced BM remodeling and the role of matrix metalloproteinase 9

Total body irradiation is a commonly used myeloablative conditioning regimen prior to HSCT. Myeloablation following TBI leads to a rapid depletion of peripheral blood cells, including platelets, and consequently triggers neogenesis of hematopoietic cells to counteract pancytopenia. Although TBI has been used for over 50 years for therapeutic purposes, the effect of radiation injury on the BM and on thrombopoiesis is not yet fully understood. As described in the previous section, we have studied the transendothelial MKs passage and PPF under steady state conditions. In the following series of experiments, we thus aimed to investigate PPF at the radiation-injured vessel wall and to decipher the underlying mechanisms of TBI-induced BM remodeling in an irradiation-based mouse model.

3.2.1. TBI leads to rapid vasodilation and degradation of ECM proteins

Several reports describe a transient expansion of the vessel lumen, a process designated as vasodilation, and vascular damage in the first days after myeloablation [83, 84]. Yet it is not clear how fast vasodilation occurs in the mouse (femur) and how the other components of the vascular wall, ECM proteins and pericytes, are influenced after radiation injury. Considering that the vascular BM microenvironment is the primary MK niche and the site of thrombopoiesis, we also sought to analyze MKs in the radioablated BM. In a first set of experiments, we hence studied the kinetics of BM remodeling after sublethal (5Gy) TBI to determine the time points for further analyses. Wildtype C57B6/J mice were irradiated, and femurs were harvested for IF-staining of vessels, MKs and nuclei. Vasodilation was quantified by measurement of the vessel-to-vessel distance.

Vasodilation was plainly visible on day one (24 hours) and most pronounced on day three (72 hours) after TBI (Fig. 9A,B), which corresponds to observations described in the literature. In line with the increased vessel lumen a reduced intersinusoidal distance after TBI was determined (Fig. 9B). Because the exact onset of vasodilation is yet unknown, the time points of analysis were further reduced to six and one hours after TBI. Unexpectedly, already as early as one hour after TBI a beginning vasodilation could be measured in the form of a reduced intersinusoidal distance, and after six hours vessel dilation was readily visible without quantification (Fig. 9A,B). Concomitantly with the vascular remodeling, the number of MKs in the BM increased from 12 ± 4.8 to 15 ± 4.3 MKs per visual field on day one after TBI and was then reduced by day seven to 3 ± 1.9 MKs per field of view (Fig. 9C).

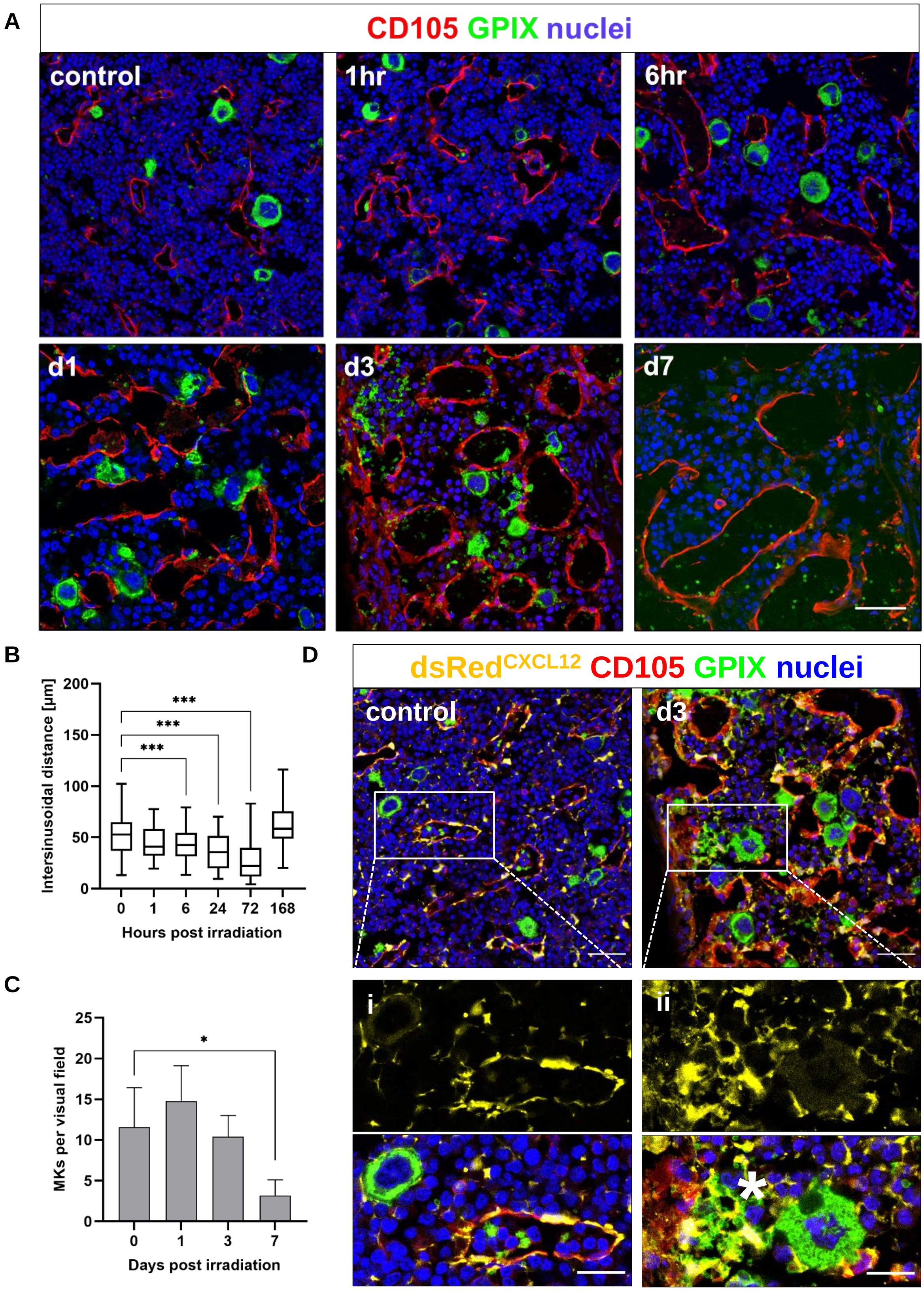

Figure 9. Total body irradiation induced massive remodeling of the BM vasculature. (A) IF staining of BM sinusoids and MKs at early time points after 5Gy TBI. One of three representative experiments is shown. (B) The median intersinusoidal distance was measured after 5Gy TBI. Box plot whiskers represent 5 resp. 95% percentile. (C) Quantification of MKs per 388 µm x 388 µm visual field. Values are depicted as mean ± SD. (D) CAR-cell (dsRed^{CXCL12}) shape changed from a fibroblast-like phenotype (i) to a clustered morphology at vasodilated sinusoids (ii). Ectopic PLP release is marked by a white

asterisk. Scale bars represent 40 µm. (A,D) BM sinusoids were visualized by anti-CD105 and MKs by anti-GPIX antibody staining. Nuclei were counterstained with DAPI. (B-C) For quantitative analyses BM from at least three mice per time point and at least five visual fields per femur were analyzed. Experiment C was technically conducted by Dr. Daniela Semeniak. Asterisks mark statistically significant differences of the mean compared to untreated controls (time point zero). (* $P < 0.05$; *** $P < 0.001$).

Irradiation of CXCL12-dsRed reporter mice revealed additionally a retraction of CAR cell extensions, resulting in a strongly clustered morphology (Fig. 9D, i and ii). Furthermore, an increased number of GPIX$^+$ platelet-like particles (PLPs) in the marrow cavity was detected (Fig. 9D, asterisk). A similar ectopic platelet release is rare and has been reported in mice deficient for the actin-binding proteins Arp2/3, WASP or ADAP [85-87] suggesting that there are MK-intrinsic mechanisms regulating vessel-directed proplatelet formation. Our observations in the irradiated BM imply that CAR cells may be additional regulators of proplatelet formation, which is consistent with the results presented in section 3.1.

Previous work of our and other research groups could confirm that different isoforms of collagens and laminins are expressed at distinct sites in the BM, especially around blood vessels [47, 50]. We were next interested whether TBI had an effect on the composition and the localization of the distinct matrix proteins. In order to address this question, we took advantage of a series of antibodies that allow to selectively stain for relevant collagen and laminin isoforms such as collagen type I (Col I), collagen type IV (Col IV) or laminin α5 (Lam α5). Expression analysis of these sinus basement membrane proteins by IF labeling showed reduced staining for collagen type IV and laminin α5 specifically at sinusoids (Fig. 10A, Fig. 11A), while the amount and localization of collagen type I was overall unaltered after irradiation (Fig. 10B). In summary, these observations indicate that platelet generation in the irradiated BM is disturbed by the eradication of MKs and radiation damage to the vascular wall including ECM proteins and CAR cells. For all further experiments the BM was analyzed on day one, day three/four and day seven after TBI, if not indicated otherwise. This allows to capture early time points where the process initiates as well as the time points when the major BM remodeling has occurred.

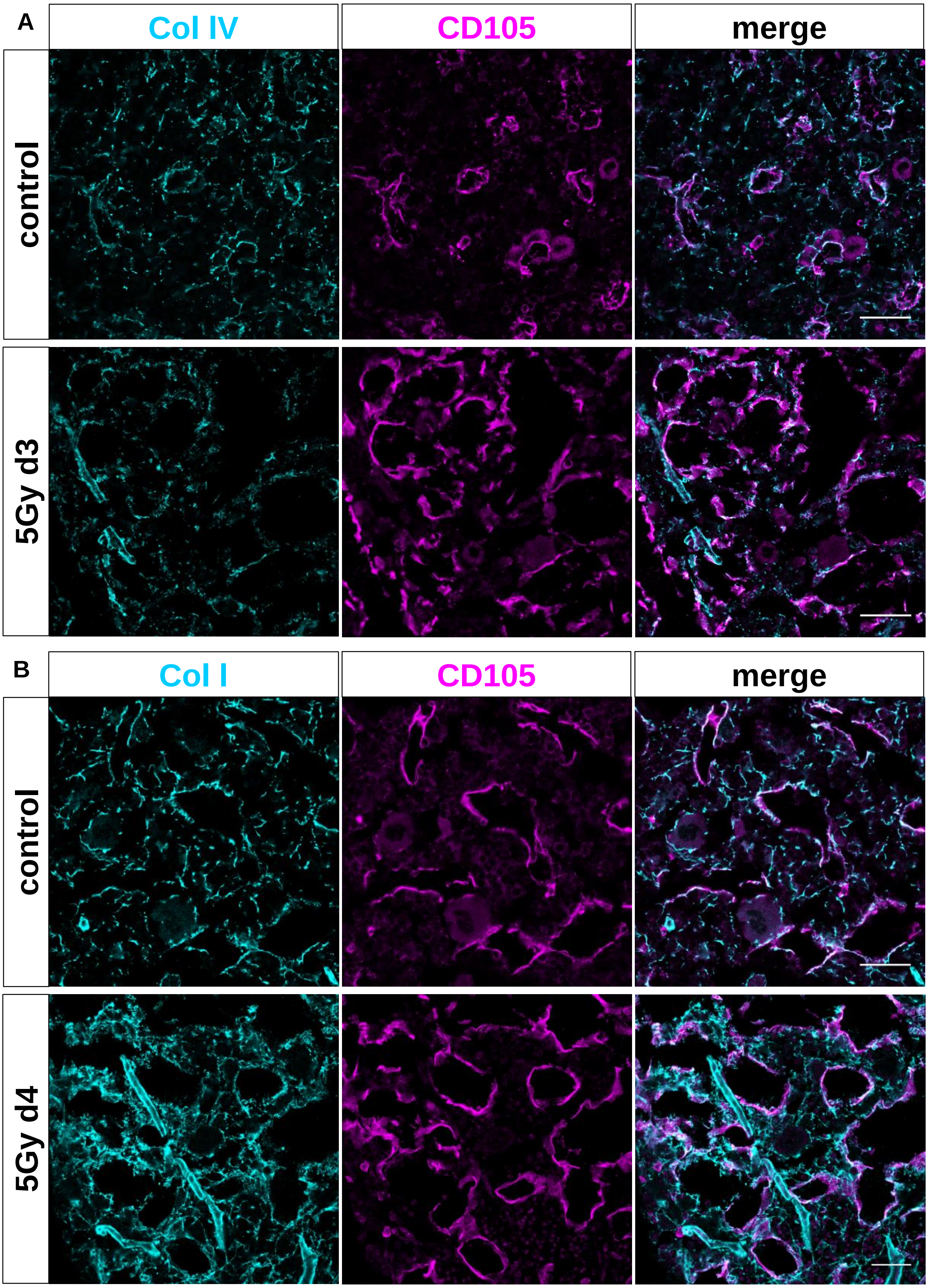

Figure 10. TBI-induced loss of collagen type IV at BM sinusoids. (A) In the non-irradiated BM (control), collagen type IV (cyan) co-localizes with vessels (CD105) but could also be partly detected in the marrow cavity. In contrast, on day three (d3) after 5 Gy TBI reduced positive staining for collagen type IV could be detected. (B) Collagen type I (cyan) is distributed within the BM cavity and could be partly found at sinusoids and arterioles. On day four (d4) after sublethal TBI collagen type I was still present at the endothelial lining. Scale bars represent 40 µm. One of at least three experiments is shown.

3.2.2. Matrix metalloproteinase 9 activity is increased after TBI

While ECM proteins undergo constant remodeling during tissue homeostasis, we have demonstrated that TBI induces a sinusoids-specific reduction of collagen type IV and laminin α5 but not collagen type I, suggesting a regulated degradation process. The primary collagen- and laminin-cleaving MMPs in the BM are the gelatinases MMP9 and MMP2, making them *bona fide* candidates for the ECM remodeling after TBI. Thus, we hypothesized that MMP2 and MMP9 catalyze the degradation of collagen type IV and laminin α5 after radiation injury and aimed to dissect the role of these MMPs in our irradiation mouse model.

Immunoblot analysis of whole BM lysates from irradiated wildtype mice revealed MMP9 expression on day one and day seven after TBI (Fig. 11B). Most MMPs are initially expressed and secreted as latent zymogens with a pro-peptide domain that needs to be cleaved for activation. We therefore used BM lysates from wildtype and MMP9-deficient (MMP9$^{-/-}$) mice to additionally study MMP activity by gelatin-zymography (Fig. 11C). MMP9 activity was increased in wildtype BM lysates on day one and day seven after 5 Gy TBI, which is reflected by larger unstained clear bands in the zymogram and which is in line with the expression pattern observed by immunoblotting, suggesting a direct relationship between expression and activity. In contrast, no MMP activity was detectable in lysates from MMP9-deficient mice, which implies that the zymographic activity in our assay is indeed derived from MMP9. Importantly, no compensatory activation of MMP2 could be observed. We thus focused on MMP9 for further experiments.

To rule out the possibility that reduced detection of ECM proteins after irradiation was due to masking of antibody-binding sites, we used an antibody that specifically recognizes the cleavage sites of degraded collagen (cleaved collagen) for immunoblotting. There was no signal in lysates of untreated BM, but one day after TBI this cleaved collagen peptide became detectable in wildtype lysates and to a smaller degree also in MMP9$^{-/-}$ BM lysates (Fig. 11D), suggesting residual collagenolytic activity in MMP9-deficient BM. Interestingly, the highest amount of cleaved collagen was detectable on day three after TBI, when MMP9 expression and activity was lowest, indicating that active MMP9 is consumed, and that activity precedes accumulation of cleaved collagen in the BM. Taken together, these results show that collagens are actively degraded after irradiation and that MMP9 is likely the primary matrix metalloproteinase mediating collagenolysis in this setting.

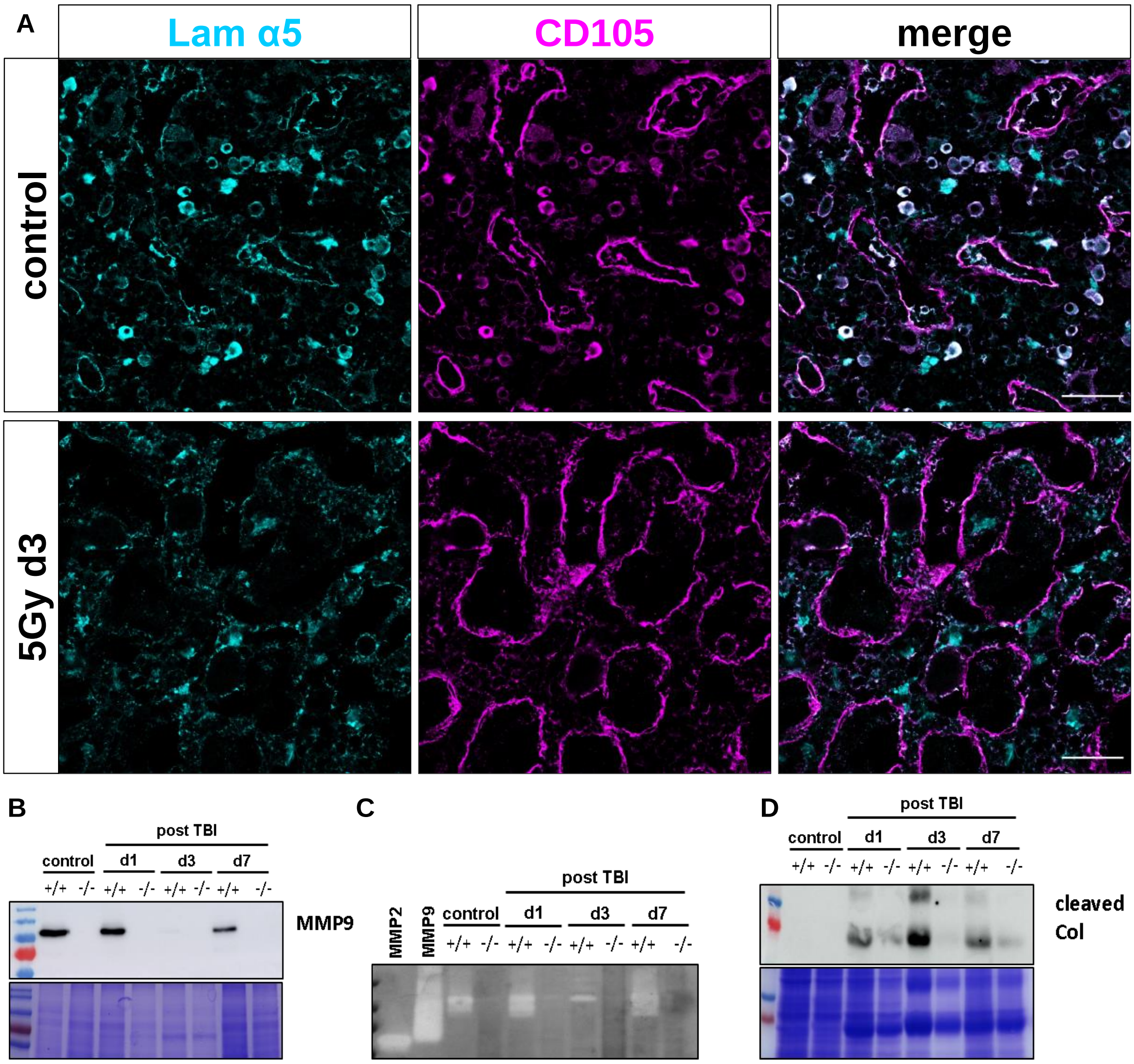

Figure 11. ECM degradation after TBI is mediated by MMP9. (A) In the non-irradiated BM laminin α5 (Lam α5) is co-localized with vessels (CD105) and arterioles. On day three after 5 Gy TBI laminin α5 is not detectable anymore. (B) BM lysates from MMP9$^{-/-}$ mice (-/-) show no MMP expression whereas MMP9 in lysates from wildtype mice (+/+) was increased on d1 and d7 after irradiation. (C) Gelatin-zymography of whole BM lysates of non-irradiated (control) and irradiated MMP9$^{+/+}$ and MMP9$^{-/-}$ mice showed increased MMP activity in the BM. (D) Immunoblot analysis of whole BM lysates from MMP9$^{+/+}$ mice reveal increased cleaved collagen peptide expression, while there was no activity in the BM of MMP9$^{-/-}$ mice. One of three representative experiments each is shown.

3.2.3. *In situ* zymography with unfixed, calcified femur sections

We have demonstrated that TBI induces sinusoid-specific degradation of collagen type IV, which is connected with increased MMP9 activity in gelatin-zymography assays (Fig. 11). This type of assay offers an overview of MMP activity in a tissue lysate but does not provide information about the subcellular localization of MMP activity *in situ*, making it impossible to determine the exact site of activity i.e., whether MMP activity after TBI is specifically increased at sinusoids. We thus aimed to combine the detection of proteolytically active MMP9 with an assay providing spatial information about MMP9 activity by establishing an *in situ* zymography assay.

As enzyme activity becomes abrogated due to fixation with PFA, we decided to establish a zymography protocol using unfixed, non-decalcified femur sections. Measurement of MMP9 activity was achieved by incubating femur sections with a dye-quenched (DQ), FITC-conjugated MMP-substrate (DQ-gelatin, DQ-collagen type I or DQ-collagen type IV) that becomes fluorescent only upon proteolytic cleavage. Femur sections were washed post incubation and the fluorescent light which is emitted after substrate cleavage was then detected using CLSM. This technique provides information on both, signal intensity, as well as on the topologic information in respect to its localization (vessel, MKs etc.). As MMPs are to some extend redundant in substrate specificity, MMP9-deficient mice were used as a negative control to estimate the contribution of MMP9 to DQ-substrate degradation. The highest MMP activity, which is reflected by bright fluorescence, was detectable in a distinct subset of cells, which partly occur in clusters within the bone marrow (Fig. 12A). MKs, recognizable by their characteristic size and nucleus morphology even without specific staining, were mostly negative for the DQ-signal, indicating that MKs play no or only a minor role for MMP activity.

There are a number of collagen-cleaving MMPs besides MMP9 and MMP2 expressed in the BM. We therefore aimed to determine the degree of DQ-substrate degradation that is mediated by other metalloproteinases. For this, *in situ* zymography was performed using DQ-gelatin, as gelatin is a mixture of several collagen isoforms and thus can serve as a substrate for a variety of MMPs. The contribution of MMPs to DQ-gelatin cleavage was confirmed by preincubation of femur sections with inhibitors that exhibit different levels of specificity towards MMPs. Phenylmethylsulfonyl fluoride (PMSF) is a non-specific protease inhibitor routinely used for protein lysate preparation. GM6001 inhibits MMPs on a broad spectrum and was originally designed for cancer treatment. SB-3CT is a selective MMP2/MMP9 mechanism-based inhibitor (in contrast to the zinc-chelator GM6001). In order to determine DQ-gelatin degradation more accurately, the DQ-gelatin signal intensity was measured and normalized to the image area (Fig. 12B,C).

The DQ-signal intensity of GM6001 treated femur sections was on average at 40% of vehicle control levels, while inhibition of MMP2 and MMP9 with SB-3CT led to 32% of control fluorescence intensity (Fig. 12B). General inhibition of proteases with PMSF resulted in 26% of control signal intensity. This finding indicates that while proteases and other MMPs might contribute to DQ-gelatin cleavage, proteolytic activity is predominantly mediated by MMP2 and MMP9.

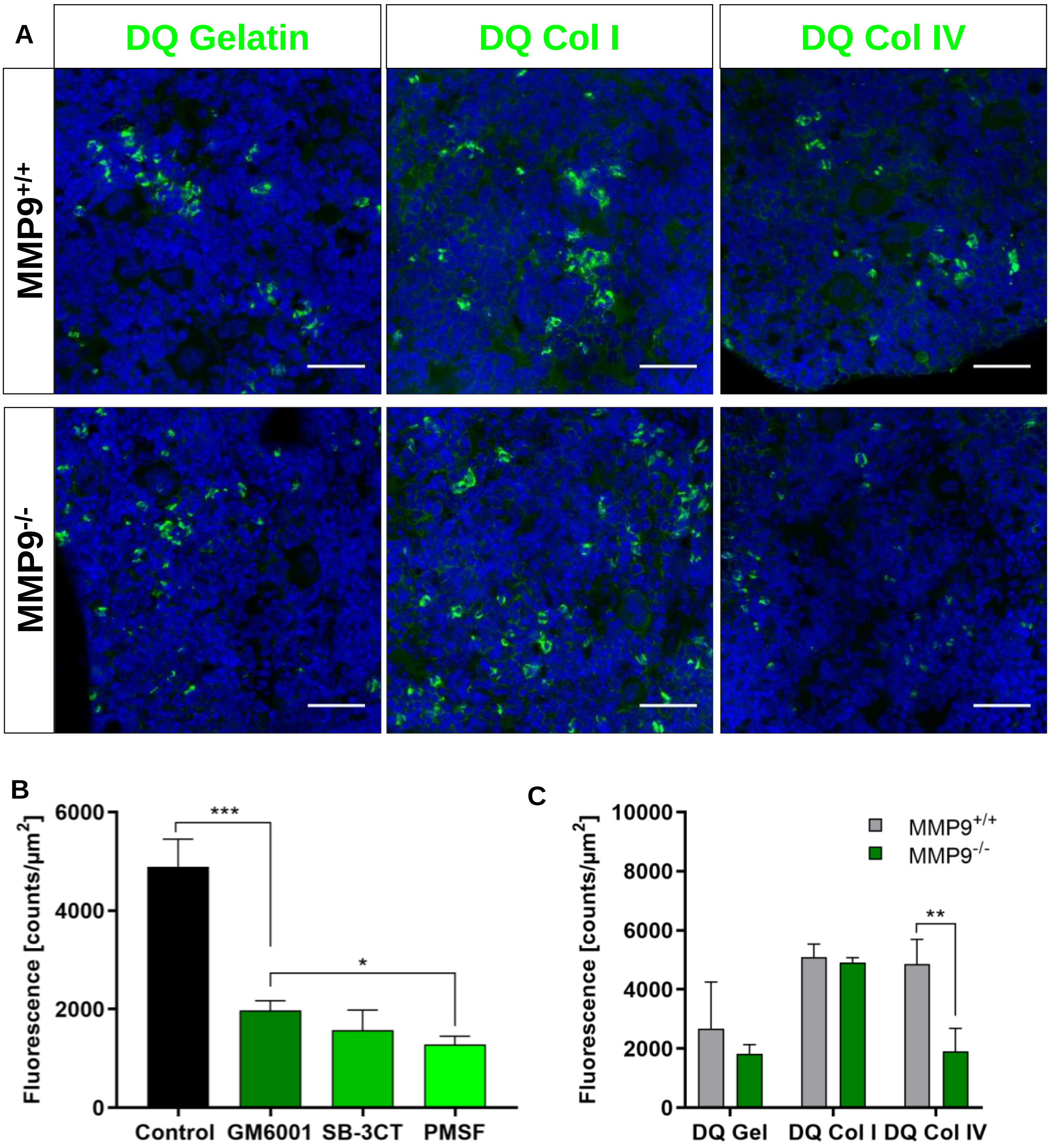

Figure 12. Detection and localization of MMP activity by *in situ* zymography. (A) Unfixed, calcified femur sections from wildtype and MMP9 knockout mice were subjected to *in situ* zymography with DQ-gelatin, DQ-collagen type I, or type IV. Scale bars represent 40 µm. (B) Quantification of fluorescence emitted by cleaved DQ-gelatin after MMP-inhibitor treatment. (C) Measurement of DQ-fluorescence shows that degradation of DQ-collagen type IV was reduced in MMP9$^{-/-}$ BM. (B-C) For fluorescence measurement at least five visual fields per femur were analyzed. One out of three representative experiments is shown. Bar graphs represent mean ± SD. Asterisks mark statistically significant differences of the mean compared to vehicle treated controls (black bar). (* $P < 0.05$; ** $P < 0.01$; *** $P < 0.001$).

Although both MMP2 and MMP9 are able to degrade gelatin, the main substrate for MMP2 is collagen type I and for MMP9 collagen type IV. We therefore assessed the individual roles of MMP2 and MMP9 in proteolysis by using DQ-collagen type I and type IV for *in situ* zymography. Wildtype mice exhibit a 90% increased signal intensity for DQ-collagen type I and

80% for DQ-collagen type IV compared to the fluorescence levels measured with DQ-gelatin (Fig. 12C). In MMP9$^{-/-}$ mice the DQ-collagen type I signal was doubled compared to DQ-gelatin. Importantly, only a marginal increase in fluorescence intensity was measured when *in situ* zymography was performed with DQ-collagen type IV in MMP9 knockout mice (15% higher than DQ-gelatin fluorescence intensity). These results suggest that DQ-collagen type IV is mainly degraded by MMP9, since DQ-collagen type IV cleavage is attenuated when MMP9 is absent. In summary, we were able to establish a tool set for studying the role of MMP9 in ECM remodeling where we can combine quantification of MMP9 activity with spatial information about proteolysis.

3.2.4. *In situ* Zymography confirms increased MMP9 activity after TBI

TBI has two main effects: it generates space in the recipient BM for the new hematopoietic system and it eradicates malignant cells like cancer stem cells. While the latter requires a higher dosage (lethal irradiation with 10Gy), sublethal irradiation (5Gy) already leads to massive rearrangement of the BM matrix. We could show that during TBI-induced BM matrix remodeling collagen type IV is specifically degraded at BM sinusoids, while MMP9 activity (but not MMP2 activity) is increased (Fig. 10 and Fig. 11), hinting towards a role of MMP9 in mediating collagen cleavage after TBI. Moreover, with use of the newly established *in situ* zymography technique described in the previous section, we could demonstrate that collagen type IV is the main substrate of MMP9 in the BM, thereby further corroborating its function during BM remodeling. We therefore hypothesized that MMP9 activity is increased around sinusoids after TBI and that this leads to vessel-specific collagen degradation. In a next set of experiments, we thus used the newly established zymography technique to study MMP9 activity after sublethal TBI *in situ* by using DQ-gelatin, DQ-collagen type I and type IV as substrates.

After TBI MMP activity was mainly detected intracellularly, as representatively shown for DQ-collagen type IV in Figure 13A. The DQ-fluorescence signal peaked on day one after TBI and was mostly absent by day seven (Fig. 13A). Compared to wildtype mice, MMP9$^{-/-}$ mice did not show an apparent increase in DQ-collagen type IV fluorescence after irradiation.

When we used DQ-gelatin for *in situ* zymography after TBI, we detected a tendency towards an increase in fluorescence intensity on day one in both MMP9$^{+/+}$ and MMP9$^{-/-}$ mice (44% in wildtypes and 6 % in knockouts compared to respective values on day zero, Fig. 13B). By day seven after TBI DQ-intensity was significantly reduced to 30% of control levels (day zero) in MMP9 knockout mice. Quantification of DQ-collagen type I fluorescence revealed increased MMP activity in MMP9$^{-/-}$ mice on day one after TBI, while we detected weak zymographic activity in MMP9$^{+/+}$ mice until day three after irradiation (Fig. 13C). When we measured DQ-collagen type IV fluorescence in irradiated MMP9 wildtype mice (Fig. 13D) we found a transiently increased fluorescence intensity on day one after TBI corresponding to the fluorescence shown in Fig 13A. These elevated intensity levels were again absent in MMP9$^{-/-}$ mice. This set of data thus clearly indicates that after irradiation MMP activity is increased, confirming the gelatin-zymography results shown in Fig. 11C, and that TBI-induced degradation of collagen type IV is mainly mediated by MMP9.

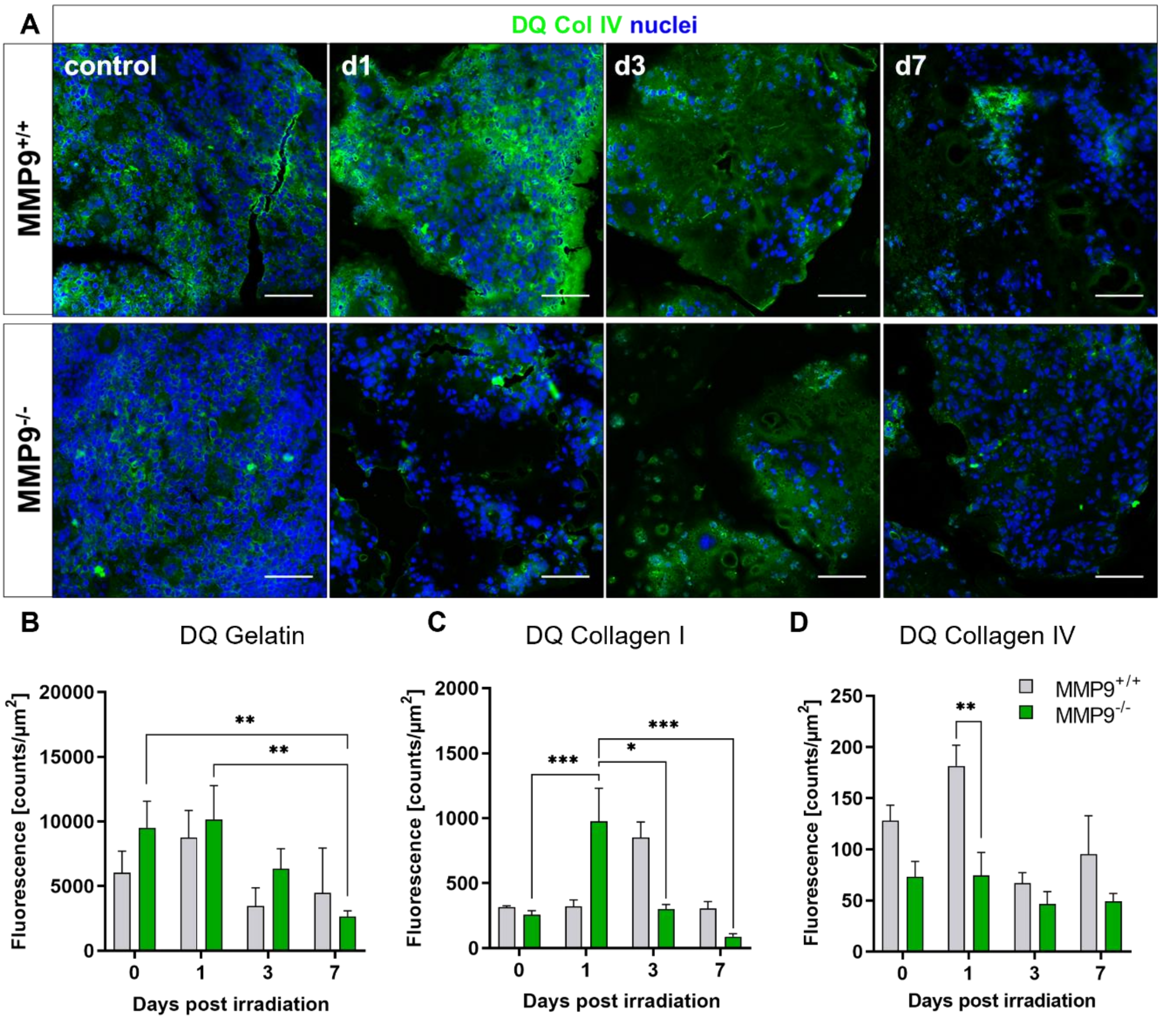

Figure 13. *in situ* MMP activity is increased after TBI. (A) Representative *in situ* zymography images with DQ-collagen type IV after 5Gy TBI. (B) Quantification of fluorescence emitted from DQ-gelatin, (C) DQ-collagen type I and (D) DQ-collagen type IV in MMP9$^{+/+}$ and MMP9$^{-/-}$ BM. For fluorescence measurements at least five visual fields per femur were analyzed. One out of three representative experiments is shown, DQ collagen type I was used in one experiment. (B-D) Data is presented as mean ± SD. Asterisks mark statistically significant differences of the pairwise comparisons as indicated. (* $P < 0.05$; ** $P < 0.01$; *** $P < 0.001$).

3.2.5. MMP9-deficiency leads to prolonged vasodilation after TBI

Vascularization and angiogenesis require ECM degradation to release ECM-bound signaling molecules, like VEGF, and to facilitate cell migration, processes in which MMP9 is known to play an important role. The data presented in the previous sections suggest that MMP9 activity is increased after TBI which contributes to collagen degradation within the BM. We therefore hypothesized that MMP9 is not only involved in irradiation-induced ECM remodeling but also in the mechanisms leading to vasodilation.

In order to address this hypothesis experimentally wildtype and MMP9$^{-/-}$ mice were subjected to sublethal TBI and sacrificed to generate BM cryosections for IF-staining of sinusoids. The intersinusoidal distance was then measured to determine whether vasodilation is dependent on MMP9. Furthermore, we have studied the effect of MMP9-deficiency on MKs by IF-staining against GPIX and determination of MK number and size. On day three after TBI both MMP9$^{+/+}$ and MMP9$^{-/-}$ mice displayed massively dilated vessels (Fig. 14A). While the quantification of MK count and size showed no difference between wildtype and knockout mice (Fig. 14B,C), the median intersinusoidal distance on day seven after TBI was still significantly reduced in MMP9$^{-/-}$ mice compared to the wildtype controls (58.4 µm in wildtypes vs. 26.8 µm in knockouts), suggesting a delayed recovery of sinusoids in the absence of MMP9 (Fig. 14D). These observations imply that MMP9 is also involved in reconstitution of vessel size beyond its role in collagenolysis after TBI.

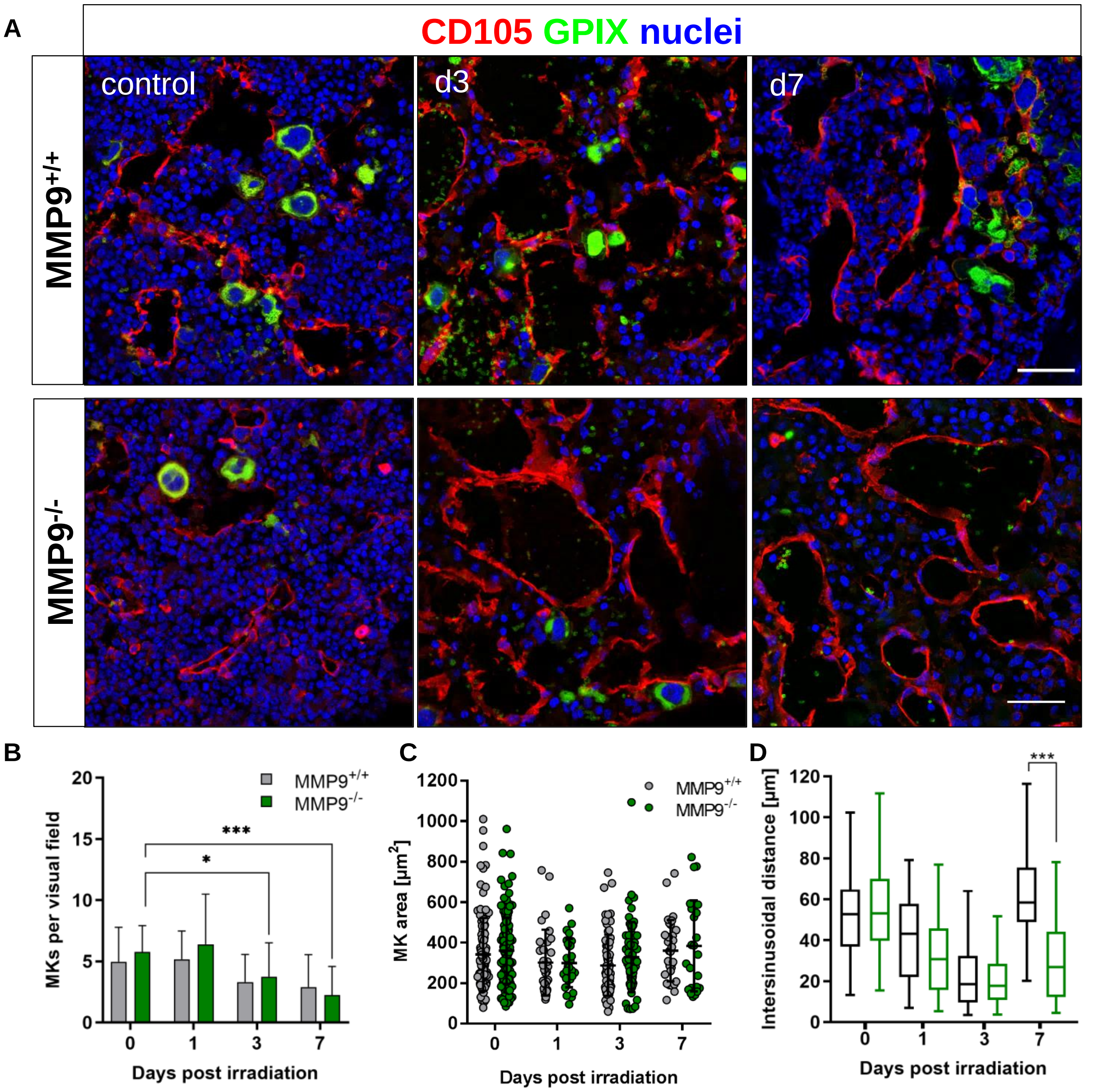

Figure 14. Increased vasodilation in MMP9-deficient mice after TBI. (A) IF-staining of sinusoids (CD105) revealed massive vasodilation after irradiation, while the number of MKs (GPIX) is reduced, independent of MMP9 expression. Nuclei were counterstained with DAPI. (B) Quantification of MK number and area (C) revealed no difference between MMP9$^{+/+}$ and MMP9$^{-/-}$ mice. Values are depicted as mean ± SD. (D) Measurement of the vessel-to-vessel distance in MMP9$^{+/+}$ and MMP9$^{-/-}$ mice on day seven after TBI. Box plot whiskers represent 5% resp. 95% percentile. (B-D) For quantifications bone marrow from three mice per time point and at least five visual fields per femur were analyzed. Asterisks mark statistically significant differences of the pairwise comparisons as indicated. (* $P < 0.05$; *** $P < 0.001$).

3.2.6. Loss of the laminin α5 chain does not affect the irradiated bone marrow

Laminins constitute a further key component of the vessel wall basement membrane. Most isoforms expressed in the BM were found to contain laminin α4- and α5-chains [88], with laminin α5 being detectable at both arterioles and sinusoids and laminin α4 exclusively at arterioles [14]. Laminins serve various functions, such as endothelial shear-induced mechanotransduction and barrier for the extravasation of immune cells [89, 90]. We have shown that laminin α5 expression is reduced at BM sinusoids after TBI (Fig. 10) and therefore questioned whether loss of laminin α5 has an influence on sinusoid structure as well as vessel permeability for MK protrusions in the native and irradiated BM.

In order to define how laminin α5 affects MKs and sinusoids before and after TBI we used the conditional Cre/loxP-system to obtain viable laminin α5 knockout mice. For this Lama5$^{flox/flox}$ mice were bred with mice that express the Cre-recombinase under control of the VE-cadherin promoter (Cdh5.Cre) yielding vessel-specific Lama5$^{flox/flox}$Cdh5.Cre^{+} mice (further referred to as Lama5^{KO}). Lama5$^{+/+}$Cdh5.Cre^{+} or Lama5$^{flox/flox}$Cdh5.Cre^{-} were used as controls (Lama5^{WT}) for the following analyses.

Sinusoid-specific degradation of laminin α5 was confirmed by immunofluorescence co-staining of laminin α5 with sinusoid markers in the Lama5^{WT} and Lama5^{KO} BM (Fig. 15A), providing a proof-of-principle that our conditional knockout approach resulted in the expected phenotype. Assessment of blood parameters from Lama5^{WT} and Lama5^{KO} mice revealed a slightly increased platelet count in laminin α5-deficient mice (849 ± 110.5x10^{3}/µl and 905 ± 155.6x10^{3}/µl) but otherwise no difference between Lama5^{WT} and Lama5^{KO} animals (Fig. 15B,C), suggesting that laminin α5 plays a negligible role for blood cell counts under steady-state conditions.

We next subjected Lama5^{WT} and Lama5^{KO} mice to sublethal TBI and subsequent CLSM analysis to define whether sinusoid-specific loss of laminin α5 influences MK numbers and recovery of sinusoids. The number of MKs on day three and seven after TBI was reduced in the BM of both wildtype and Lama5^{KO} mice while MK size was increased (Fig. 15D,E). Interestingly, MKs in Lama5^{KO} mice seemed to be divided into either very large or smaller sized MKs (Fig. 15E). The intersinusoidal distance as an indirect marker for vasodilation was comparable between Lama5^{WT} and Lama5^{KO} mice. In summary, these results imply that sinusoid-specific loss of the laminin α5 isoform has no impact on TBI-induced BM remodeling.

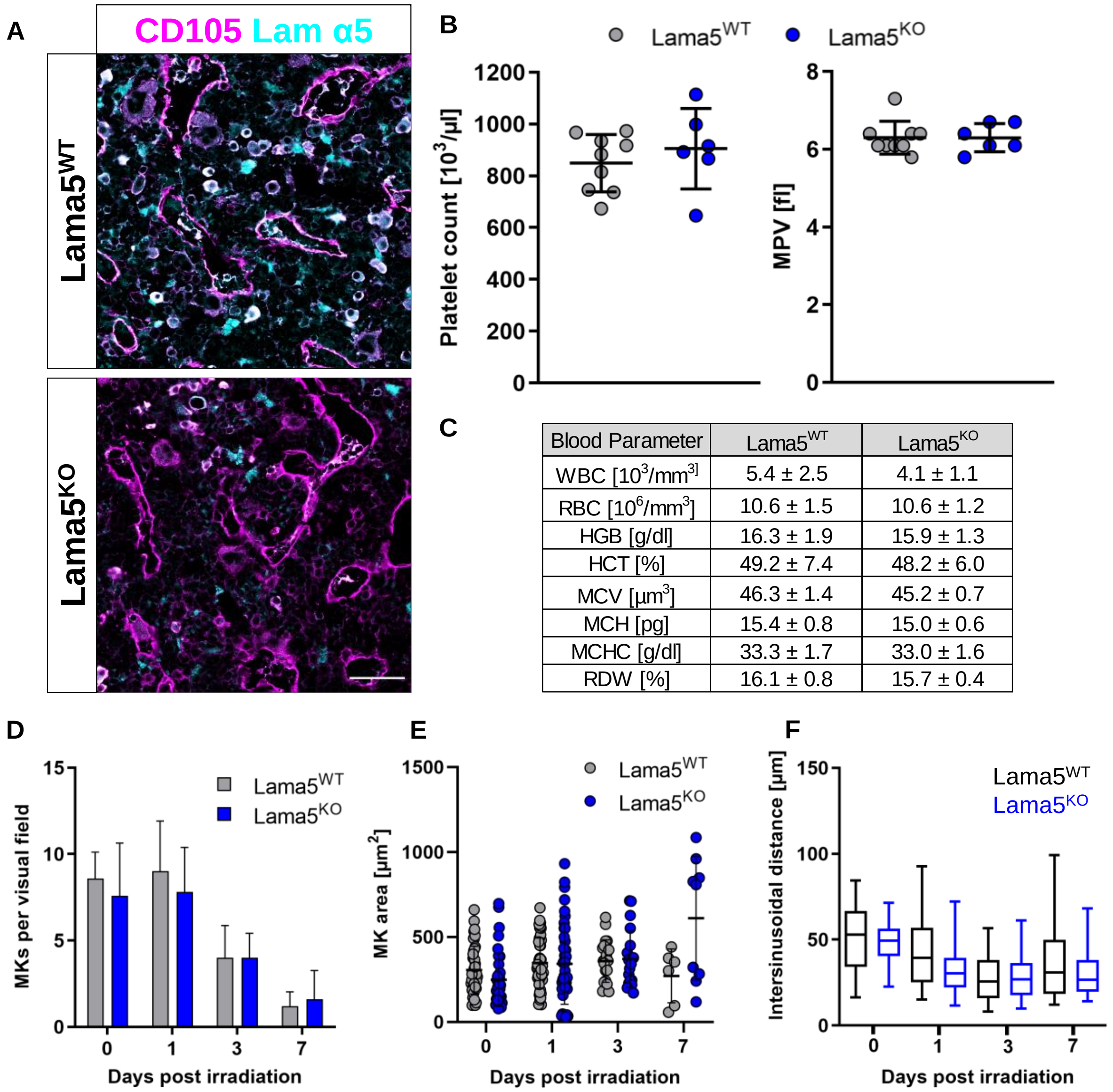

Blood Parameter	Lama5^{WT}	Lama5^{KO}
WBC [10^3/mm^3]	5.4 ± 2.5	4.1 ± 1.1
RBC [10^6/mm^3]	10.6 ± 1.5	10.6 ± 1.2
HGB [g/dl]	16.3 ± 1.9	15.9 ± 1.3
HCT [%]	49.2 ± 7.4	48.2 ± 6.0
MCV [µm^3]	46.3 ± 1.4	45.2 ± 0.7
MCH [pg]	15.4 ± 0.8	15.0 ± 0.6
MCHC [g/dl]	33.3 ± 1.7	33.0 ± 1.6
RDW [%]	16.1 ± 0.8	15.7 ± 0.4

Figure 15. Impact of laminin α5 knockout on blood cell counts, MKs and sinusoids. (A) IF-staining of laminin α5 (Lam α5) and sinusoids (CD105) in Lama5^{WT} and Lama5^{KO} mice. Scale bars represent 40 µm. (B) Platelet count and size was measured with an automated hematology analyzer (ScilVet). Each datapoint represents one mouse. (C) Comparable blood cell counts between Lama5^{WT} and Lama5^{KO} animals measured with ScilVet. WBC = white blood cells, RBC = red blood cells, HGB = hemoglobin, HCT = hematocrit, MCV = mean corpuscular volume, MCH = mean corpuscular hemoglobin, MCHC = mean corpuscular hemoglobin concentration, RDW = red blood cell distribution width. (D) The number of BM MKs per field of view is reduced after TBI both in Lama5WT and Lama5KO mice, while MK size (E) is increased. Values are depicted as mean ± SD. (F) Both Lama5^{WT} and Lama5^{KO} mice display a pronounced vasodilation after TBI as shown by a reduced intersinusoidal distance. Box plot whiskers represent 5% resp. 95% percentile. (D-F) For quantitative analysis two femurs per time point and genotype with five visual fields per femur were used.

3.3. The megakaryocytic niche and platelet engraftment after BM transplantation

Hematopoietic stem cell transplantation is often the last therapeutic option to treat life threatening diseases such as leukemia or bone marrow failure syndromes. Usually, mobilized peripheral blood stem cells (PBSCs) are used for transplantation. However, about 20% of European HSCT patients receive whole BM and in rare cases umbilical cord blood [91]. HSCT is typically accompanied with ablation of the recipient BM by TBI and/or chemotherapy. This procedure aims at eradicating malignant progenitor cells and at creating free niche sites in the recipient BM for the new graft.

The documentation of engraftment is essential to evaluate successful therapy and can be achieved by assessment of donor cells in the recipient blood and BM. Engraftment in human patients is specified as the first of three consecutive days with a neutrophil count of at least $0.5x10^9$/l and platelet count of more than $20x10^9$/l, as defined in the handbook of the European Society for Blood and Marrow Transplantation (EBMT) [69]. Around 20% to 30% of patients develop a long-lasting thrombocytopenia which harbors the risk of HSCT-related hemostatic complications and affects mortality [92, 93]. There are several known risk factors for a delayed platelet engraftment, such as the stem cells source or conditioning regimen. Yet, the underlying mechanism of long-lasting thrombocytopenia is not completely understood.

3.3.1. MK engraftment begins in the first days after transplantation

The conditioning regimen used prior to BM transplantation induces rapid remodeling of the hematopoietic compartment. So far it is not clear how this remodeling influences engraftment of donor cells. We therefore sought to analyze the changes during BM reconstitution after myeloablation by TBI and subsequent HSCT.

In an initial series of experiments, we established a transplantation mouse model to study the kinetics of MK engraftment. A reporter mouse strain that expresses the red fluorescent protein dsRed constitutively under control of the β-actin promoter ($Actb^{dsRed}$) was used as BM donor to enable the discrimination of all donor(-derived) cells from the recipient BM. Whole BM from $Actb^{dsRed}$ mice was intravenously transplanted into lethally irradiated wildtype mice for subsequent analysis of the recipient BM and blood by CLSM and flow cytometry at the time points indicated in Fig. 16A.

Within a period of seven days post HSCT the overall number of MKs was markedly reduced from over 600 MKs per whole femur scan on day zero to only 32 MKs on day seven (Fig. 16B). Concomitantly, the average MK size was increased from 383 ± 143 μm^2 on day zero to 492 ± 163.1 μm^2 on day seven and 520 ± 265.6 μm^2 on day 14, which hints towards a higher maturity degree of these MKs (Fig. 16C). Until day 14 after transplantation the overall MK count began to recover with most MKs being dsRed$^+$ indicating that Actb^{dsRed} donor cells engrafted and differentiated into MKs in the recipient BM (Fig. 16D). In parallel to the engraftment of donor-derived MKs, the irradiation-induced vasodilation began to recede as indicated by an increasing intersinusoidal distance. However, even on day 14 after HSCT the intersinusoidal distance was still significantly decreased (Fig. 16E). These observations suggest that reconstitution of the BM after lethal TBI and subsequent transplantation starts already one week after treatment.

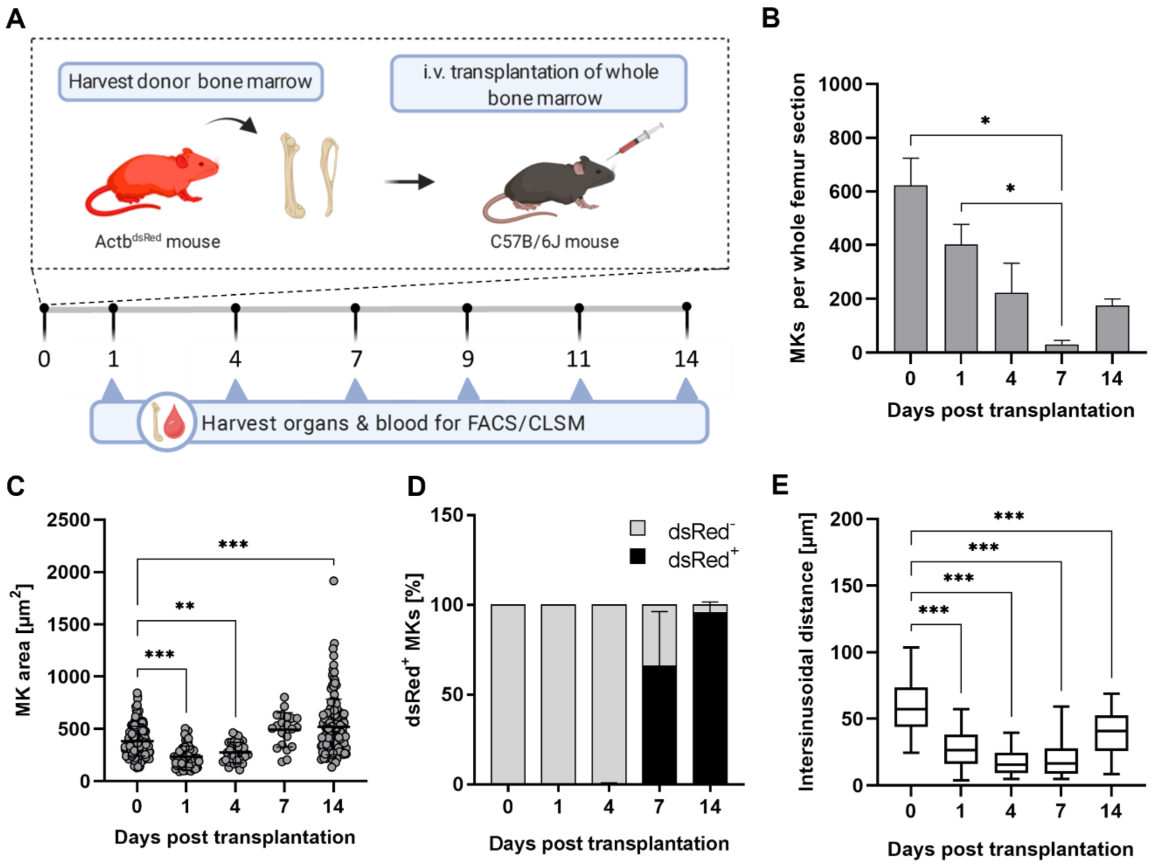

Figure 16. MK engraftment in a BM transplantation mouse model. (A) Experimental setup of BM transplantation with Actb^{dsRed} donor mice and wildtype recipients. Mice were sacrificed at the indicated time points (days) for organ extraction and subsequent femur cryosectioning with IF-staining of vessels and MKs. Stained femurs were then analyzed by CLSM. (B) The number of MKs and (C) MK size was determined in whole femur sections after transplantation. Values are mean ± SD. (D) Percentage of recipient- (dsRed$^-$) and donor-derived (dsRed$^+$) MKs after TBI. dsRed$^-$ and dsRed$^+$ MKs were counted in whole femurs scans. (E) Measurement of the vessel-to-vessel distance after transplantation. Box plot whiskers represent 5% resp. 95% percentile. (B-E) Quantitative analyses were performed using four whole femur scans from two transplantation experiments. (C,E) For measurement of the MK area and intersinusoidal distance ten visual fields (444 µm x 364 µm) were randomly selected from four whole femur scans. Asterisks mark statistically significant differences of the pairwise comparisons as indicated. (* $P < 0.05$; ** $P < 0.01$; *** $P < 0.001$). (A) was created using Biorender.

3.3.2. Donor cells engraft in clusters within the recipient bone marrow

One major advantage of the transplantation model used in this study is the ubiquitous, intrinsic dsRed reporter fluorescence from the donor-mice used for transplantation. This allows tracing of all donor cells regardless of their cell type, but at the same time tracking of BM cell subpopulations by specific antibody staining. The dynamics of HSC homing and engraftment have been described in previous reports using flow cytometry or various microscopy techniques, as reviewed in [94]. However, there are several limitations to these studies: (1) most reports focus on defined HSC populations, such as $Lin^{-}Sca\text{-}1^{+}c\text{-}Kit^{+}\ CD150^{+}CD48^{-}CD41^{-}$ cells, and overlook MKs or megakaryocytic progenitors; (2) homing and engraftment of donor(-derived) cells were either studied in whole organs or even the whole body and not on a single cells level; (3) previous reports lack a detailed mapping of the recovering BM during the first weeks after HSCT. We thus subjected our murine BM transplantation model to multicolor immunofluorescence microscopy in order to visualize $dsRed^{+}$ donor cells as well as MKs and sinusoids in the transplanted BM during the first two weeks after BM transplantation.

One day after transplantation very few isolated $dsRed^{+}$ cells were detectable in the recipient BM (Fig. 17, d1). By day four donor-derived cells became visible in microclusters (Fig.17, d4 white arrowheads), which increased significantly in their size and developed into large conglomerates until day 14 after transplantation (Fig. 17, d7, d14). These large clusters could be predominantly found near the BM cortex of the diaphysis (Fig. 17, d7, d14 white arrowheads) and the trabecular bone of the epiphyses (data not shown). Interestingly, not only donor cells in general displayed this clustered engraftment pattern, but also $GPIX^{+}$ MKs. In the native BM MKs are homogeneously distributed and most MKs are eradicated during TBI. Newly formed, donor-derived MKs then repopulate the BM in clusters (Fig. 17, d14 dashed lines), arguing that few stem or progenitor cells home and proliferate at distinct sites in the recipient BM and differentiate there into MKs.

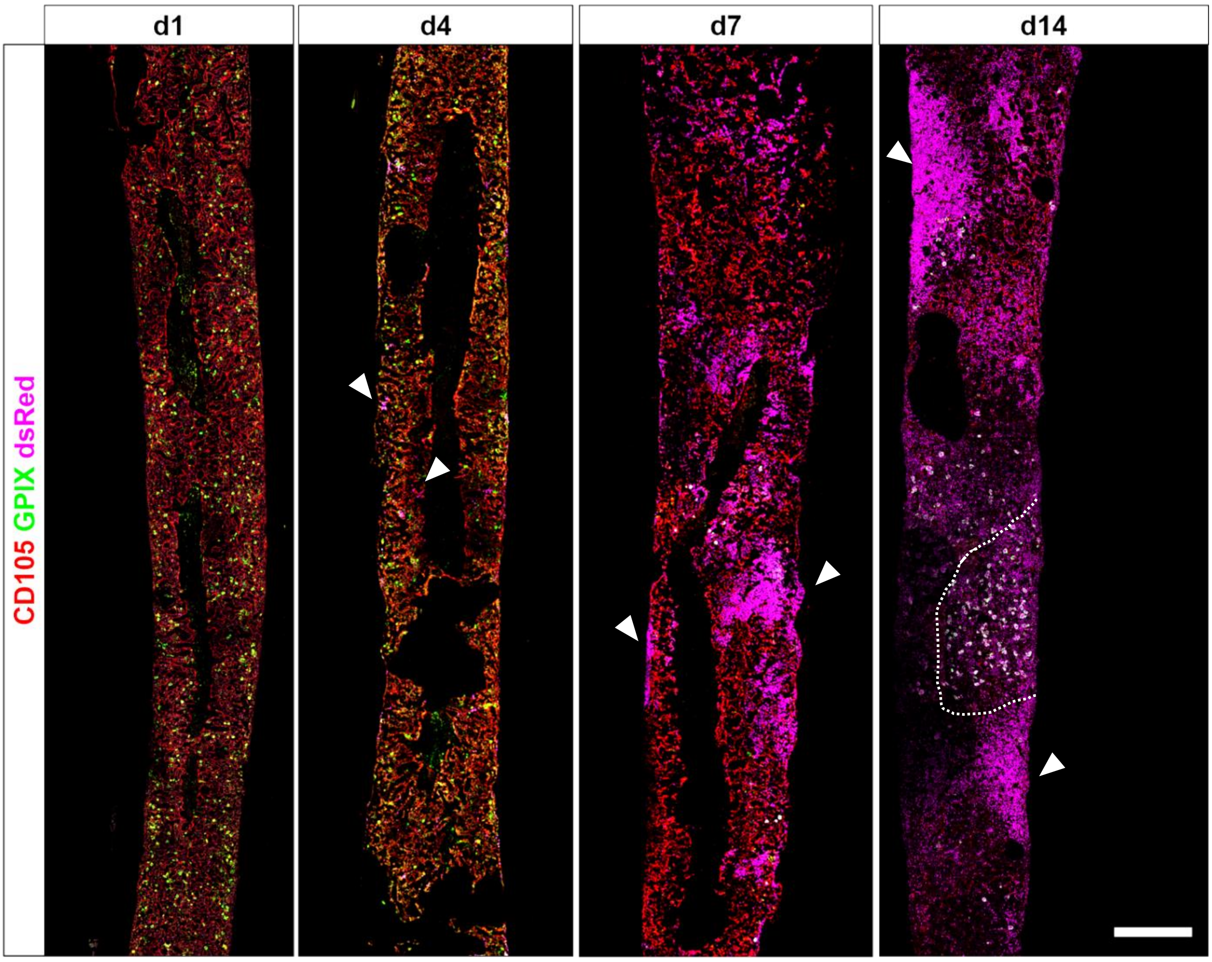

Figure 17. Engraftment of dsRed⁺ BM-donor cells. Representative immunofluorescence images of the recipient BM show dsRed⁺ (dsRed) cell cluster formation on day one (d1), four (d4), seven (d7) and 14 (d14) after transplantation. Sinusoids (CD105) are depicted in red, MKs (GPIX) in green. White arrowheads marks clusters near the bone cortex. The dashed line outlines a MK cluster (d14). Scale bar represents 500 µm. Images from one representative - out of three experiments - are depicted.

The observed engraftment pattern of dsRed⁺ donor cells (appearing as cortex-associated flattened triangles) compared to the MK engraftment pattern was not restricted to the BM in long bones but was also found in the sternum (Fig. 18A), which suggests that this engraftment pattern applies to all BM compartments. We next investigated whether this cluster formation occurred in other organs than bones. As liver and spleen act as blood filters, it is likely that intravenously injected BM cells reach and colonize these organs. In mice the spleen acts as a hematopoietic organ including megakaryocytes. On day 14 after transplantation sporadic dsRed⁺ cells were detectable in the liver (Fig. 18B), while a substantial amount of donor cells homed to the spleen, giving rise to dsRed⁺ MKs (Fig. 18C). On day seven after BM transplantation few individual MKs in the spleen were dsRed-positive (data not shown), while on day 14 after transplantation dsRed⁺ cells in the spleen seem to accumulate in the white pulp, but do not display a distinct cluster formation as was observed in the BM. Taken together these findings imply that the engraftment of donor cells in large clusters appears to be a BM-specific phenomenon.

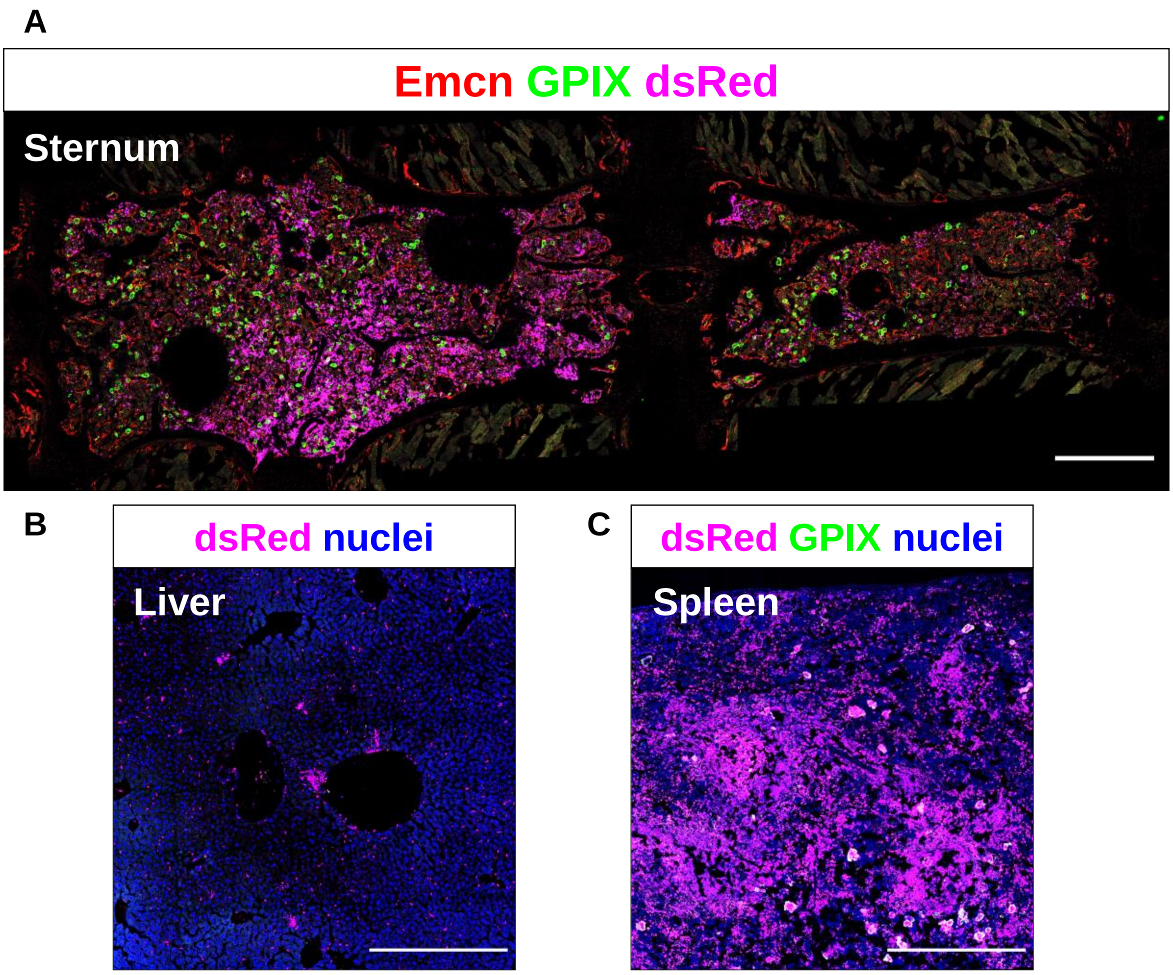

Figure 18. Cluster formation of donor cells is restricted to the BM. (A) dsRed$^+$ donor cells (magenta) cluster in the sternal BM but not in the liver (B) or spleen (C). MKs are shown in green (GPIX), and sinusoids are depicted in red (Emcn). Nuclei were stained with DAPI (blue). Scale bars represent 500 µm.

3.3.3. The different BM lineages do not exhibit the same engraftment pattern

The HSCT procedure involves intravenous graft infusion into the recipient (for mice as well as for humans). HSCs then find their way back from the circulation into the BM where they engraft and ideally reconstitute the ablated BM. Since the BM is highly vascularized even after radiation injury of the BM sinusoids, we expected transplanted HSCs to encounter multiple entry sites in the recipient BM, which would eventually result in an overall homogeneous distribution of donor-derived hematopoietic cells and their derived clusters. However, donor cells as well as MKs in the recipient BM engrafted in large clusters after transplantation (Fig. 17). As it is unclear whether this observation is also true for other hematopoietic cell lineages, we next aimed to analyze the clusters in respect to their cellular composition to clarify whether they consist of only one or a mixture of different cell populations. In order to address this, femurs from transplanted wildtype mice were used for cryosectioning and IF-staining against relevant lineage markers: GPIX as a MK marker, Ly6G to visualize granulocytes, Ly6C for monocytic cells, B220 as a pan B cell marker and Ter119 for erythrocytes as well as erythroid progenitors.

The staining revealed that MKs clustered near the BM cortex and were unexpectedly not located within the large dsRed$^+$ clusters although they were dsRed-positive as well (Fig. 19A). In contrast to MKs, Ly6G$^+$ did differentiate within the donor cell-derived clusters, as depicted by the overlapping dsRed$^+$Ly6G$^+$ staining shown in Fig. 19B (white areas). This overlap was to a much lower extent also detectable for Ly6C$^+$ cells (Fig. 19C), while it was completely absent for B cells (Fig. 19D) and for (Fig. 19E) erythrocytes. The latter cell type exhibited a homogeneous distribution within the transplanted BM. In conclusion, these results illustrate that at least MKs and Ly6G$^+$ cells home within the recipient BM in clusters, but that this cluster formation does not seem to be the general engraftment pattern found for all BM lineages.

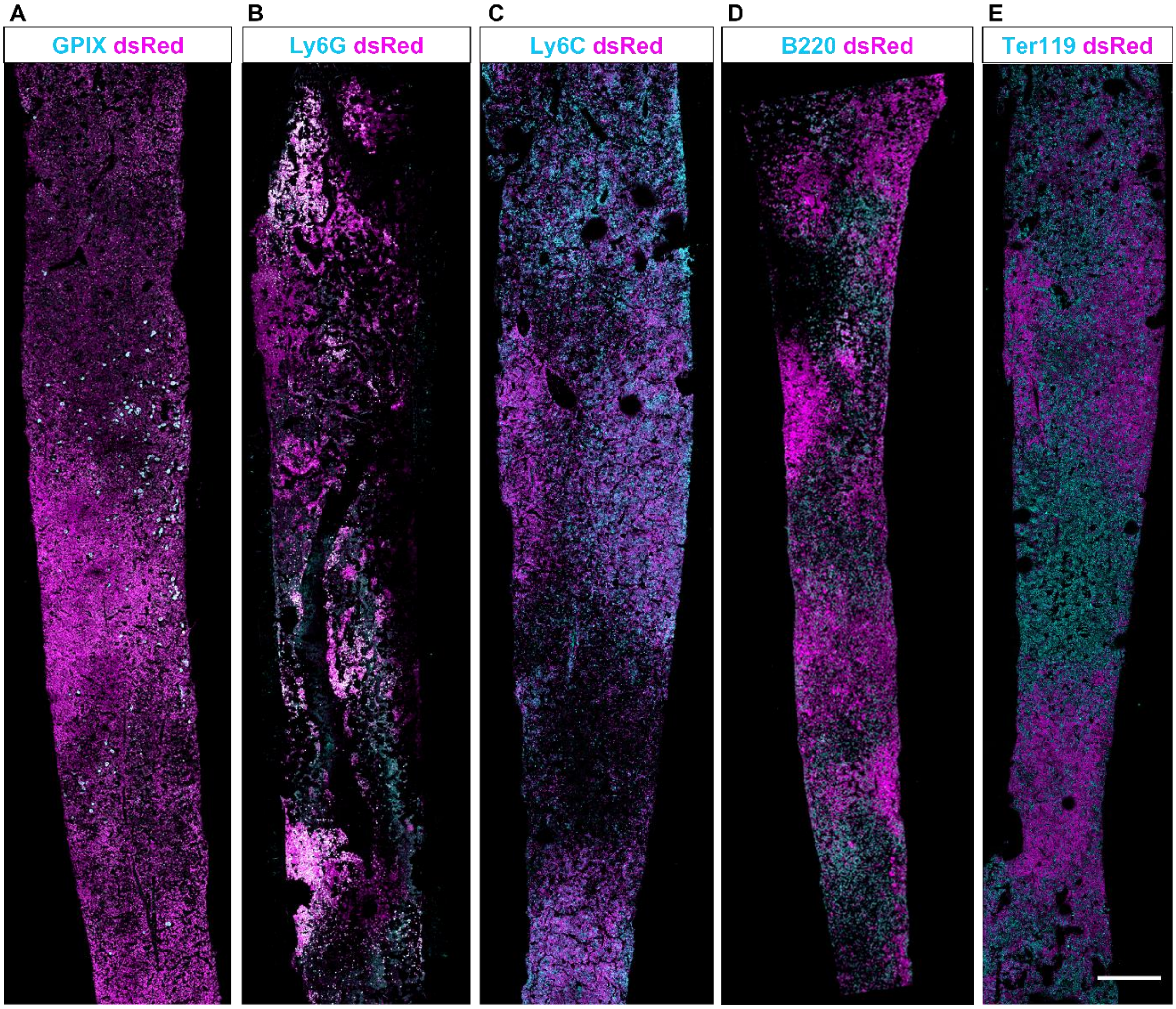

Figure 19. Engraftment of BM lineages. (A) MKs (GPIX), (B) granulocytes (Ly6G) engrafted in clusters. (C) The detection of Ly6C$^+$ cells partially overlapped with dsRed$^+$ (dsRed) cells while (D) B cells (B220) and (E) Ter119$^+$ cells are evenly distributed throughout the BM and showed no relevant co-staining for dsRed. Panels A, C, D and E show day 14, panel B day seven after transplantation. Scale bar represents 500 µm.

3.3.4. MMP9 expression in the BM niche does not play a role for cluster formation

MMP9 is known to be important for BM engraftment after low dose (2 Gy) irradiation by mediating VEGF release from mast cells and by shedding of SCF as well as recruitment of c-kit$^+$ stem and progenitor cells [95, 96], thereby promoting BM recovery and revascularization. This finding is in line with our observation that MMP9-deficient mice still display a pronounced vasodilation one week after sublethal TBI. However, it is not known whether MMPs or specifically MMP9 play a role for the localization of donor cells in the recipient BM.

In order to address this question, MMP9$^{+/+}$ and MMP$^{-/-}$ mice were used as recipients for transplantation with Actb^{dsRed} mice as BM donors. Femur cryosectioning and subsequent IF-staining for CLSM revealed the expected dsRed$^+$ cluster formation in MMP9 wildtype as well as in MMP9-deficient mice, indicating that MMP9 was dispensable for donor cell cluster formation (Fig. 20A). MK count and size was similar between wildtype and knockout animals (Fig. 20B,C), although the number of MKs in MMP9$^{-/-}$ mice dropped already four days after HSCT (112.5 ± 9.2 MKs per whole femur scan in knockouts compared to 316.5 ± 34.6 on the same day in MMP9$^{+/+}$ mice).

The percentage of dsRed$^+$ MKs was elevated on day four after transplantation in MMP9$^{-/-}$ mice (Fig. 20D,E) compared to wildtype control animals. MMP9$^{-/-}$ mice displayed a prolonged vasodilation on day seven after HSCT, which is indicated by a significantly decreased intersinusoidal distance, and which recaps our observations after sublethal TBI presented in Fig. 14. However, by day 14 after HSCT the intersinusoidal distance was comparable between MMP9$^{+/+}$ and MMP9$^{-/-}$ mice (Fig. 20F). These observations imply that MK engraftment and reconstitution of the vascularity was not dependent on the expression of MMP9 in the BM stroma.

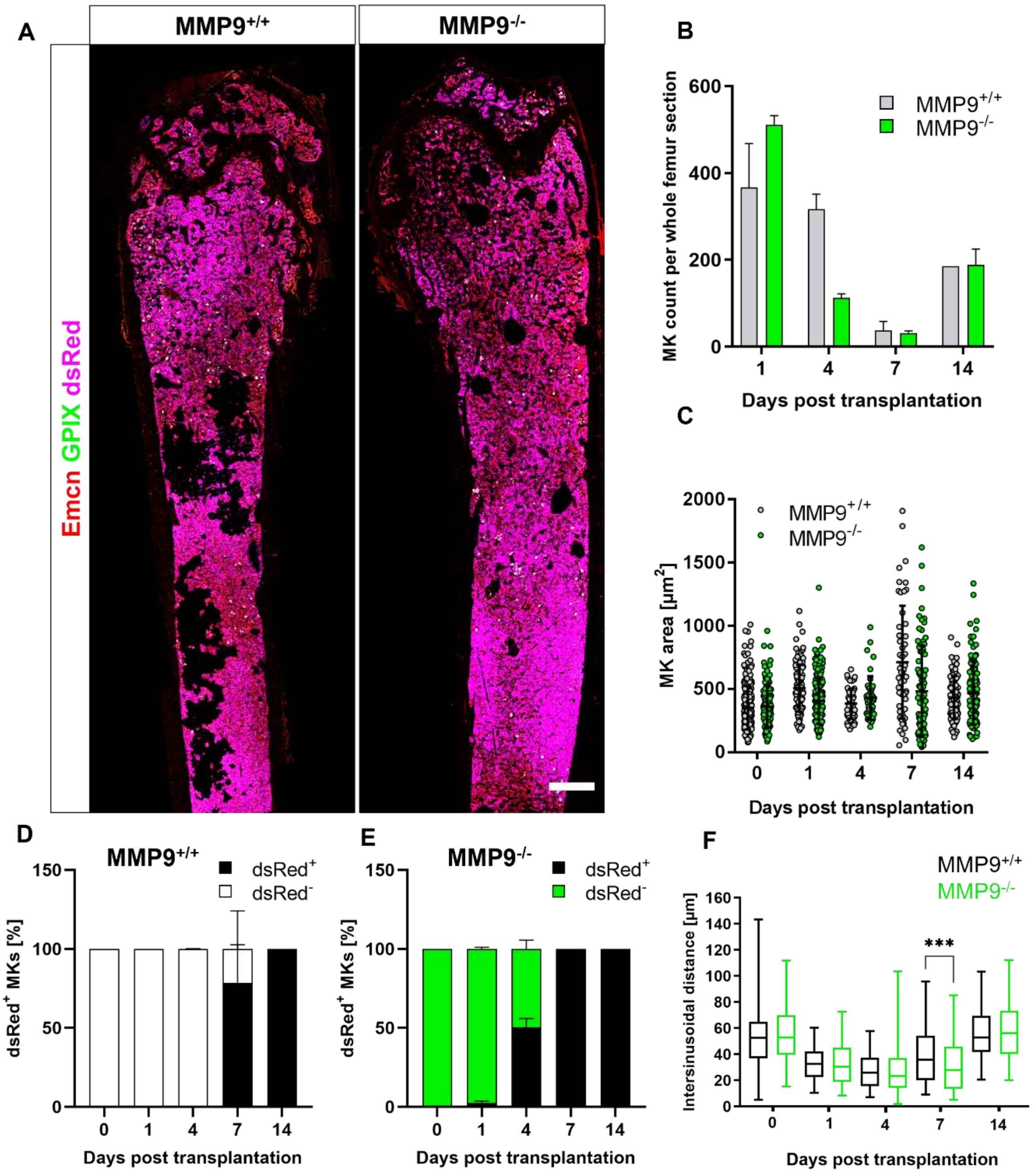

Figure 20. The role of MMP9 for dsRed cluster formation and MK engraftment. (A) IF-stained femur sections from MMP9$^{+/+}$ and MMP9$^{-/-}$ mice shows dsRed^{+} (magenta) cell cluster formation on day 14 after transplantation. MKs are shown in green (GPIX), vessels are depicted in red (Emcn). (B) Determination of the MK count in two whole femur scans per time point and genotype. Data is presented as mean ± SD. (C) For measurement of MK area ten visual fields (444 µm x 364 µm) were randomly selected from two whole femur scans per time point and genotype. Values are mean ± SD. (D) Percentage of dsRed^{+} MKs of total MK count in MMP9$^{+/+}$ and (E) MMP9$^{-/-}$ mice. (F) Measurement of the intersinusoidal distance after transplantation. The vessel-to-vessel distance was determined by random selection of ten visual fields (444 µm x 364 µm) from two whole femur scans per time point and genotype. Box plot whiskers represent 5% resp. 95% percentile. Asterisks mark statistically significant differences of the pairwise comparison as indicated. (*** $P < 0.001$).

The members of the MMP protein family have redundant substrates and can compensate the loss of another MMP to some degree, as was demonstrated by the generation of

MMP13/MMP9 or MMP2/MMP14 double knockout mice [14, 97]. A possible explanation for the seeming dispensability of MMP9 in the transplantation experiments shown in our study could therefore be the compensatory activity of another MMP. We thus analyzed the overall MMP activity in whole BM lysates from MMP9$^{+/+}$ and MMP9$^{-/-}$ mice after transplantation by gelatin-zymography (Fig. 21).

MMP9 activity in wildtype BM lysates was increased after transplantation. This was in line with the activity increase after TBI only (Fig. 11C). Importantly, increased total MMP activity was also detected in MMP9$^{-/-}$ lysates on day seven after transplantation, arguing that this is due to enzymatic compensation by one or more other MMP.

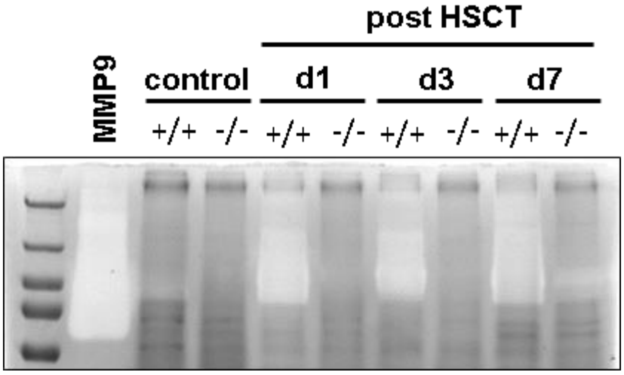

Figure 21. MMP activity after BM transplantation. Whole BM lysates from transplanted MMP9 wildtype and MMP9 knockout mice were subjected to analysis by gelatin-zymography. One out of three representative experiments is depicted.

3.3.5. Loss of MMP9 is compensated by upregulation of other MMPs

By using various complementary zymography techniques we could so far demonstrate that after TBI the gelatinolytic activity of MMP9 is upregulated in wildtype mice but remains virtually absent in MMP9$^{-/-}$ mice. After HSCT, MMP activity was attenuated in MMP9-deficient mice, albeit not completely abolished. We hence analyzed the transplanted MMP9$^{+/+}$ and MMP9$^{-/-}$ BM with regard to an increased RNA expression of possible compensatory MMPs. We thus performed qPCR analysis of four MMP mRNA transcripts reported to be expressed in the BM or that share common substrates with MMP2 and MMP9, namely (a) MMP14, (b) MMP13, (c) MMP19, and (d) MMP8.

The expression level was determined using the ΔΔCt-method with *Gapdh* as a loading control. The *Mmp9* mRNA expression level in transplanted MMP9$^{-/-}$ mice was found to be much below the level found in transplanted wildtype mice, suggesting that although wildtype BM was used for transplantation, the loss of MMP9 is not substituted for by the donor-BM. On day one after transplantation, *Mmp9* expression in wildtype mice was comparable to that in non-irradiated (d0) controls (Fig. 22A). On day three after transplantation, expression levels in wildtype animals decreased drastically ($2^{-\Delta\Delta Ct}$ of 0.3 ± 0.08) and increased again to levels up to $2^{-\Delta\Delta Ct}$ of

0.6 ± 0.16 on day seven. This mRNA expression level directly corresponds to the detected protein expression and activity of MMP9 after sublethal TBI without subsequent HSCT which was presented in section 3.2.2. (Fig. 11). MMP2 protein activity was not detectable in BM derived from mice with TBI only or TBI with subsequent transplantation, but we found that *Mmp2* mRNA expression was massively upregulated in both MMP9$^{+/+}$ and MMP9$^{-/-}$ mice (Fig. 22B), implying that the *Mmp2* transcript is either not translated into a protein or that the MMP2 zymogen is not activated in the transplanted BM.

MMP14 has been reported to play a role comparable to functions attributed to MMP2. Both MMP9$^{+/+}$ and MMP9$^{-/-}$ mice showed an increasing *Mmp14* expression after transplantation, which was inverse to MMP2 levels (Fig 22C). A similar increase was found for *Mmp13* (Fig. 22D). MMP14 or MMP13 were not upregulated in MMP9$^{-/-}$ mice, suggesting that even though they are known to show functional redundancy for the two main gelatinases MMP2 and MMP9, they are probably not compensating for the loss of MMP9. In contrast to the other candidate MMPs tested here, we detected a MMP9$^{-/-}$-specific two-fold increase (compared to wildtype values) of the collagenases *Mmp19* on day three (Fig. 22E) and *Mmp8* on day seven after transplantation (Fig. 22F), making the latter two MMPs likely candidates to compensate for MMP activity in *Mmp9*-null mice.

Taken together, we could demonstrate that residual MMP activity is detectable in mice receiving BM of MMP9$^{-/-}$ donor mice. This is probably due to a compensatory (upregulated) enzyme activity by other MMPs such as MMP8 or MMP19. This upregulation of MMPs with a comparable set of substrates might explain why MMP9 expression is apparently dispensable for donor cell and MK engraftment after transplantation.

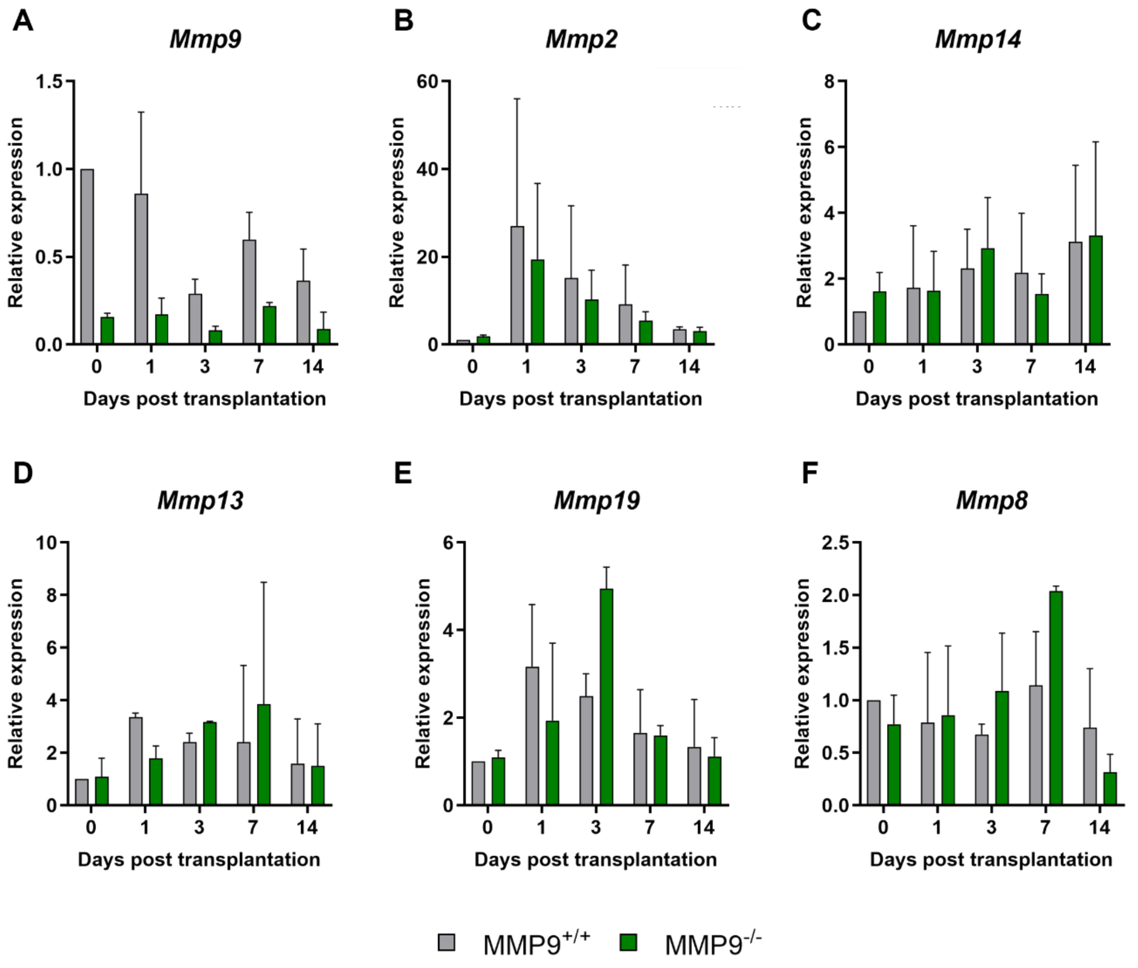

Figure 22. MMP expression in MMP9$^{+/+}$ and MMP9$^{-/-}$ mice after transplantation. MMP9$^{+/+}$ and MMP9$^{-/-}$ were subjected to TBI with BM transplantation and sacrificed for BM extraction. Whole BM was then used to isolate RNA and generate cDNA to analyze expression of (A) *Mmp9*, (B) *Mmp2*, (C) *Mmp14*, (D) *Mmp13,* (E) *Mmp19* and (F) *Mmp8* by qPCR. MMP expression was normalized to the endogenous control *Gapdh*. Data of two experiments (n=2), each determined in triplicates, were averaged. Values are mean ± SD.

3.3.6. Heterogeneous chemokine expression after transplantation

Cytokines and chemokines (or chemotactic cytokines) are small signaling proteins (many around 8 to 20 kDa) that are modulators of cell proliferation, differentiation, and migration [50]. Constitutively expressed chemokines at distinct sites within the BM play an important role for cell homeostasis by directing cells to specific locations e.g., recruitment of HSCs to the vascular stem cell niche by CXCL12. HSC proliferation and differentiation is strictly regulated by the interplay of a distinct set of chemokines binding to their respective receptors, such as CXCL12 (from CAR cells at the sinusoidal vessels) binding to CXCR4 present on HSCs (and MKs).

In order to identify cytokines and chemokines that may be important during BM transplantation we chose a largely unbiased explorative approach and analyzed the blood serum level of relevant cytokines and chemokines in a multiplex-based immunoassay (ProcartaPlex). This method allows to determine the expression levels of 18 analytes per sample simultaneously (Table 19). As by this approach not all relevant chemokines and cytokines could be measured in the same sample, we decided to expand our portfolio by TPO, CXCL12 and SCF, whose serum levels were measured by ELISA. We selected up to six time points after BM transplantation (d1, 4, 7, 9, 11, 14) in addition to untreated mice (d0). We found that 13 out of the 21 tested analytes displayed a measurable, significant increase compared to untreated controls (Table 19, blue), while eight were either expressed below or slightly above the detection limit (Table 19, red).

Table 19. Chemokine multiplex panel

Analyte						
G-CSF	CXCL5	CCL7	TGF-β	SCF	CCL5	CXCL2
CXCL9	CCL11	VEGF-A	TPO	M-CSF	TNF α	Leptin
CXCL1	CCL2	Adiponectin	CXCL12	GM-CSF	CCL3	CCL4

Previous studies have shown that TPO and G-CSF plasma levels increase in response to low platelet or neutrophil counts, respectively [98, 99]. We therefore expected to find elevated serum levels for both cytokines in response to HSCT-induced thrombocytopenia and neutropenia. Platelet counts dropped massively on day seven and nine post HSCT, while TPO serum levels increased and peaked on day nine (Fig. 23A).

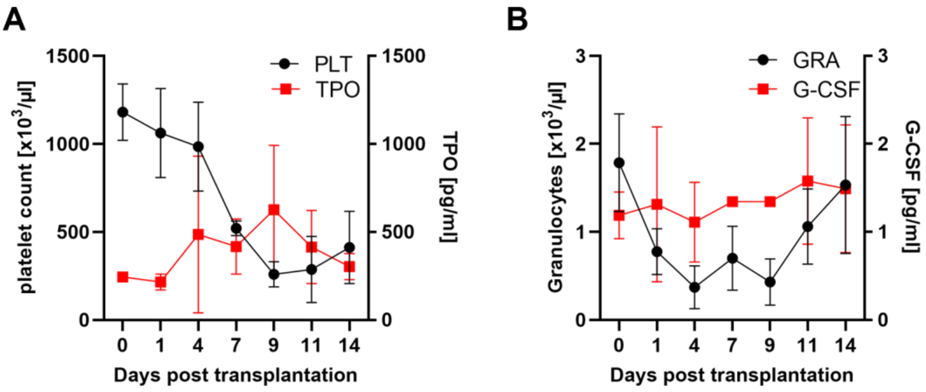

Figure 23. Correlation of peripheral blood cell counts with chemokine expression. (A) TPO levels were measured by ELISA in transplanted and untreated control (day zero) wildtype mice. (B) G-CSF protein expression was assessed by ProcartaPlex immunoassay. Data is presented as mean ± SD. n=3

The neutrophil counts dropped already on day one after HSCT and reached the nadir on day four, whereas G-CSF serum levels inclined steadily from day one on for 14 days during the detection period (Fig. 23B). These two hematopoietic growth factors thus increased in response to the lack of peripheral cells. This reciprocal relation of peripheral blood count and subsequent cytokine upregulation demonstrates sufficient sensitivity and specificity to validate our experimental approach. We found that expression levels of CXCL1 were selectively upregulated from 1 pg/ml in untreated animals to 12 pg/ml on day four after HSCT (Fig. 24A). CXCL9 levels, in contrast, were transiently upregulated from 5 pg/ml in untreated animals to 36 pg/ml on day nine and 34 pg/ml on eleven after HSCT (Fig. 24B). CXCL5 levels were found to be around 113 pg/ml in untreated animals and serum levels were gradually declining, reaching the nadir of 18 pg/ml on day nine after transplantation and then began to increase again up to 50 pg/ml on day 14 (Fig. 24C). Interestingly, this corresponds to the dropping platelet count after HSCT that also started to recover after day nine (Fig. 23A). CXCL5 was shown to be expressed by platelet-derived growth factor B-activated fibroblasts to promote BM mesenchymal stem cell chemotaxis and differentiation [100]. This hints towards a possible interplay of platelets and CXCL5. Compared to untreated control levels (day zero) expression of the CCL chemokines CCL2, CCL7 and CCL11 was sustainably upregulated from day one after HSCT until the analysis endpoint on day 14 (Fig. 24D-F).

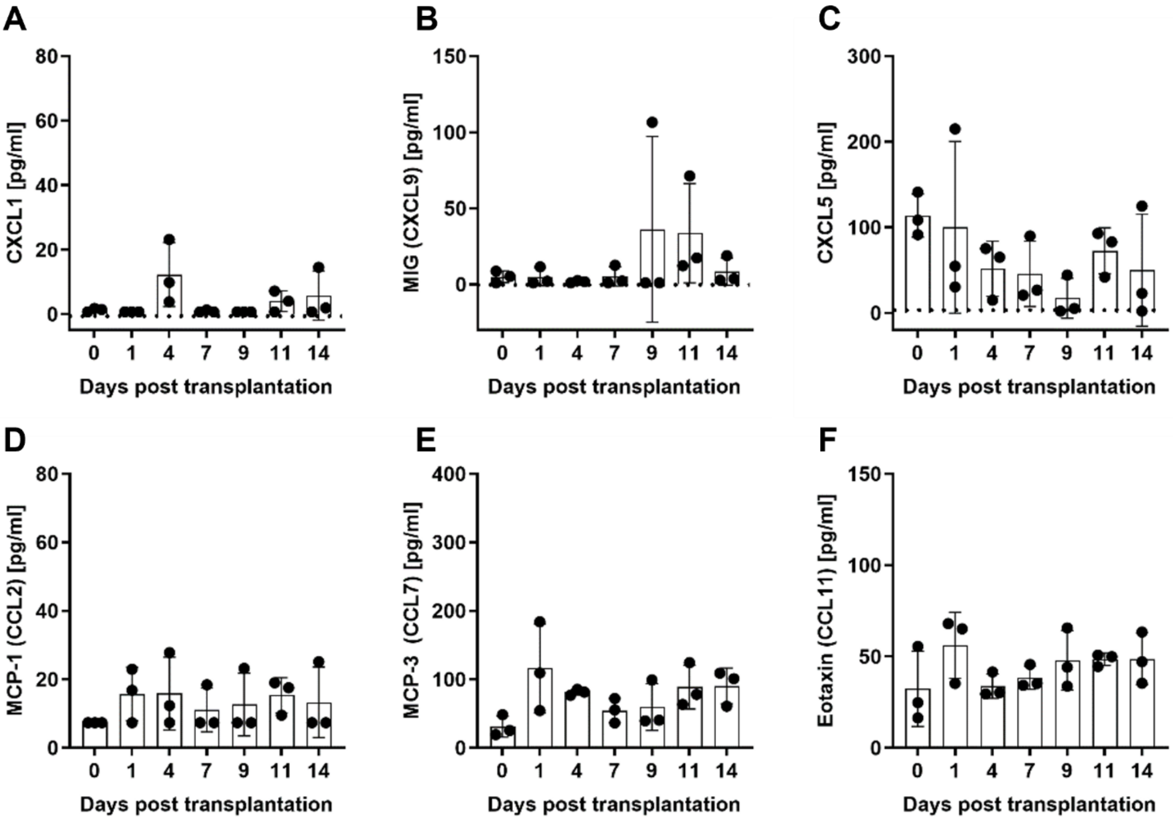

Figure 24. CXC and CCL chemokine expression after HSCT. (A) CXCL1 expression peaked on day one after HSCT and was still increased on day eleven and 14. (B) CXCL9 expression was elevated on day nine and eleven post HSCT. (C) Transient reduction of CXCL5 expression until day nine after HSCT. (D) Slightly increased expression of CCL2. (E) CCL7 levels were upregulated as of day one after treatment. (F) Upregulation of CCL11 persists until the endpoint of analysis on day 14 post HSCT. Data is presented as mean ± SD. n=3

Adiponectin was overall highly expressed (91 ng/ml) and only marginally altered within 14 days after HSCT (Fig. 25A). A similar expression pattern was visible for SCF (218 pg/ml on day zero and 248 pg/ml on day 14 after HSCT, Fig. 25B). CXCL12 levels started at 9 pg/ml and increased on day one (15 pg/ml), eleven and 14 after HSCT (Fig. 25C). Taken together, our data indicate that although SCF and CXCL12 are expressed by the same cell types, they are differentially regulated after TBI and HSCT. TGF-β serum levels are about 3026 pg/ml in untreated animals and were markedly reduced to 393 pg/ml already on day one after HSCT (Fig. 25D). Importantly, only the bioactive form of TGF-β is detected by the assay system used here. This cytokine is a known inducer of HSC quiescence in order to maintain the stem cell pool [101]. Studies with human and murine HSCs have demonstrated that neutralization of TGF-β leads to release of HSCs from dormancy [102, 103]. In regard to the expression pattern shown here, this finding suggests that downregulation of TGF-β after HSCT might be linked to induction of HSC proliferation in order to facilitate BM reconstitution. As already mentioned above, TPO and G-SCF expression increased after HSCT in correlation with the drop in peripheral white blood cell or the platelet counts, respectively (Fig. 25E,F).

In order to study the chemokine expression pattern during the acute phase after radiation injury, we have additionally performed the ProcartaPlex assay and ELISAS in mice that were either sublethally (5 Gy) or lethally (10 Gy) irradiated. This chemokine expression data after 5 Gy or 10 Gy TBI without subsequent HSCT is shown in section 6.1. (Fig. 35, 36) and confirms our data after HSCT. Taken together we identified CXCL1, CXCL9, and CXCL5 as chemokines expressed at selective time points after HSCT. Furthermore, we found TGF-β to be one of the few growth factors that were downregulated after HSCT. These observations imply that these chemokines are likely to have an impact on donor cell engraftment.

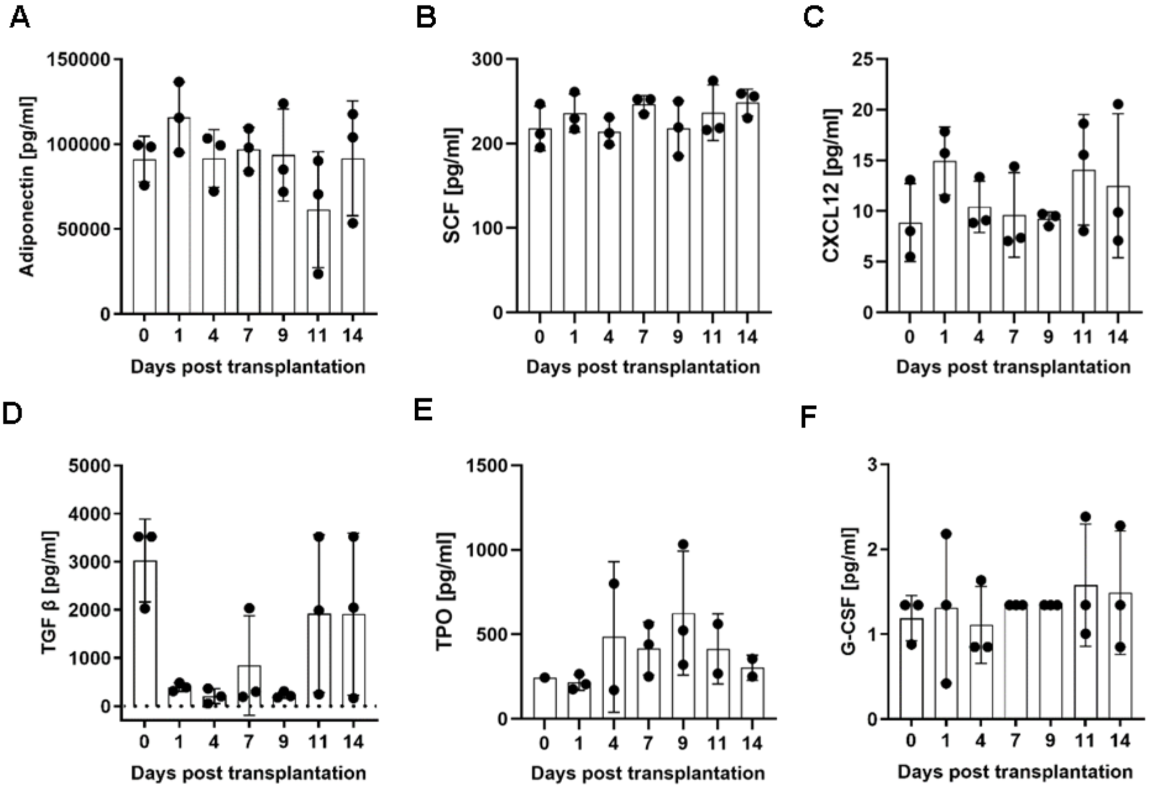

Figure 25. Cytokine expression after HSCT. Serum levels were determined using the ProCarta multiplex assay (A, D, F) or ELISA (B, C, E). (A) High expression of adiponectin and (B) SCF in both untreated control (day zero) and transplanted animals. (C) Transient upregulation of CXCL12 expression (D) Massive downregulation of TGF-β until day nine after HSCT. (E) Increasing TPO and (F) G-CSF serum levels. Data is shown as mean ± SD. n=3

The overall goal of the chemokine multiplex analysis was to identify chemokines that possibly influence BM reconstitution and cluster formation after HSCT. We therefore reanalyzed the expression data and chose to display the results as fold-change over control in radar plots, as this allows intuitive grasping of relevant molecules and of outliers. Highly expressed chemokines include CXCL1 with a 10-fold increase on day one and five-fold upregulation on day 14 (Fig. 26B,F). CCL7 showed a 3.7-fold increased expression on day one, 1.7-fold on day seven and three-fold on day eleven and 14 (Fig. 26A,C,F). Furthermore, seven-fold upregulation of CXCL9 on day nine and eleven is emphasized in the radar plots shown in Fig. 26D and E. In summary, we could detect peak expression of few individual chemokines after TBI and HSCT, such as CXCL1, CCL7 and CXCL9, which will be targets for further experiments.

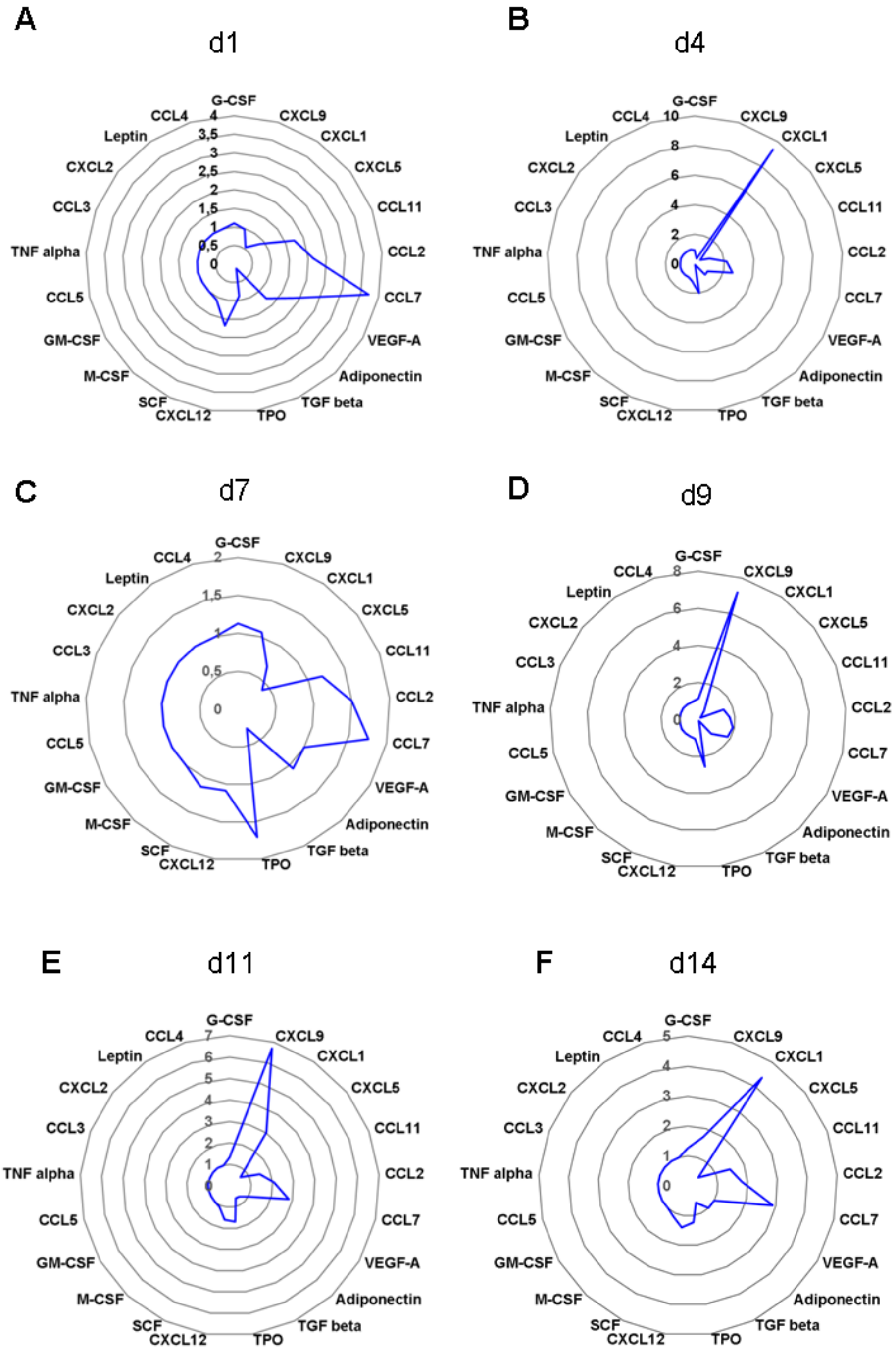

Figure 26. Radar plots displaying alterations in chemokine levels after HSCT. (A) Chemokine expression is displayed as fold-change over untreated control levels on day one (B) day four (C) day seven (D) day 9 (E) day eleven and (F) day 14 after lethal TBI and subsequent BM transplantation. Data is presented as fold-change over untreated control. n=3

3.4. Platelet biogenesis and function after BM transplantation

Apart from an increased risk of life-threatening infections due to low neutrophil counts after myeloablation for HSCT, prolonged and severe thrombocytopenia is another complication that affects approx. 20% to 30% of HSCT patients [92, 93]. Hemorrhage after HSCT can take various forms, with the most common life-threatening ones being pulmonary and gastrointestinal bleeding [104]. Although bleeding can be pharmacologically treated (e.g., antifibrinolytics) or by transfusions of platelet concentrates, the latter bears the risk of allo-immunization. HSCT is further associated with thromboembolic events such as venous thromboembolism (VTE), transplant-associated thrombotic microangiopathy (TA-TMA) or sinusoidal obstruction syndrome (SOS). While the contribution of the endothelium and the coagulation system to hemostatic and thrombotic HSCT complications have been previously assessed, the role of platelets has not yet been studied in detail. In the previous chapters we could provide experimental evidence that the BM undergoes massive remodeling after TBI and HSCT affecting the vascular MK niche by (a) degradation of ECM proteins (b) the rearrangement of pericytes surrounding BM sinusoids and (c) vasodilation (chapter 3.2.1). It is not clear whether (or to what degree) this aberrant vascular wall influences thrombopoiesis and finally platelet function. We therefore sought to study platelet function in our murine HSCT model.

3.4.1. Peripheral blood cells are rapidly cleared after myeloablation

Lethal TBI leads to the ablation of peripheral WBCs and platelets (Fig. 23). We used this effect to monitor irradiation treatment efficiency and later post-transplantation hematopoiesis by longitudinally follow the development of peripheral blood cell counts after BM transplantation. In humans, lymphocytes are the first cells to be eradicated after TBI due to their high susceptibility to irradiation. This massive loss of peripheral blood lymphocytes on day one after treatment could be reproduced in our HSCT mouse model (0.9 ± 1.1x10^3/µl one day after HSCT, Fig. 27A). The red blood cell (RBC) count was overall only marginally reduced (Fig. 27B), which is probably due to their low sensitivity to radiation as enucleated cells, as well as their long life span (120 days in humans, 40 days in mice). Furthermore, we measured a rapid decline of the white blood cell (WBC) count to 0.9 ± 0.6x10^3/µl during the first week after HSCT and recovery of the WBC count starting from day seven after transplantation (Fig. 27C). Platelet counts were also heavily reduced during the first days after HSCT to a nadir of 260 ± 72.1x10^3/µl and started to increase again after day nine (Fig. 27D). Concomitantly to the decrease in platelet counts, the mean platelet volume (MPV) began to increase (5.8 ± 0.1 fl on day zero vs. 6.4 ± 0.8 fl on day nine after HSCT, Fig. 27E), which underlines the inverse relation between platelet count and size, and which hints towards the triggering of platelet biogenesis. Importantly, monitoring of blood cell counts (including the platelet count) in human HSCT patients has shown that in most cases the WBC begins to recover before platelet counts start to increase [105]. We were able to observe a similar kinetic in our murine HSCT model, implying that BM engraftment and post transplantation hematopoiesis is similar in humans and mice and that our experimental mouse model provides a *bona fide* tool to study the development of blood cell lineages after HSCT.

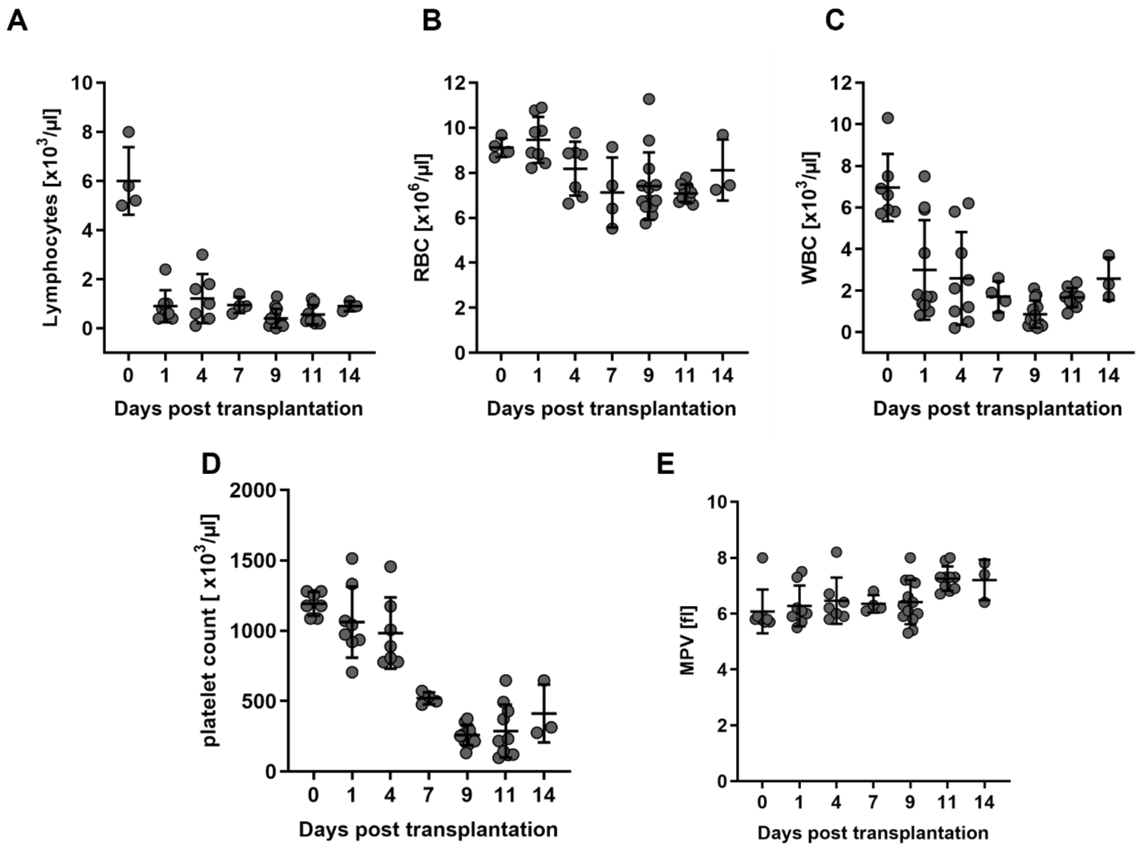

Figure 27. Blood cell parameters after BM transplantation. (A) Lymphocyte count, (B) the red blood cell (RBC) count, (C) white blood cell (WBC) count, (D) platelet count and (E) mean platelet volume (MPV) after HSCT. Blood cell parameters were measured with an automated hematology analyzer (ScilVet). Data is presented as mean ± SD. n = 4 to 8.

3.4.2. Heterogeneous platelet surface receptor expression after sublethal TBI

We have so far demonstrated that the MK BM microenvironment is heavily remodeled after sublethal TBI as well as after HSCT and that MK engraftment occurs at distinct sites in the recovering BM compared to precursor cells of other blood cell lineages (Fig. 19). It is yet not known how platelets are structurally and functionally influenced when they are generated at an aberrant vascular niche. We thus first studied the expression levels of platelet glycoproteins and integrins after 5Gy TBI without HSCT by flow cytometry, in order to study the effect of acute radiation injury on platelets.

Expression of the vWF receptor complex subunits GPIb and GPV was decreased to approx. 50% of untreated control levels (day zero) on day nine after TBI, while GPIX expression was reduced by 40% (Fig. 28A,B). The tetraspanin CD9 is an abundantly expressed transmembrane platelet surface receptor, which is considered to be a protein essential for organizing for the expression and distribution of the highly abundant fibrinogen receptor $\alpha_{IIb}\beta_3$. Expression of both receptors was found to be downregulated by half on day nine after TBI (Fig.

28B,C). The same decrease could be observed for the hemITAM receptor CLEC-2 (Fig. 28D). The abundance of the collagen receptor GPVI was also reduced to 50% of control expression level, while expression of the second major collagen receptor integrin $\alpha_2\beta_1$ was even reduced by 70% (Fig. 28C,D). In summary, surface abundance of all receptors was decreased around 50% after TBI although the downregulation severity varied between the different surface receptors.

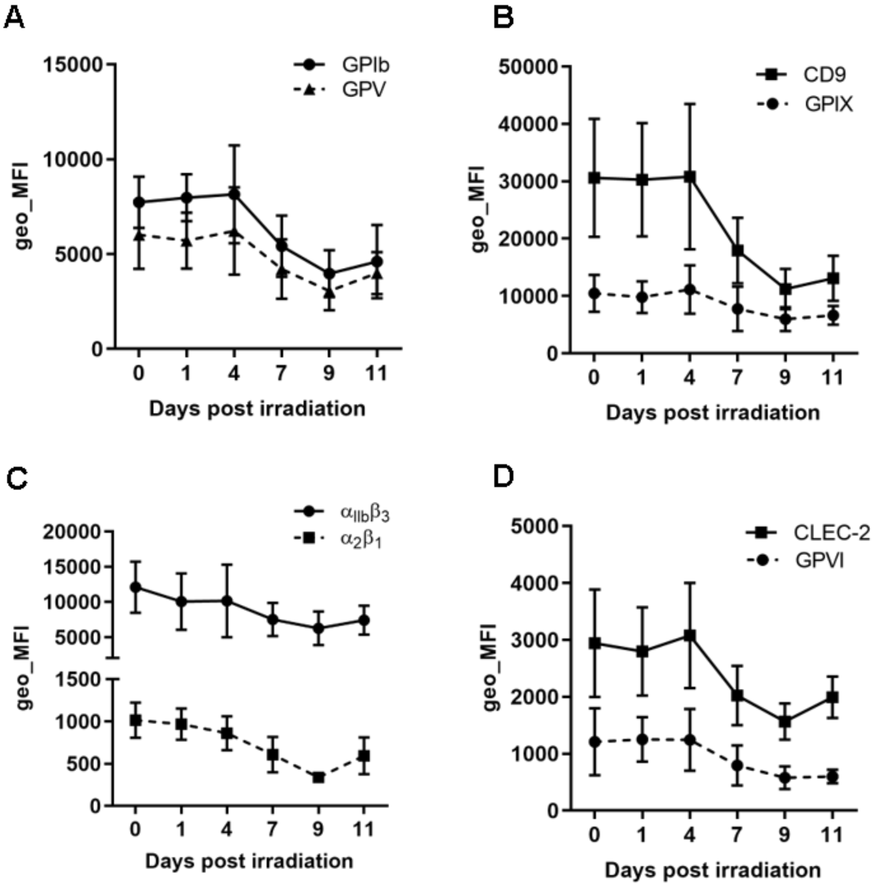

Figure 28. Platelet surface receptor expression after sublethal TBI. (A) Expression of GPIb, GPV, (B) GPIX, CD9, (C) integrin $\alpha_{IIb}\beta_3$, $\alpha_2\beta_1$, (D) CLEC-2 and GPVI was assessed by flow cytometry after sublethal TBI. The geo-MFI values are depicted as mean ± SD. n = 7 from two independent irradiation experiments.

3.4.3. Platelets become hyporeactive after 5Gy TBI

Alterations in the expression levels of platelet surface receptors may influence platelet function. Consequently, we assessed the release of platelet α-granules upon stimulation with various agonists after 5Gy TBI. For this, platelets were activated either with thrombin, collagen-related peptide (CRP-X_L) or convulxin. Neo-exposure of P-selectin (CD62P) was measured by binding of fluorescently labeled anti-CD62P antibody in a flow cytometric approach. The geometric MFI (geo MFI) determined for resting controls was then subtracted from the values measured for activated samples to obtain values for the delta geo MFIs.

Upon high dose (0.1 U/ml) stimulation of PAR3 and PAR4 with thrombin, CD62P exposure was overall unaltered on day one and day four after TBI and then gradually declined until day nine to 33% of the control values. Platelet activation after thrombin stimulation started to normalize again from day eleven after TBI (Fig. 29A). In contrast, after platelet activation by GPVI-stimulation with high concentrations of CRP-X_L (10 µg/ml) hardly any degranulation was detectable from day four after TBI (Fig. 29B). Importantly, platelet stimulation with convulxin, which acts as a strong agonist by induction of GPVI multimerization, could rescue this hyporeactive phenotype partly on day four after TBI, but did not induce activation at the other indicated time points (Fig. 29C). Taken together, our data shows that although expression of GPVI is only slightly reduced, platelet activation through stimulation of this receptor after TBI is massively disturbed.

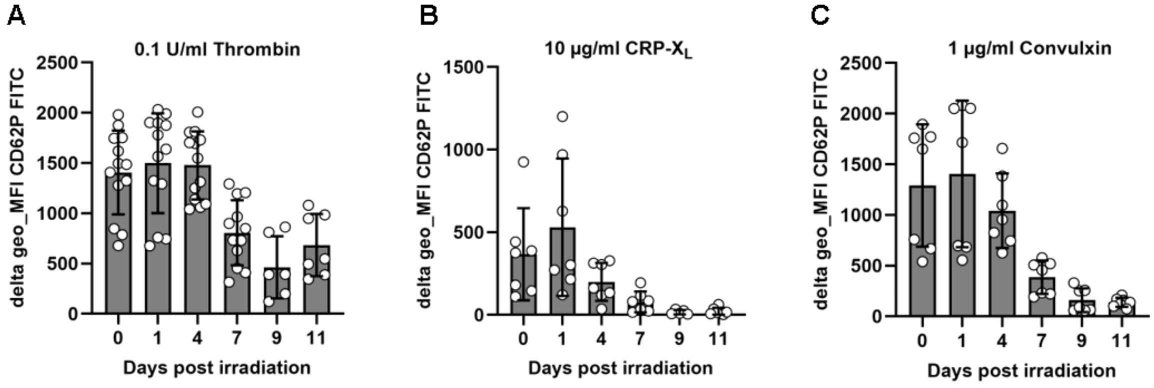

Figure 29. CD62P exposure of activated platelets after 5Gy TBI. (A) Platelet degranulation upon thrombin stimulation. (B) Activation of platelets with the GPVI agonist CRP-X_L and (C) convulxin. Data is displayed as mean ± SD. n = 6 to 13 from at least two independent irradiation experiments.

3.4.4. Platelet aggregate formation is impaired after TBI

Assessment of activated platelets by flow cytometry allows evaluating their capability to secrete granule contents and expose molecules that play a role during hemostasis on a single cell level. However, this type of analysis does not provide information about the ability of platelets to adhere to one another and form stable aggregates. In order to determine aggregate formation after TBI we next performed aggregometry analysis. For this, a suspension of washed platelets was stimulated under stirring conditions with thrombin, Horm collagen or CRP-X_L and then subjected to measurement of the transmitted light using a four-channel aggregometer. Importantly, platelet counts were adjusted to 500x10^3/µl in all samples.

Thrombin activation of control platelets led to rapid aggregate formation as indicated by the increasing light transmission. In contrast, only weak aggregation was detected for platelets after TBI (Fig. 30A). Stimulation of control platelets either with Horm collagen or CRP-X_L induced stable aggregation, while aggregate formation was completely absent for platelets after irradiation (Fig. 30B,C). This data confirms the GPVI activation defect shown by flow cytometry. Furthermore, it demonstrates that platelet function is impaired on multiple levels and that this functional defect is not only due to TBI-induced thrombocytopenia.

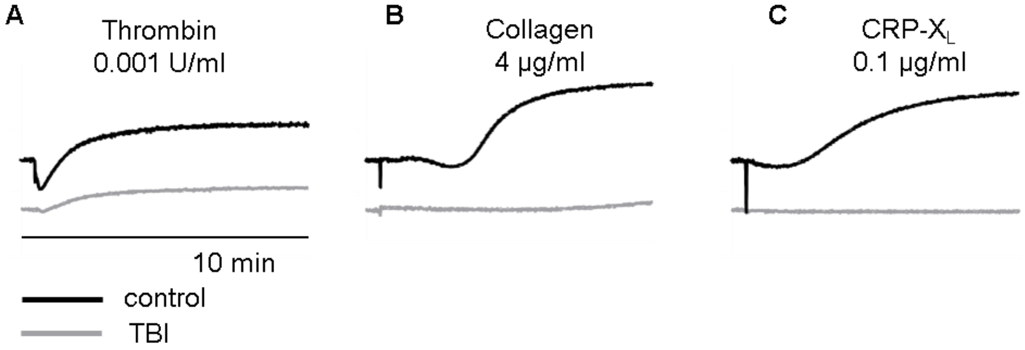

Figure 30. Light transmission aggregometry of platelets after TBI. (A) Platelet stimulation of control platelets (black) and platelets from sublethally irradiated mice (grey) with (A) thrombin (B) Horm collagen or (C) CRP-X$_L$. n = 4 untreated controls vs. 8 irradiated mice (d9 after TBI) pooled to 2 samples. Platelet count was adjusted to 500.000/µl in all samples.

3.4.5. GPVI downstream signaling is disturbed after TBI

Platelets from irradiated mice displayed a major hyporeactivity towards the GPVI agonists CRP-X$_L$ and convulxin, although expression of the receptor itself was only marginally altered, hinting towards a defect in the signaling cascade of GPVI. We therefore analyzed phosphorylation of the key downstream signaling protein Syk at tyrosine 525/26 in platelets after sublethal TBI by quantitative immunoblotting.

Washed platelets from control and irradiated mice were stimulated with CRP-X$_L$ under stirring conditions and lysed 60 seconds after activation. Syk was not phosphorylated in resting platelets, confirming no pre-activation. Upon stimulation with CRP-X$_L$ p-Syk became detectable in platelets from non-irradiated controls and to a lower degree also in platelets from irradiated mice (Fig. 31A). While quantification of total Syk protein levels revealed no difference between non-irradiated and irradiated samples (Fig. 31B), p-Syk levels were found to be significantly reduced in platelets after TBI (Fig. 31C,D). These observations suggest that the GPVI downstream signaling cascade is compromised after TBI. This is in line with the hyporeactive phenotype that platelets from irradiated mice exhibited in our flow cytometry and aggregometry experiments.

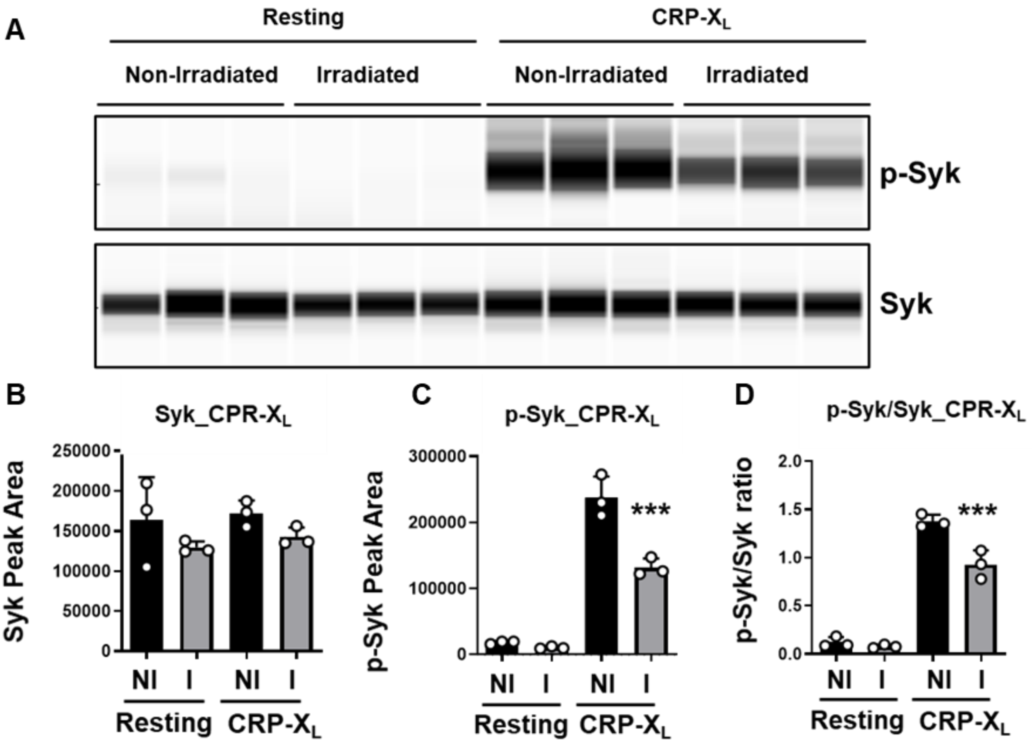

Figure 31. Syk phosphorylation after HSCT. (A) Platelets (adjusted cell count to 500x10^3/µl) from non-irradiated control and 5Gy irradiated mice (d9 post TBI) were stimulated with 30 µg/ml CRP-X$_L$ for 60 seconds under stirring conditions before lysis. Semi-quantitative immunoblotting revealed reduced Syk phosphorylation after sublethal TBI. (B-C) Determination of the p-Syk ratio between control and irradiated platelets as well as p-Syk to total Syk after TBI. (D) Total Syk expression is not significantly altered after TBI. n = 3 control vs. 9 irradiated mice pooled to 3 samples. (B-C) Data is presented as mean ± SD. Asterisks mark statistically significant differences between non-irradiated (NI) and irradiated (I) samples. (*** $P < 0.001$). Data was generated in cooperation with Dr. Zoltan Nagy.

3.4.6. Platelets are dysfunctional after BM transplantation

Myeloablative TBI in a clinical setting is always combined with transplantation of healthy HSCs for reconstitution. We have demonstrated that MK repopulation in the recipient BM is detectable already one week after HSCT (Fig. 16). Thus, we next studied platelet function in our murine HSCT model in order to assess not only surface receptor expression and platelet function after acute radiation injury only, but also during recovery of the BM MK pool, which reflects the situation in humans after HSCT.

Expression of the vWF receptor subunits GPIb, GPV and GPIX was overall decreased by half until day nine after transplantation, which corresponds to the platelet count nadir and increased again from day eleven after HSCT (Fig. 32A,B). CD9 and integrin $\alpha_{IIb}\beta_3$ was transiently increased and then downregulated to 40% and 60% of control expression by day nine after HSCT (Fig. 32B,C). The hemITAM receptor CLEC-2 was similarly downregulated (Fig. 32D). While the abundance of the collagen receptor $\alpha_2\beta_1$ was virtually unaltered until day 11 and then downregulated by 60% on day 14, GPVI expression was reduced by approx. 50% (Fig. 32C,D). Compared to the surface receptor levels in the cohort of mice "after TBI only" (Fig. 28), we found an overall milder but similar decrease of glycoprotein and integrin expression during the first nine days after HSCT with an emerging recovery of receptor expression levels beyond day eleven after transplantation. These data suggest that the mechanisms leading to aberrant platelet surface receptor expression after irradiation are independent of the radiation dose and that newly generated platelets after HSCT share a distinct surface receptor density than resting platelets in untreated animals.

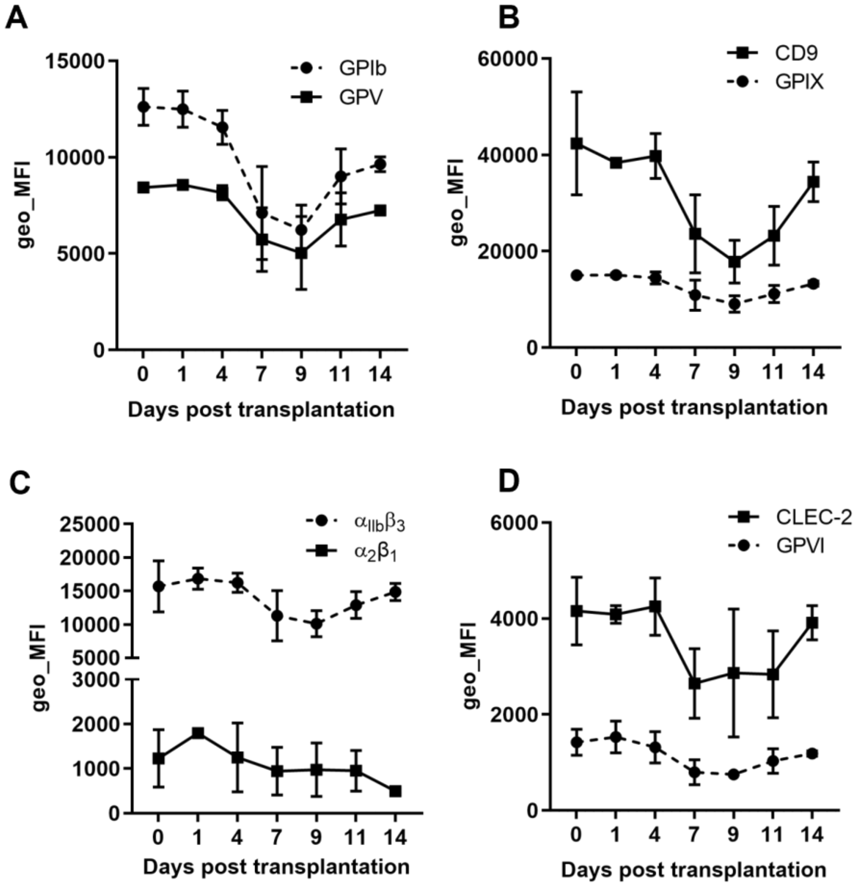

Figure 32. Platelet surface receptor expression after HSCT. (A) Receptor Abundance of GPIb, GPV, (B) GPIX, CD9, C) integrin $\alpha_{IIb}\beta_3$, integrin $\alpha_2\beta_1$ (D) CLEC-2 and GPVI was studied by flow cytometry after HSCT. Data is depicted as the geo-MFI value as mean ± SD. n = 4 to 8 from two independent transplantation experiments.

In a next set of experiments, we studied platelet function after HSCT upon stimulation with thrombin, CRP-X$_L$, or convulxin and measured α-granule release by flow cytometry as described in section 3.4.3. Stimulation of platelets with a high dose of thrombin (0.1 U/ml) triggered increased P-selectin exposure on day one after HSCT, which then gradually declined until day nine. Platelet activation after thrombin stimulation started to normalize again from day eleven after HSCT (Fig. 33A). On the contrary, stimulation of GPVI with high concentrations of CRP-XL (10 µg/ml) led to hardly any degranulation. This massive hyporeactivity persisted from day four until the analysis endpoint on day 14 after HSCT (Fig. 33B). Platelet stimulation with the strong GPVI multimerization agent convulxin rescued this hyporeactive phenotype to some extent on day four after HSCT, but not at the other indicated time points (Fig. 33C). We detected a similar hyporeactivity towards GPVI agonists after sublethal TBI without subsequent HSCT, as shown in section 3.4.3. This hints towards a persisting platelet function defect, which extends into the BM recovery phase after HSCT.

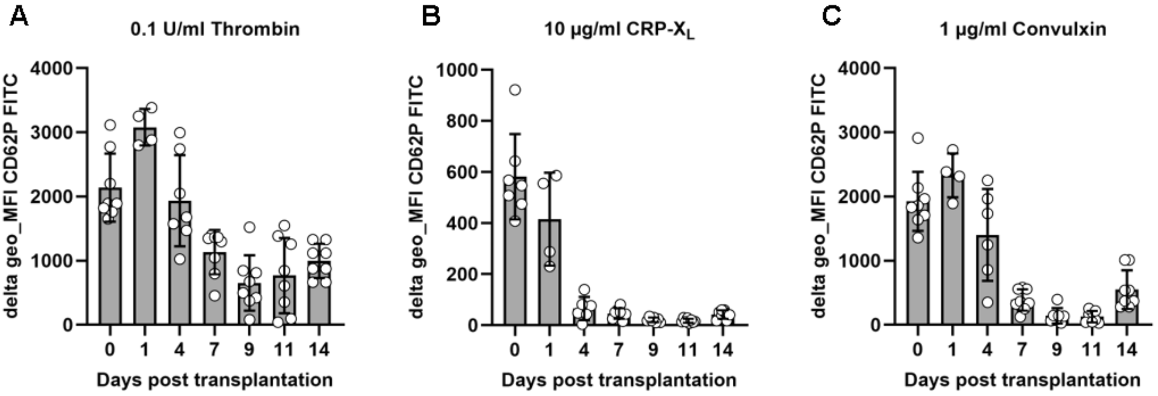

Figure 33. P-selectin (CD62P) exposure of activated platelets after HSCT. (A) Platelet degranulation upon 0.1 U/ml thrombin stimulation. (B) Activation of platelets with the GPVI agonist CRP-X_L (10 µg/ml). (C) Platelet stimulation with 1 µg/ml convulxin. Data is displayed as the delta-geoMFI (mean ± SD). n = 4 to 8 from two independent transplantation experiments.

In summary, we have demonstrated for the first time that TBI-triggered remodeling of the BM led to massively impaired platelet activation and aggregation after BM transplantation, especially upon stimulation of GPVI. This may be due to a defect in the GPVI signal transduction, suggesting a yet unrecognized aspect of platelet dysfunction after TBI, which is important for understanding HSCT-associated bleeding and thrombosis.

4. Discussion

The bone marrow is the main hematopoietic compartment responsible for the generation of all blood cells. Under steady state conditions the human BM produces a massive biomass of 5-10x10^{10} granulocytes, 2x10^{11} erythrocytes and 10^{11} platelets per day, which are continuously replenished from the pool of progenitor cells and released from the abluminal marrow cavity into the blood stream [106-108]. While MKs have been identified as the immediate precursors of platelets, the visualization of thrombopoiesis has proven to be difficult due to the paucity of MKs among the nucleated cells and their localization within the BM, which is embedded into an opaque calcified cortex. Despite these obstacles many efforts have been made to develop techniques to study the transmural migration of (pro)platelets *in situ* and *in vivo*. However, all of these studies describe the direct interaction of MKs with sinusoidal endothelial cells and do not take the perivascular reticular cells into consideration.

In the present study, we have identified CXCL12-abundant reticular (CAR) cells as possible gatekeepers of the transendothelial MK passage and have revealed in an unprecedented ultrastructural resolution the events leading to MK vessel protrusion under steady state conditions. In further experiments we have challenged the MK/sinus interface by TBI and analyzed the mechanisms underlying the niche remodeling after myeloablation and HSCT. We could demonstrate that graft-derived MKs exhibit a distinct engraftment pattern from most other blood cell lineages and that MKs residing in a radiation-injured BM produce functionally altered platelets.

4.1. Identification of CAR cells as regulators of platelet generation

Hematopoiesis is normally a unidirectional process in respect to the permeability of cells through the endothelial lining: mature blood cells are released from the BM into the circulation and do not re-enter the BM. One exception for this enigmatic selectiveness of the blood BM-barrier are hematopoietic stem cells, which are able to cross the endothelium in both directions. The diapedesis of HSCs from the BM into the blood stream can be triggered by stimulation with G-CSF or blockade of the CXCL12 receptor CXCR4 [109, 110]. This mechanism is routinely used by clinicians to mobilize HSCs in donors for human HSCT. The donor graft is typically applied by a central venous catheter into the peripheral blood, where HSCs can then find their way back into the BM (and its niche), a process referred to as stem cell homing [111]. The vasculature is therefore an important player during stem cell homing.

Blood vessel infiltrate virtually all tissues and consist of arteries and veins which branch into smaller arterioles, venules, and capillaries of the microvasculature. Endothelial cells (ECs), that line the luminal side of all blood vessels, exhibit distinct organ-specific properties and give rise to a set of tissue-specific vessel wall morphology and permeability [112]. The capillary bed of the BM is in textbooks traditionally referred to as discontinuous, which means that BM SECs form large gaps to permit passage of blood cells [113]. Interestingly, various early electron microscopic studies on the migration of blood cells through the BM vessel wall have demonstrated that the sinusoidal lining is continuous and that pore formation within the vessel wall only occurs during the diapedetic transit of cells [80, 114-116]. Leon Weiss further characterized BM sinusoids as a trilaminar structure consisting of (1) lining cells (ECs), (2) a basement membrane and (3) pericytes, which form cytoplasmic extensions that envelop hematopoietic cells residing in the perivascular niche [81, 117]. CAR cells among other perivascular stroma cells are a rich source of cytokines, such as CXCL12 and SCF, and play a central role in HSC maintenance. In a seminal study by Avecilla et al. the authors demonstrated in a c-mpl knockout mouse model that TPO-independent thrombopoiesis is facilitated by CXCL12-expressing cells through relocation of MK progenitors to the perivascular niche and promotion of maturation [30]. This study has used classic H&E BM staining and based their results on thin (2D) sections. We have adopted a novel cutting and four-color IF-staining protocol for calcified bones, to be able to draw conclusions about the (co-)localization of different cellular and extracellular structures within the same section. In contrast to H&E staining this allowed us to not only visualize vessels and MKs, but also BM stroma cells (CAR cells in particular) together with matrix proteins, such as collagens, laminins and perlecan [14, 50, 73, 118, 119]. Using this method in combination with TEM and SBF-SEM, we studied the sinus wall for the first time as a whole while achieving a high 2D- and 3D-resolution both in fluorescence microscopy and electron microscopy [73]. In this section, I will discuss three aspects of the MK/vessel wall interaction and proplatelet formation (PPF) that our work has contributed to the understanding of: (1) the location of MKs at the perivascular niche, (2) the continuity of the endothelial lining and (3) the permeability of BM sinusoids for MK protrusions.

By using thin BM cryosections (7 µm) for multicolor CLSM as well as optimization of a staining and clearing procedure for thick bone sections (>200 µm) we mapped CAR cells throughout the whole BM in respect to sinusoids and MKs. We found a dense network of CAR cells enwrapping vessels and MKs, forming multiple close contact sites to both (Fig. 6). Our observations are in line with the common concept that MKs are preferentially located near CAR cells and sinusoids, but now allow to visualize the distribution in a continuous 200 µm section encompassing all relevant components of a BM sinusoidal vessel. Whether this co-localization is due to active migration of MKs or MK progenitors towards CAR cells is a matter of debate. Several studies have reported that targeting the CXCL12/CXCR4 axis triggers MK translocation under inflammatory conditions or after radiation injury in response to a CXCL12 gradient [120-122]. In contrast, by using two-photon microscopy Junt et al. have shown that vessel-residing MKs do not migrate [31]. Recent data from our research group could corroborate this finding by demonstrating that mature GPIX$^+$ MKs do not migrate between the dense vessel network, thereby challenging the concept of *in vivo* migration of mature MKs [82]. However, both studies did not address relocation of HSCs or early megakaryocytic progenitors that may be able to actively migrate towards CXCL12 expressing perivascular cells, such as CAR cells.

By mapping and co-localizing CAR cells together with BM sinusoids and MKs in whole femur sections with multi-color CLSM we were able to analyze vessel-protruding MKs in more detail (Fig. 7, 8). In line with the work by De Bruyn [80, 114], Campbell [115] and Weiss [81, 116, 117] we demonstrated that the sinusoidal endothelial lining is continuous (Fig. 3 in [73]). In our experiments this was emphasized by the heavy metal treatment, required for TEM sample procession, which did not perfuse deep into the BM cavity, but accumulated at the luminal vessel side (Supplementary Fig. 3 in [73]). Although the majority of MKs was located directly at sinusoids, we found only 1.5% of all MKs to breach the endothelium. Most of the SEC-penetrating MKs were not in contact with CAR cells at the site of the protrusion. One limitation of the 2D analysis used for quantifying protruding MKs is the possibility of misjudging proplatelet forming MKs as resting MKs or as “not in contact to CAR cells”, which will finally result in underestimating their actual number/fraction. In order to overcome this limitation, we confirmed our observations by using 3D reconstructions of thick confocal BM volumes and segmented SBF-SEM images thereby demonstrating that MKs are indeed not in contact to CAR cells at the sites of PPF. Based on these analyses, we conclude that CAR cells may act as yet uncharacterized regulators of vessel-directed PPF.

In the last years several mechanisms for the vessel-directed platelet biogenesis *in vivo* have been proposed: The small Rho GTPases Cdc42 and RhoA are regulators of the actin cytoskeleton dynamics and are associated with the formation of cytoskeletal structures involved in adherence and migration, such as stress fibers and filopodia. Mice that lack either Cdc42 or RhoA display a pronounced macrothrombocytopenia [123, 124]. In the absence of RhoA MKs exhibit hyperpolarization due to increased or unbalanced Cdc42 activity, resulting in transmigration of whole MKs into the vasculature. In contrast, lack of Cdc42 results in more MKs with increased distance to vessels. Together, these findings have led to a model providing a MK-intrinsic control mechanism for the transendothelial platelet generation: while Cdc42 acts as a “Go”-signal for PPF, RhoA negatively regulates MK polarization, thereby functioning as a “Stop”-signal [125]. Besides Rho GTPases ECM proteins of the BM are known modulators of platelet biogenesis. Studies using *in vitro* PPF assays demonstrated that collagen type I inhibits PPF, suggesting that this mechanism prevents ectopic platelet release into the BM cavity [14, 97]. However, thrombopoiesis is unaltered in mice that are deficient for both main MK collagen receptors integrin $\alpha_2\beta_1$ and GPVI, suggesting that collagen sensing by either of these receptors plays a minor role for platelet biogenesis *in vivo* [50]. CAR cells now represent a possible third regulatory level for PPF.

Femur sections of irradiated CXCL12-dsRed reporter mice revealed that CAR cell morphology is profoundly altered as a direct consequence of TBI. Under steady state conditions CAR cells enwrap the endothelial lining on the cavity site (Fig. 6). At the radiation-injured sinus wall, we detected cluster formation and presumably retraction of CAR cell protrusions (Fig. 9D). These events were accompanied with massive MK fragmentation and the ectopic release of GPIX$^+$ PLPs into the BM (Fig. 9D). Our observations underpin the hypothesis that CAR cells act as gatekeepers of platelet release. However, direct evidence for an interaction of MKs with CAR cells and their regulatory role still remains to be provided but was beyond the scope of this thesis.

MKs express several surface receptors, such as integrin $\alpha_4\beta_1$ and CXCR4, for which the counterpart ligands (VCAM-1 and CXCL12 respectively) are produced or expressed by CAR cells [100, 126]. Conversely, MK- and platelet-produced substances are known to modulate pericytes in other organs. One example is platelet-derived growth factor (PDGF)-B which was shown to be required for correct attachment of pericytes in the microvasculature of the kidney [127]. Thus, it is likely that CAR cells and MKs are able to directly interact with each other. Besides the receptors and chemokines involved in this interaction, another ambiguity relates to the sequence of events leading to the transendothelial passage of MK protrusions. We have demonstrated that PPF occurs at sites where CAR cells are not in direct contact to MK protrusions (Fig. 7). Yet, it is unclear whether this is due to CAR cell retraction, which is actively triggered by vessel-approaching MKs, or whether MKs "search" for preformed CAR cell-free sites at the abluminal sinus wall. The latter can be observed in a similar way for the transmigration of leukocytes from the blood stream into an inflamed tissue. At the abluminal side, leukocytes search for entry sites in the pericyte cell layer and basement membrane. These leukocyte permissive sites have been shown to be defined by the exclusive presence of laminin α4 and absence of laminin α5 [128]. Although leukocytes and MKs pass the blood BM-barrier in opposite directions, the underlying mechanisms regulating these processes may be similar.

4.2. TBI-triggered BM remodeling and its effect on MK engraftment

The regulation of thrombopoiesis in health and disease is of high clinical relevance, with HSCT being one example for this. With the advancement of HSCT technologies as well as the success of unrelated donor and haploidentical HSCTs, suitable BM donors became readily more available, which is one reason for the steadily rising number of HSCTs over the last three decades [91]. Despite this trend, little is known about the impact of the TBI-triggered changes in the BM on the engraftment of donor cells and MKs in particular. In this study, we mapped the irradiated BM using CLSM, in order to identify the morphological changes triggered by sublethal TBI in respect to MKs, ECM proteins and blood vessels. The data summarized in this study provide evidence that one very early effect of the radiation injury was the dilation of sinusoids, which already began a few hours after treatment (Fig. 9). In the following days after irradiation this vasodilation was accompanied by the degradation of ECM proteins of the sinus basement membrane, in particular collagen type IV and laminin α5 (Fig. 10, 11). The degradation of ECM proteins did not seem to be the main trigger of vasodilation but rather a consequence of the increasing vessel-volume or an independent process.

BM vessel diameters may be influenced by various factors, such as blood flow, intramedullary pressure, or properties of the vessel wall. While different studies on the long-term effects of HSCT and leukemia therapy report an increased intraosseous pressure to be a risk factor for avascular necrosis in survivors of HSCT, there is no information on the BM blood flow during acute radiation injury available [129, 130]. Possible alterations in the intramedullary pressure, which could be due the loss of cellularity after myeloablation are also unexplored. However, TBI-induced vessel wall changes are better studied, although still not fully understood.

Several studies have described a pronounced dilation of BM vessels in response to myeloablation by TBI, 5-fluorouracil (5-FU) or during inflammatory stress [83, 84, 105, 131]. Vasodilation is actively regulated by substances referred to as vasodilators, such as nitric oxide or bradykinin, which induce relaxation of smooth muscle cells around blood vessels [132]. It is not known whether this or a similar mechanism applies to BM sinusoids and TBI-induced vasodilation. Mechanical factors that may influence the vascular perimeter are the different ECM proteins of the basement membrane. Mice with mutations in the genes *Col4a1* and *Col4a2* encoding for the α1- and α2-chains of collagen type IV exhibit (beside several other organ malformations) irregularly shaped and enlarged blood vessels [133-135]. Mice lacking laminin α4 display impaired microvessel maturation, delayed collagen type IV deposition into the basement membrane and extensive hemorrhage [51]. These mouse models emphasize the importance of the proper basement membrane composition for vascular integrity. The vessel-specific laminin α5 knockout model (Lama5^{KO}) used in our study did not show any vascular defect or numeral alterations in peripheral blood leukocytes under steady state conditions, indicating that the lack of laminin α5 did not affect leukocyte transmigration. After challenging the BM by TBI, we found a comparable vasodilation in Lama5^{KO} and wildtype mice (Fig. 10), suggesting that laminin α5 is dispensable for the sinusoidal structure. Although loss of basement membrane proteins could in part explain TBI-triggered vasodilation, this is likely not the only cause. We could measure vasodilation before matrix degradation and loss of cellularity, arguing that vasodilation after TBI is not exclusively due to altered basement membrane properties.

As already briefly discussed in section 4.1, CAR cells undergo morphological alterations after TBI in the way of retraction and clustering around blood vessels. Previous studies from our group have shown that vasodilation after irradiation is a BM-specific phenomenon, that cannot be found in other hematopoietic organs such as the spleen [136]. One possible explanation for this observation could be the different composition of the perivascular niche in the BM and spleen. Splenic sinusoids consist of elongated fusiform endothelial cells that are arranged in a parallel manner thereby forming slits through which blood cells can pass [137]. Vessel stability and contractility is mediated by annular fibers which hold the sinus together like metal straps on a wooden barrel [138]. It is therefore conceivable that BM sinusoids expand after TBI due to the loss of stabilization by ECM proteins and CAR cells, while splenic sinusoids remain unchanged due to their more rigid structure.

Role of matrix metalloproteinase 9

The turnover of matrix proteins in the BM during homeostasis is mediated by the gelatinases MMP2 and especially MMP9. The importance of MMP9 activity during bone development and remodeling is emphasized by the phenotypic malformations that MMP9$^{-/-}$ mice display. Proper long bone formation requires extensive matrix remodeling, endochronal ossification and angiogenesis. Loss of MMP9 leads to growth plate defects due to impaired apoptosis of hypertrophic chondrocytes eventually resulting in shorter femurs [61]. Furthermore, vascular remodeling, bone fracture healing and collagen fiber alignment is impaired in MMP9$^{-/-}$ mice [139-141]. In our study we could demonstrate that activity of the collagen- and laminin-degrading protease MMP9 is upregulated after TBI followed by HSCT and have linked this activity to collagen proteolysis by several complementary zymography-based techniques. Although mice lacking MMP9 exhibited vasodilation to a similar degree as MMP9 wildtype controls, MMP9$^{-/-}$ mice displayed delayed recovery of the vasculature. Beyond the known role of MMP9 in in reconstruction and healing processes after different forms of tissue injury data from this study provide additional experimental evidence that MMP9 plays also a role in vascular recovery after irradiation.

A number of studies have demonstrated that MMP9 is not only involved in BM matrix remodeling, but also in HSC mobilization [110, 142, 143]. Heissig et al. have demonstrated that MMP9 is required for the reconstitution of the hematopoietic compartment after chemotherapeutic myeloablation with 5-FU by mediating the release of soluble kit-ligand [95]. In contrast to these findings, we could not observe an impact of MMP9-deficiency on the engraftment of donor cells, especially of cells of the megakaryocytic lineage. Blood cell counts (data not shown), the number of GPIX$^+$ MKs and the overall distribution of donor-derived cells in the BM of recipient MMP9$^{-/-}$ mice was comparable to that of MMP9$^{+/+}$ control animals. However, vasodilation after HSCT was prolonged in MMP9$^{-/-}$ mice which is in line with our observations in mice treated with "TBI only", as discussed above (Fig. 20). Of note, we have used MMP9 wildtype BM for our transplantation experiments. The apparent dispensability of MMP9 for cell engraftment after HSCT may therefore be either due to graft-derived MMP9 activity or compensatory proteolytic activity by another MMP, for which we have presented the first experimental evidence (Fig. 21, 22).

HSC and MK engraftment

Several factors influence homing and lodgment of HSC to their hematopoietic niche after HSCT. HSC homing is first initiated by their tethering and rolling along the endothelial lining, which is mediated by P-selectin and E-selectin followed by further adhesion through binding of additional receptors. This includes the interaction of integrin $\alpha_4\beta_1$ (VLA-4) with VCAM-1 being of particular importance during this process [144-147]. Transmigration of endothelial-bound HSCs through the vessel wall is then enabled by podosome formation and loss of VE-cadherin function [148].

SECs and BM pericytes express the above-mentioned adhesion molecules and secrete cytokines involved in homing such as SCF and CXCL12. Other abundant sources of CXCL12 within the BM are osteoblasts and osteoclasts residing at the endosteal niche [149]. Deletion of either CXCL12-expressing cells or the CXCL12 receptor CXCR4 leads to reduction of the HSC pool, increased sensitivity of BM stromal cells to myeloablative injury as well as to an overall reduced homing and BM reconstitution after HSCT [3, 4, 9]. Furthermore, differences in the reactive oxygen species (ROS) state of arteriolar ECs and SECs are involved in HSC lodgment [150]. While arterioles maintain a low ROS microenvironment, which facilitates HSC quiescence and self-renewal, the perivascular niche at sinusoids typically constitutes higher levels of ROS promoting HSC differentiation and activation [151]. ROS-mediated oxidative stress leads also to radiation-induced bystander effects after TBI, which can damage transplanted HSCs and impair reconstitution of the recipient BM [68, 152]. These findings underline the importance of an intact stromal BM environment.

In our study we have assessed HSC homing and MK engraftment in whole femur sections of a murine HSCT model, where we used ubiquitously dsRed-expressing mice as BM donors (Fig. 16A). We expected transplanted HSCs to have multiple entry sites in the vasculature of the recipient BM, leading to homogeneous distribution of donor cells. However, we demonstrated for the first time that donor-derived BM cells and among them especially MKs are organized in large clusters preferentially positioned at the femur cortex. This cluster formation may be due to locally altered receptor abundance on the endothelial surface of vasodilated sinusoids or differences in the availability of growth factors.

In our study we have measured serum chemokine levels of mice after HSCT and found peak expression especially of CXCL1, CXCL9 and CCL7. CXCL1 is a chemoattractant for neutrophils that binds to its receptor CXCR2 and is reported to play an important role in the inflammatory response by orchestrating the diapedesis of neutrophils through the endothelial wall [153]. Although the direction of the transendothelial passage of immune cells (namely from the circulation into a tissue) differs from that of platelet-forming MKs (from the BM into the circulation), CXCL1 may be an interesting candidate for studies on the transmural penetration of MK protrusions. Beyond its role during inflammation CXCR2 influences the differentiation of HSCs to megakaryocytic progenitors [154]. CXCR2 could therefore be involved in MK progenitor differentiation after myeloablation. CCL7, also known as monocyte-chemotactic protein 3 (MCP3) influences leukocyte migration and is critical for monocyte mobilization from the BM and recruitment to sites of inflammation [155]. Local overexpression of CCL7 in a mouse model of myocardial infarction led to the recruitment of BM-derived mesenchymal stem cell homing to the infarcted myocardium, demonstrating the ability of CCL7 to influence MSC trafficking to sites of injury [156]. CCL7 would therefore be another candidate for further analyses regarding BM recovery after HSCT.

CXCL9 is mainly secreted by macrophages during inflammation. Interestingly, CXCL9 is also produced by osteoblasts in the BM and was identified to act as an angiostatic factor regulating bone angiogenesis and osteogenesis [157]. Future studies on the remodeling of the BM vasculature after TBI and HSCT could therefore aim to decipher the role of CXCL9 in this process.

Our study demonstrated that the BM niche is heavily remodeled after radiation injury, including ECM proteins and CAR cells. However, we did not study possible TBI-induced bystander effects, which could influence HSC engraftment and cluster formation. A frequently used murine HSCT model are non-obese diabetic/severe combined immunodeficient (NOD/SCID) mice, which can be xenotransplanted with human CD34$^+$ HSCs. One major advantage of this model is that donor cell engraftment can be achieved without the need of myeloablation prior to transplantation, making it possible to study human HSC engraftment in an uncompromised BM compartment [158]. Although there are several reports that describe MK and platelet engraftment using this mouse model [159, 160], there is no information on the distribution of MKs or donor cells in the recipient BM. Future studies with NOD/SCID mice may therefore help to identify factors influencing HSC distribution after HSCT and the role of the radiation-damaged BM in this process.

The primary aim of this thesis was to decipher the mechanisms underlying prolonged thrombocytopenia after HSCT in order to either attenuate or shorten the thrombocytopenic phase after transplantation. A new question that has arisen based on our findings, is whether donor cell and MK cluster formation contributes to prolonged thrombocytopenia and whether MK engraftment can be improved by the generation of more suitable lodgment sites for MK progenitors. Currently, there are two methods in experimental approaches used to improve platelet counts after HSCT: (1) graft manipulation and (2) the use of thrombopoietin receptor agonists. Graft manipulation is a procedure frequently applied to customize and optimize cells for a patient prior to transplantation. This can be achieved by e.g., physical manipulation in terms of antibody washing and volume reduction. Another type of graft manipulation are measures to deplete cells (like CD3$^+$ T cells) that are associated with poor engraftment and risk factors such as graft-versus-host disease (GvHD) or to enrich a certain cell population (CD34$^+$ cells) [161, 162]. So far, graft manipulation is not used to specifically enhance MK and platelet engraftment. However, studies have shown that enrichment of a graft with CD34$^+$ cells that have been cultured *ex vivo* with TPO or co-transplantation of mesenchymal stem cells accelerated platelet engraftment [163, 164].

The thrombopoietin receptor agonists eltrombopag and romiplostim are FDA- and EMA-approved drugs for the treatment of immune thrombocytopenic purpura (ITP) and are currently in clinical trial for the use after HSCT, as reviewed by Mahat et al. [92]. Responders to treatment, indicated by an increase in platelet counts to levels of at least $50x10^9$/l was seen in about 70% of patients treated with eltrombopag and in 82% of patients that received romiplostim. Although there have been reports describing romiplostim-induced myelofibrosis [165, 166], thrombopoietin receptor agonists are nonetheless promising tools for the treatment of prolonged post-HSCT thrombocytopenia.

4.3. Platelets are functionally altered after myeloablation

As discussed in the previous section (4.2.), prolonged thrombocytopenia and hemorrhage is a common problem after HSCT. Whether this is accompanied by functional platelet defects has not been studied yet. In this thesis, we are the first to describe a platelet function defect in the early phase after TBI and HSCT. We could show that platelets become hyporeactive both after sublethal TBI and HSCT, which we studied by flow cytometry on a single cell level (Fig. 29, 33) and by aggregometry (Fig. 30). The GPVI signaling pathway appeared to be particularly affected in this context (Fig. 31), while GPVI surface expression was reduced by half compared to untreated controls (Fig. 28D, 32D).

One obvious bias of our analyses is the thrombocytopenia after TBI and HSCT, which can (in whole blood without adjusting the platelet count) influence functional responses in some assays. However, flow cytometry is not that prone to skew results when thrombocytopenic blood is analyzed. This method is thus routinely used to evaluate platelet defects in thrombocytopenic patients or in very young patients for which the blood volume is limited and aggregometry cannot be applied. For aggregometry experiments in this study, we have adjusted platelet counts prior to adding the agonists (Fig. 30). Still, future analyses at later time points after HSCT, when MK engraftment has occurred and platelet counts have normalized, are highly relevant. Preliminary data from our work group indicate that depending on how many cells have been used for transplantation, this time point is reached between two and four weeks after HSCT and that an incomplete BM chimerism can be achieved by that time, meaning that recipient-derived and donor-derived hematopoietic cells coexist in the recipient’s BM (mixed chimerism). This allowed us to study recipient- and donor-derived platelets originated from the same mouse and thereby internally controlled in the same experiment. The results from this experiment suggest that donor-derived platelets are hyperreactive, while the platelet population as a whole still shows a hyporeactive response, indicating that functional abnormalities of a minor platelet sub-population are masked within the entirety of the platelet population. Although our findings are still preliminary and need to be confirmed by further experiments, due to the fact that they are internally controlled, they provide *bona fide* experimental evidence towards the existence of MK subpopulations in the BM that give rise to platelets with different functional properties. This may help to understand why bleedings and thrombotic events can co-exist in patients after HSCT, with platelet subpopulations reacting actively to triggers, while other platelets become passively incorporated into a growing thrombus. This observation will thus be followed by our group to further provide a better understanding of the consequences of the mixed platelet chimerism after HSCT.

Recent studies using single-cell RNA (scRNA) sequencing have reported MK cellular heterogeneity already on a MK progenitor level, both for the murine as well as for the human BM, and identified distinct MK subpopulations, including MKs with immune characteristics or with priming towards the generation of platelets [167]. This means that while MKs in one individual exhibit already certain (and clearly distinguishable) differences among themselves, BM chimerism after allogeneic HSCT adds another layer to this by introducing cells that are genetically different from the recipient's own BM cells. Diploid mammalian cells usually express the maternally and paternally inherited genes in an equal manner. However, scRNA sequencing using mouse blastocysts and human fibroblasts suggests that some genes can differ in their allelic burst frequency and size, leading to expression variability in single cells, as recently reviewed by Heemskerk and West [168]. These findings implicate that one megakaryocyte may generate platelets with transcripts from one or two alleles [169]. These differences in the allele-specific transcription within one, as well as between individuals could explain how the same heterogeneous mutation can lead to variable platelet defects even within one family [170]. It is also not clear how MK polyploidy and asymmetrical PPF affect platelet heterogeneity. The question of whether all the above-described factors reported to influence

MK heterogeneity also play a role in MK engraftment and platelet function after HSCT, has not yet been addressed.

Besides the variability of platelets under steady state conditions, several studies in humans and mice have shown that various infectious diseases, such as sepsis or dengue virus infection affect the BM niche and also alter the MK (and consequently the platelet) transcriptome. MKs in the inflamed BM give rise to functionally altered platelets especially affecting the GPVI signaling pathway [171-174]. Moreover, there are reports on platelet-associated hemostatic dysfunctions in patients with hereditary collagenopathies, such as in Ehlers-Danlos syndrome or in Osteogenesis imperfecta [175-177]. Recently, it was demonstrated that collagen VI-deficient mice generate hyperreactive platelets, corroborating the role of the ECM matrix environment for platelet function [178]. In line with these findings, our observations in response to HSCT suggest that an aberrant BM niche leads to functionally altered platelets. How exactly the BM microenvironment after HSCT regulates platelet function and how sustainable the functional changes are, requires further investigations.

4.4. Outlook and concluding remarks

Thrombopoiesis under homeostatic conditions

The experimental findings presented in the first part of this thesis shed light on a so far underappreciated component of the BM vessel wall and a possible novel player in the regulation of *in vivo* PPF. We are the first to propose CAR cells as gatekeepers of the SEC/MK interface, which prevent/enable the interaction of MKs with the endothelial lining and direct MK protrusions into the blood stream. Our results led us to develop the following hypothesis: resting MKs reside at BM sinusoids and are in contact to CAR cells. At the sites of proplatelet formation, CAR cells retract in order to let cytoplasmic MK protrusion penetrate the basement membrane and SECs. MKs then breach the endothelial wall through a newly formed pore to release large proplatelets into the circulation (Fig. 34) [73].

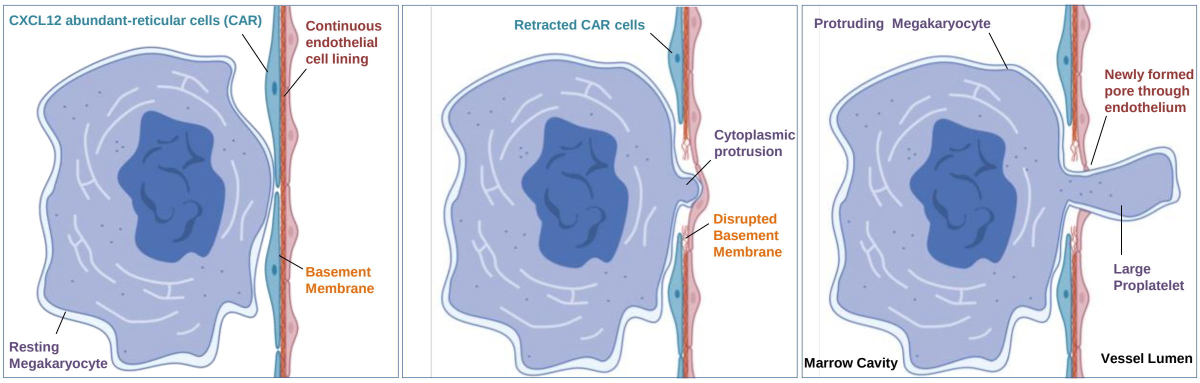

Fig. 34. Model of CAR cell-mediated regulation of PPF. Resting MKs at the vessel wall are in contact to CAR cells that retract at sites of PPF to enable SEC penetration by MK protrusions and proplatelet release into the vessel lumen. (Image taken from [73]).

This hypothesis opens up a series of new, unanswered questions. Our study has so far focused on CAR cells and not on other pericytes or perivascular cells respectively. Thus, one question is whether the vascular niche harbors additional perivascular cell populations, which may be associated with MKs. Vascular niche cells are an abundant source of cytokines and chemokines. A next question is therefore whether these cells produce MK-active mediators and how these may affect thrombopoiesis.

Finally, the physiological and pathophysiological relevance of MK/perivascular cell interactions remain to be elucidated. In future studies, we want to address the questions raised above to achieve a better understanding of the basal mechanisms, which modulate platelet biogenesis. This knowledge will pave the way for new therapeutic measures to target abnormal thrombopoiesis under disease conditions, such as sepsis or after HSCT.

Thrombopoiesis under pathological conditions

In this thesis, we have unprecedentedly demonstrated that the megakaryocytic lineage exhibits a distinct engraftment pattern and that the function of platelets generated in the transplanted niche is severely impaired after HSCT. We were the first to question whether cells that derive from a healthy donor BM are functional and assess this by several complementary assays (flow cytometry, aggregometry, immunoblot).

In future experiments, we will study the platelet function defect found after HSCT in other functional assays, such as *in vitro* / *in vivo* thrombus formation or tail bleeding time, to evaluate whether this has an impact on the ability of platelets to form a thrombus or a hemostatic plaque.

We have shown that the engraftment kinetic of the different BM lineages in our murine HSCT model reflects the post transplantation hematopoiesis in human HSCT patients, thereby validating our experimental mouse model as a tool to study the development of the blood cell lineages after HSCT. However, it is not clear whether the aberrant platelet function in transplanted mice mimics post HSCT platelet function in humans. Severe side effects of HSCT, such as life-threatening infections or bleeding are mostly attributed to low immune cell and platelet numbers. So far, there are no reports on functional defects of graft-derived blood cells and especially platelets in the context of HSCT-related complications. HSCT is not only related to thrombocytopenia and hemorrhage, but paradoxically also to thromboembolic events that suggest that altered platelet function may play a role in the events leading to thrombosis after HSCT. We will therefore extent our platelet studies to human HSCT patients in order to determine the impact of platelet function on bleeding tendency and thromboembolism after HSCT.

The findings presented in this study and the future experiments contribute to the understanding of thrombopoiesis during homeostatic conditions and disease, which will help to develop novel treatments for patients suffering from aberrant platelet biogenesis.

5. References

1. Nimmo, R.A., G.E. May, and T. Enver, *Primed and ready: understanding lineage commitment through single cell analysis.* Trends in cell biology, 2015. **25**(8): p. 459-467.
2. Yamamoto, R., et al., *Clonal Analysis Unveils Self-Renewing Lineage-Restricted Progenitors Generated Directly from Hematopoietic Stem Cells.* Cell, 2013. **154**(5): p. 1112-1126.
3. Omatsu, Y., et al., *The essential functions of adipo-osteogenic progenitors as the hematopoietic stem and progenitor cell niche.* Immunity, 2010. **33**(3): p. 387-99.
4. Sugiyama, T., et al., *Maintenance of the hematopoietic stem cell pool by CXCL12-CXCR4 chemokine signaling in bone marrow stromal cell niches.* Immunity, 2006. **25**(6): p. 977-988.
5. Broudy, V.C., *Stem Cell Factor and Hematopoiesis.* Blood, 1997. **90**(4): p. 1345-1364.
6. Williams, D.E., et al., *Identification of a ligand for the c-kit proto-oncogene.* Cell, 1990. **63**(1): p. 167-74.
7. Yuzawa, S., et al., *Structural basis for activation of the receptor tyrosine kinase KIT by stem cell factor.* Cell, 2007. **130**(2): p. 323-334.
8. Peled, A., et al., *Dependence of human stem cell engraftment and repopulation of NOD/SCID mice on CXCR4.* Science, 1999. **283**(5403): p. 845-848.
9. Singh, P., K.S. Mohammad, and L.M. Pelus, *CXCR4 expression in the bone marrow microenvironment is required for hematopoietic stem and progenitor cell maintenance and early hematopoietic regeneration after myeloablation.* Stem Cells, 2020. **38**(7): p. 849-59.
10. Zubicaray, J., et al., *Plerixafor-based mobilization in pediatric healthy donors with unfavorable donor/recipient body weight ratio resulted in a better CD34(+) collection yield: A retrospective analysis.* J Clin Apher, 2021. **36**(1): p. 78-86.
11. Black, J.D.J. and B.J. Tadros, *Bone structure: from cortical to calcium.* Orthopaedics and Trauma, 2020. **34**(3): p. 113-119.
12. Crane, G.M., E. Jeffery, and S.J. Morrison, *Adult haematopoietic stem cell niches.* Nature Reviews Immunology, 2017. **17**(9): p. 573-590.
13. Kunisaki, Y., *Pericytes in bone marrow.* Pericyte Biology in Different Organs, 2019: p. 101-114.
14. Semeniak, D., et al., *Proplatelet formation is selectively inhibited by collagen type I through Syk-independent GPVI signaling.* J Cell Sci, 2016. **129**(18): p. 3473-84.
15. Gomariz, A. and P.M. Helbling, *Quantitative spatial analysis of haematopoiesis-regulating stromal cells in the bone marrow microenvironment by 3D microscopy.* Nature Communications, 2018. **9**(1): p. 2532.
16. Kunisaki, Y., et al., *Arteriolar niches maintain haematopoietic stem cell quiescence.* Nature, 2013. **502**(7473): p. 637-43.
17. Ding, L., et al., *Endothelial and perivascular cells maintain haematopoietic stem cells.* Nature, 2012. **481**(7382): p. 457-462.
18. Aoki, K., et al., *Identification of CXCL12-abundant reticular cells in human adult bone marrow.* British Journal of Haematology, 2021. **193**(3): p. 659-668.
19. Lewis, K., M. Yoshimoto, and T. Takebe, *Fetal liver hematopoiesis: from development to delivery.* Stem Cell Research & Therapy, 2021. **12**(1): p. 139.
20. Cenariu, D., et al., *Extramedullary Hematopoiesis of the Liver and Spleen.* Journal of clinical medicine, 2021. **10**(24): p. 5831.
21. Lefrançais, E., et al., *The lung is a site of platelet biogenesis and a reservoir for haematopoietic progenitors.* Nature, 2017. **544**(7648): p. 105-109.
22. Italiano, J.E., Jr., et al., *Blood platelets are assembled principally at the ends of proplatelet processes produced by differentiated megakaryocytes.* J Cell Biol, 1999. **147**(6): p. 1299-312.
23. Wickramasinghe, S.N., A. Porwit, and W.N. Erber, *CHAPTER 2 - Normal bone marrow cells: Development and cytology*, in *Blood and Bone Marrow Pathology (Second*

Edition), A. Porwit, J. McCullough, and W.N. Erber, Editors. 2011, Churchill Livingstone: Edinburgh. p. 19-44.
24. Tilburg, J., I.C. Becker, and J.E. Italiano, *Don't you forget about me(gakaryocytes).* Blood, 2021.
25. Kaushansky, K., *The molecular mechanisms that control thrombopoiesis.* The Journal of clinical investigation, 2005. **115**(12): p. 3339-3347.
26. Murone, M., D.A. Carpenter, and F.J. de Sauvage, *Hematopoietic deficiencies in c-mpl and TPO knockout mice.* Stem Cells, 1998. **16**(1): p. 1-6.
27. Ballmaier, M., et al., *c-mpl mutations are the cause of congenital amegakaryocytic thrombocytopenia.* Blood, 2001. **97**(1): p. 139-146.
28. Ballmaier, M., et al., *Thrombopoietin in Patients With Congenital Thrombocytopenia and Absent Radii: Elevated Serum Levels, Normal Receptor Expression, But Defective Reactivity to Thrombopoietin.* Blood, 1997. **90**(2): p. 612-619.
29. Fielder, P.J., et al., *Regulation of Thrombopoietin Levels by c-mpl–Mediated Binding to Platelets.* Blood, 1996. **87**(6): p. 2154-2161.
30. Avecilla, S.T., et al., *Chemokine-mediated interaction of hematopoietic progenitors with the bone marrow vascular niche is required for thrombopoiesis.* Nat Med, 2004. **10**(1): p. 64-71.
31. Junt, T., et al., *Dynamic visualization of thrombopoiesis within bone marrow.* Science, 2007. **317**(5845): p. 1767-70.
32. Bender, M., et al., *Microtubule sliding drives proplatelet elongation and is dependent on cytoplasmic dynein.* Blood, 2015. **125**(5): p. 860-8.
33. Patel-Hett, S., et al., *Visualization of microtubule growth in living platelets reveals a dynamic marginal band with multiple microtubules.* Blood, 2008. **111**(9): p. 4605-16.
34. de Botton, S., et al., *Platelet formation is the consequence of caspase activation within megakaryocytes.* Blood, 2002. **100**(4): p. 1310-1317.
35. Evans, A.L., et al., *Transfer to the clinic: refining forward programming of hPSCs to megakaryocytes for platelet production in bioreactors.* Blood advances, 2021. **5**(7): p. 1977-1990.
36. Thon, J.N., B.J. Dykstra, and L.M. Beaulieu, *Platelet bioreactor: accelerated evolution of design and manufacture.* Platelets, 2017. **28**(5): p. 472-477.
37. Nakamura, S., N. Sugimoto, and K. Eto, *Ex vivo generation of platelet products from human iPS cells.* Inflammation and regeneration, 2020. **40**(1): p. 30-30.
38. Brown, E., et al., *Multiple membrane extrusion sites drive megakaryocyte migration into bone marrow blood vessels.* Life science alliance, 2018. **1**(2): p. e201800061.
39. Eckly, A., et al., *Megakaryocytes use in vivo podosome-like structures working collectively to penetrate the endothelial barrier of bone marrow sinusoids.* Journal of Thrombosis and Haemostasis, 2020. **18**(11): p. 2987-3001.
40. Boscher, J., et al., *Blood platelet formation at a glance.* Journal of Cell Science, 2020. **133**(20).
41. Schachtner, H., et al., *Megakaryocytes assemble podosomes that degrade matrix and protrude through basement membrane.* Blood, 2013. **121**(13): p. 2542-2552.
42. Maynard, D.M., et al., *Proteomic analysis of platelet alpha-granules using mass spectrometry.* J Thromb Haemost, 2007. **5**(9): p. 1945-55.
43. Koseoglu, S. and R. Flaumenhaft, *Advances in platelet granule biology.* Curr Opin Hematol, 2013. **20**(5): p. 464-71.
44. Varga-Szabo, D., I. Pleines, and B. Nieswandt, *Cell Adhesion Mechanisms in Platelets.* Arteriosclerosis, Thrombosis, and Vascular Biology, 2008. **28**(3): p. 403-412.
45. Nurden, A., *Profiling the Genetic and Molecular Characteristics of Glanzmann Thrombasthenia: Can It Guide Current and Future Therapies?* J Blood Med, 2021. **12**: p. 581-599.
46. Lee-Thedieck, C., P. Schertl, and G. Klein, *The extracellular matrix of hematopoietic stem cell niches.* Advanced Drug Delivery Reviews, 2022. **181**: p. 114069.
47. Malara, A., et al., *Megakaryocytes contribute to the bone marrow-matrix environment by expressing fibronectin, type IV collagen, and laminin.* Stem Cells, 2014. **32**(4): p. 926-37.

48. Smith, C.W., et al., *Mice lacking the inhibitory collagen receptor LAIR-1 exhibit a mild thrombocytosis and hyperactive platelets.* Arteriosclerosis, thrombosis, and vascular biology, 2017. **37**(5): p. 823-835.
49. Abbonante, V., et al., *Discoidin domain receptor 1 protein is a novel modulator of megakaryocyte-collagen interactions.* Journal of Biological Chemistry, 2013. **288**(23): p. 16738-16746.
50. Semeniak, D., et al., *Impact of Itga2-Gp6-double collagen receptor deficient mice for bone marrow megakaryocytes and platelets.* PLOS ONE, 2019. **14**(8): p. e0216839.
51. Thyboll, J., et al., *Deletion of the laminin alpha4 chain leads to impaired microvessel maturation.* Molecular and cellular biology, 2002. **22**(4): p. 1194-1202.
52. Sonnenberg, A., P.W. Modderman, and F. Hogervorst, *Laminin receptor on platelets is the integrin VLA-6.* Nature, 1988. **336**(6198): p. 487-489.
53. Schaff, M., et al., *Integrin α6β1 is the main receptor for vascular laminins and plays a role in platelet adhesion, activation, and arterial thrombosis.* Circulation, 2013. **128**(5): p. 541-552.
54. Page-McCaw, A., A.J. Ewald, and Z. Werb, *Matrix metalloproteinases and the regulation of tissue remodelling.* Nature Reviews Molecular Cell Biology, 2007. **8**: p. 221.
55. Hadler-Olsen, E., et al., *Regulation of matrix metalloproteinase activity in health and disease.* The FEBS Journal, 2011. **278**(1): p. 28-45.
56. Creemers, E.E., et al., *Matrix metalloproteinase inhibition after myocardial infarction: a new approach to prevent heart failure?* Circulation research, 2001. **89**(3): p. 201-210.
57. Stickens, D., et al., *Altered endochondral bone development in matrix metalloproteinase 13-deficient mice.* Development, 2004. **131**(23): p.5883-5895.
58. Oh, J., et al., *Mutations in two matrix metalloproteinase genes, MMP-2 and MT1-MMP, are synthetic lethal in mice.* Oncogene, 2004. **23**(29): p. 5041-5048.
59. Coussens, L.M., B. Fingleton, and L.M. Matrisian, *Matrix Metalloproteinase Inhibitors and Cancer—Trials and Tribulations.* Science, 2002. **295**(5564): p. 2387-2392.
60. Lambert, V., et al., *MMP-2 and MMP-9 synergize in promoting choroidal neovascularization.* The FASEB Journal, 2003. **17**(15): p. 2290-2292.
61. Vu, T.H., et al., *MMP-9/gelatinase B is a key regulator of growth plate angiogenesis and apoptosis of hypertrophic chondrocytes.* Cell, 1998. **93**(3): p. 411-422.
62. Lee, S., et al., *Processing of VEGF-A by matrix metalloproteinases regulates bioavailability and vascular patterning in tumors.* The Journal of cell biology, 2005. **169**(4): p. 681-691.
63. Yu, X.F. and Z.C. Han, *Matrix metalloproteinases in bone marrow: roles of gelatinases in physiological hematopoiesis and hematopoietic malignancies.* Histol Histopathol, 2006. **21**(5): p. 519-31.
64. Hübel, K., *Mobilization and Collection of HSC*, in *The EBMT Handbook: Hematopoietic Stem Cell Transplantation and Cellular Therapies*, E. Carreras, et al., Editors. 2019, Springer, Copyright 2019, EBMT and the Author(s). Cham (CH). p. 117-22.
65. Nagler, A. and A. Shimoni, *Conditioning*, in *The EBMT Handbook: Hematopoietic Stem Cell Transplantation and Cellular Therapies*, E. Carreras, et al., Editors. 2019, Springer, Copyright 2019, EBMT and the Author(s). Cham (CH). p. 99-107.
66. Heinzelmann, F., et al., *Total-Body Irradiation—Role and Indications.* Strahlentherapie und Onkologie, 2006. **182**(4): p. 222-230.
67. Peters, C., et al., *Total Body Irradiation or Chemotherapy Conditioning in Childhood ALL: A Multinational, Randomized, Noninferiority Phase III Study.* Journal of Clinical Oncology, 2021. **39**(4): p. 295-307.
68. Hu, L., X. Yin, and Y. Zhang, *Radiation-induced bystander effects impair transplanted human hematopoietic stem cells via oxidative DNA damage.* Blood, 2021. **137**(24): p. 3339-3350.
69. Carreras, E., et al., *The EBMT handbook: hematopoietic stem cell transplantation and cellular therapies.* 2019.

70. Cao, Y.-A., et al., *Molecular Imaging Using Labeled Donor Tissues Reveals Patterns of Engraftment, Rejection, and Survival in Transplantation.* Transplantation, 2005. **80**(1): p. 134-139.
71. Heib, T., et al., *Isolation of murine bone marrow by centrifugation or flushing for the analysis of hematopoietic cells - a comparative study.* Platelets, 2021. **32**(5): p. 601-607.
72. Nagy, Z., et al., *Interplay between the tyrosine kinases Chk and Csk and phosphatase PTPRJ is critical for regulating platelets in mice.* Blood, 2020. **135**(18): p. 1574-1587.
73. Wagner, N., et al., *CXCL12-Abundant Reticular (CAR) Cells Direct Megakaryocyte Protrusions across the Bone Marrow Sinusoid Wall.* Cells, 2021. **10**(4).
74. Lok, S. and D.C. Foster, *The structure, biology and potential therapeutic applications of recombinant thrombopoietin.* Stem Cells, 1994. **12**(6): p. 586-598.
75. Lok, S., et al., *Cloning and expression of murine thrombopoietin cDNA and stimulation of platelet production in vivo.* Nature, 1994. **369**(6481): p. 565-568.
76. Kawamoto, T. and M. Shimizu, *A method for preparing 2-to 50-µm-thick fresh-frozen sections of large samples and undecalcified hard tissues.* Histochemistry and cell biology, 2000. **113**(5): p. 331-339.
77. Caplan, A.I., *Mesenchymal stem cells.* Journal of orthopaedic research, 1991. **9**(5): p. 641-650.
78. Méndez-Ferrer, S., et al., *Mesenchymal and haematopoietic stem cells form a unique bone marrow niche.* Nature, 2010. **466**(7308): p. 829-834.
79. Greenbaum, A., et al., *CXCL12 in early mesenchymal progenitors is required for haematopoietic stem-cell maintenance.* Nature, 2013. **495**(7440): p. 227-230.
80. De Bruyn, P.P., S. Michelson, and T.B. Thomas, *The migration of blood cells of the bone marrow through the sinusoidal wall.* J Morphol, 1971. **133**(4): p. 417-37.
81. Weiss, L., *The hematopoietic microenvironment of the bone marrow: an ultrastructural study of the stroma in rats.* Anat Rec, 1976. **186**(2): p. 161-84.
82. Stegner, D., et al., *Thrombopoiesis is spatially regulated by the bone marrow vasculature.* Nat Commun, 2017. **8**(1): p. 127.
83. Li, X.M., et al., *Bone marrow sinusoidal endothelial cells undergo nonapoptotic cell death and are replaced by proliferating sinusoidal cells in situ to maintain the vascular niche following lethal irradiation.* Exp Hematol, 2008. **36**(9): p. 1143-1156.
84. Slayton, W.B., et al., *The role of the donor in the repair of the marrow vascular niche following hematopoietic stem cell transplant.* Stem Cells, 2007. **25**(11): p. 2945-2955.
85. Paul, D.S., et al., *Deletion of the Arp2/3 complex in megakaryocytes leads to microthrombocytopenia in mice.* Blood advances, 2017. **1**(18): p. 1398-1408.
86. Prislovsky, A., et al., *Rapid platelet turnover in WASP (−) mice correlates with increased ex vivo phagocytosis of opsonized WASP (−) platelets.* Experimental hematology, 2008. **36**(5): p. 609-623.
87. Spindler, M., et al., *ADAP deficiency impairs megakaryocyte polarization with ectopic proplatelet release and causes microthrombocytopenia.* Blood, The Journal of the American Society of Hematology, 2018. **132**(6): p. 635-646.
88. Yousif, L.F., J. Di Russo, and L. Sorokin, *Laminin isoforms in endothelial and perivascular basement membranes.* Cell adhesion & migration, 2013. **7**(1): p. 101-110.
89. Jalali, S., et al., *Integrin-mediated mechanotransduction requires its dynamic interaction with specific extracellular matrix (ECM) ligands.* Proceedings of the National Academy of Sciences, 2001. **98**(3): p. 1042-1046.
90. Wu, C., et al., *Endothelial basement membrane laminin α5 selectively inhibits T lymphocyte extravasation into the brain.* Nature medicine, 2009. **15**(5): p. 519-527.
91. Passweg, J.R., et al., *Hematopoietic cell transplantation and cellular therapy survey of the EBMT: monitoring of activities and trends over 30 years.* Bone Marrow Transplantation, 2021. **56**(7): p. 1651-1664.
92. Mahat, U., S.J. Rotz, and R. Hanna, *Use of Thrombopoietin Receptor Agonists in Prolonged Thrombocytopenia after Hematopoietic Stem Cell Transplantation.* Biology of Blood and Marrow Transplantation, 2020. **26**(3): p. e65-e73.

93. Labrador, J., et al., *Analysis of incidence, risk factors and clinical outcome of thromboembolic and bleeding events in 431 allogeneic hematopoietic stem cell transplantation recipients.* Haematologica, 2013. **98**(3): p. 437.
94. Heazlewood, S.Y., et al., *Analyzing hematopoietic stem cell homing, lodgment, and engraftment to better understand the bone marrow niche.* Annals of the New York Academy of Sciences, 2014. **1310**(1): p. 119-128.
95. Heissig, B., et al., *Recruitment of stem and progenitor cells from the bone marrow niche requires MMP-9 mediated release of kit-ligand.* Cell, 2002. **109**(5): p. 625-637.
96. Heissig, B., et al., *Low-dose irradiation promotes tissue revascularization through VEGF release from mast cells and MMP-9-mediated progenitor cell mobilization.* J Exp Med, 2005. **202**(6): p. 739-50.
97. Balduini, A., et al., *Adhesive receptors, extracellular proteins and myosin IIA orchestrate proplatelet formation by human megakaryocytes.* Journal of thrombosis and haemostasis, 2008. **6**(11): p. 1900-1907.
98. Dame, C., G. Gaedicke, and H. Schulze, *Physiologie der Megakaryopoiese und des Thrombozyten.* Monatsschrift Kinderheilkunde, 2006. **154**(6): p. 502-509.
99. Watari, K., et al., *Serum G-CSF levels in healthy volunteers and patients with various disorders as estimated by enzyme immunoassay.* Blood, 1989. **73**: p. 117-22.
100. Hamada, T., et al., *Transendothelial Migration of Megakaryocytes in Response to Stromal Cell-derived Factor 1 (SDF-1) Enhances Platelet Formation.* Journal of Experimental Medicine, 1998. **188**(3): p. 539-548.
101. Sitnicka, E., et al., *Transforming growth factor beta 1 directly and reversibly inhibits the initial cell divisions of long-term repopulating hematopoietic stem cells.* Blood, 1996. **88**(1): p. 82-8.
102. Soma, T., J.M. Yu, and C.E. Dunbar, *Maintenance of murine long-term repopulating stem cells in ex vivo culture is affected by modulation of transforming growth factor-beta but not macrophage inflammatory protein-1 alpha activities.* Blood, 1996. **87**(11): p. 4561-7.
103. Hatzfeld, J., et al., *Release of early human hematopoietic progenitors from quiescence by antisense transforming growth factor beta 1 or Rb oligonucleotides.* J Exp Med, 1991. **174**(4): p. 925-9.
104. Labrador, J., et al., *Incidence and risk factors for life-threatening bleeding after allogeneic stem cell transplant.* British Journal of Haematology, 2015. **169**(5): p. 719-725.
105. Narayan, K., S. Juneja, and C. Garcia, *Effects of 5-fluorouracil or total-body irradiation on murine bone marrow microvasculature.* Exp Hematol, 1994. **22**(2): p. 142-8.
106. Summers, C., et al., *Neutrophil kinetics in health and disease.* Trends in immunology, 2010. **31**(8): p. 318-324.
107. Rivella, S. and B.J. Crielaard, *Disorders of Iron Metabolism: Iron Deficiency and Iron Overload and Anemia of Chronic Diseases*, in *Pathobiology of Human Disease*, L.M. McManus and R.N. Mitchell, Editors. 2014, Academic Press: San Diego. p. 1471-1487.
108. Hartwig, J., *Production and destruction of platelets*, in *The Non-Thrombotic Role of Platelets in Health and Disease*. 2015, IntechOpen.
109. Rettig, M.P., G. Ansstas, and J.F. DiPersio, *Mobilization of hematopoietic stem and progenitor cells using inhibitors of CXCR4 and VLA-4.* Leukemia, 2012. **26**(1): p. 34-53.
110. Hoggatt, J., et al., *Rapid Mobilization Reveals a Highly Engraftable Hematopoietic Stem Cell.* Cell, 2018. **172**(1-2): p. 191-204.e10.
111. Kenyon, M. and A. Babic, *The European Blood and Marrow Transplantation Textbook for Nurses: Under the Auspices of EBMT.* 2018.
112. Potente, M. and T. Mäkinen, *Vascular heterogeneity and specialization in development and disease.* Nature Reviews Molecular Cell Biology, 2017. **18**(8): p. 477-494.
113. Welsch, U. and T. Deller, *Histologie-Das Lehrbuch*. 2018: Elsevier Health Sciences.
114. Becker, R.P. and P.P. De Bruyn, *The transmural passage of blood cells into myeloid sinusoids and the entry of platelets into the sinusoidal circulation; a scanning electron microscopic investigation.* Am J Anat, 1976. **145**(2): p. 183-205.

115. Campbell, F.R., *Ultrastructural studies of transmural migration of blood cells in the bone marrow of rats, mice and guinea pigs.* Am J Anat, 1972. **135**(4): p. 521-35.
116. WEISS, L., *Transmural Cellular Passage in Vascular Sinuses of Rat Bone Marrow.* Blood, 1970. **36**(2): p. 189-208.
117. Weiss, L., *The structure of bone marrow. Functional interrelationships of vascular and hematopoietic compartments in experimental hemolytic anemia: an electron microscopic study.* Journal of Morphology, 1965. **117**(3): p. 467-537.
118. Becker, I.C., et al., *G6b-B regulates an essential step in megakaryocyte maturation.* Blood Advances, 2022.
119. Vögtle, T., et al., *Heparan sulfates are critical regulators of the inhibitory megakaryocyte-platelet receptor G6b-B.* Elife, 2019. **8**: p. e46840.
120. Dominici, M., et al., *Restoration and reversible expansion of the osteoblastic hematopoietic stem cell niche after marrow radioablation.* Blood, 2009. **114**(11): p. 2333-2343.
121. Niswander, L.M., et al., *SDF-1 dynamically mediates megakaryocyte niche occupancy and thrombopoiesis at steady state and following radiation injury.* Blood, 2014. **124**(2): p. 277-86.
122. Pitchford, S.C., T. Lodie, and S.M. Rankin, *VEGFR1 stimulates a CXCR4-dependent translocation of megakaryocytes to the vascular niche, enhancing platelet production in mice.* Blood, The Journal of the American Society of Hematology, 2012. **120**(14): p. 2787-2795.
123. Pleines, I., et al., *Multiple alterations of platelet functions dominated by increased secretion in mice lacking Cdc42 in platelets.* Blood, The Journal of the American Society of Hematology, 2010. **115**(16): p. 3364-3373.
124. Pleines, I., et al., *Megakaryocyte-specific RhoA deficiency causes macrothrombocytopenia and defective platelet activation in hemostasis and thrombosis.* Blood, The Journal of the American Society of Hematology, 2012. **119**(4): p. 1054-1063.
125. Dutting, S., et al., *A Cdc42/RhoA regulatory circuit downstream of glycoprotein Ib guides transendothelial platelet biogenesis.* Nat Commun, 2017. **8**: p. 15838.
126. Avraham, H., et al., *Characterization of adhesive interactions between human endothelial cells and megakaryocytes.* J Clin Invest, 1993. **91**(6): p. 2378-84.
127. Lindblom, P., et al., *Endothelial PDGF-B retention is required for proper investment of pericytes in the microvessel wall.* Genes Dev, 2003. **17**(15): p. 1835-40.
128. Sixt, M., et al., *Endothelial cell laminin isoforms, laminins 8 and 10, play decisive roles in T cell recruitment across the blood-brain barrier in experimental autoimmune encephalomyelitis.* J Cell Biol, 2001. **153**(5): p. 933-46.
129. Campbell, S., et al., *Predictors of avascular necrosis of bone in long-term survivors of hematopoietic cell transplantation.* Cancer, 2009. **115**(18): p. 4127-4135.
130. Shusterman, S. and A.T. Meadows, *Long term survivors of childhood leukemia.* Current Opinion in Hematology, 2000. **7**(4): p. 217-222.
131. Vandoorne, K., et al., *Imaging the Vascular Bone Marrow Niche During Inflammatory Stress.* Circ Res, 2018. **123**(4): p. 415-427.
132. Honing, M.L., et al., *Bradykinin-induced vasodilation of human forearm resistance vessels is primarily mediated by endothelium-dependent hyperpolarization.* Hypertension, 2000. **35**(6): p. 1314-8.
133. Jeanne, M., J. Jorgensen, and D.B. Gould, *Molecular and genetic analyses of collagen type IV mutant mouse models of spontaneous intracerebral hemorrhage identify mechanisms for stroke prevention.* Circulation, 2015. **131**(18): p. 1555-1565.
134. Kuo, D.S., et al., *Allelic heterogeneity contributes to variability in ocular dysgenesis, myopathy and brain malformations caused by Col4a1 and Col4a2 mutations.* Human molecular genetics, 2014. **23**(7): p. 1709-1722.
135. Favor, J., et al., *Type IV procollagen missense mutations associated with defects of the eye, vascular stability, the brain, kidney function and embryonic or postnatal viability in the mouse, Mus musculus: an extension of the Col4a1 allelic series and the identification of the first two Col4a2 mutant alleles.* Genetics, 2007. **175**(2): p. 725-736.

136. Semeniak, D., *Role of bone marrow extracellular matrix proteins on platelet biogenesis and function.*Doctoral dissertation, 2018, p.70-71
137. MacDonald, I.C., et al., *Kinetics of red blood cell passage through interendothelial slits into venous sinuses in rat spleen, analyzed by in vivo microscopy.* Microvasc Res, 1987. **33**(1): p. 118-34.
138. De Bruyn, P.P. and Y. Cho, *Contractile structures in endothelial cells of splenic sinusoids.* J Ultrastruct Res, 1974. **49**(1): p. 24-33.
139. Galis, Z.S., et al., *Targeted disruption of the matrix metalloproteinase-9 gene impairs smooth muscle cell migration and geometrical arterial remodeling.* Circulation research, 2002. **91**(9): p. 852-859.
140. Colnot, C., et al., *Altered fracture repair in the absence of MMP9.* Development, 2003. **130**(17): p. 4123-4133.
141. Kyriakides, T.R., et al., *Mice that lack matrix metalloproteinase-9 display delayed wound healing associated with delayed reepithelization and disordered collagen fibrillogenesis.* Matrix biology : journal of the International Society for Matrix Biology, 2009. **28**(2): p. 65-73.
142. Pelus, L.M., et al., *Neutrophil-derived MMP-9 mediates synergistic mobilization of hematopoietic stem and progenitor cells by the combination of G-CSF and the chemokines GRObeta/CXCL2 and GRObetaT/CXCL2delta4.* Blood, 2004. **103**(1): p. 110-9.
143. King, A.G., et al., *Rapid mobilization of murine hematopoietic stem cells with enhanced engraftment properties and evaluation of hematopoietic progenitor cell mobilization in rhesus monkeys by a single injection of SB-251353, a specific truncated form of the human CXC chemokine GRObeta.* Blood, 2001. **97**(6): p. 1534-42.
144. Frenette, P.S., et al., *Susceptibility to infection and altered hematopoiesis in mice deficient in both P- and E-selectins.* Cell, 1996. **84**(4): p. 563-74.
145. Nabors, L.K., et al., *Overlapping roles for endothelial selectins in murine hematopoietic stem/progenitor cell homing to bone marrow.* Experimental hematology, 2013. **41**(7): p. 588-596.
146. Papayannopoulou, T., et al., *The VLA4/VCAM-1 adhesion pathway defines contrasting mechanisms of lodgement of transplanted murine hemopoietic progenitors between bone marrow and spleen.* Proc Natl Acad Sci U S A, 1995. **92**(21): p. 9647-51.
147. Scott, L.M., G.V. Priestley, and T. Papayannopoulou, *Deletion of alpha4 integrins from adult hematopoietic cells reveals roles in homeostasis, regeneration, and homing.* Mol Cell Biol, 2003. **23**(24): p. 9349-60.
148. Timo, R., et al., *Hematopoietic stem and progenitor cells use podosomes to transcellularly cross the bone marrow endothelium.* Haematologica, 2020. **105**(12): p. 2746-2756.
149. Semerad, C.L., et al., *G-CSF potently inhibits osteoblast activity and CXCL12 mRNA expression in the bone marrow.* Blood, 2005. **106**(9): p. 3020-3027.
150. Urao, N. and M. Ushio-Fukai, *Redox regulation of stem/progenitor cells and bone marrow niche.* Free radical biology & medicine, 2013. **54**: p. 26-39.
151. Itkin, T., et al., *Distinct bone marrow blood vessels differentially regulate haematopoiesis.* Nature, 2016. **532**(7599): p. 323-328.
152. Shen, H., et al., *An acute negative bystander effect of γ-irradiated recipients on transplanted hematopoietic stem cells.* Blood, 2012. **119**(15): p. 3629-37.
153. Girbl, T., et al., *Distinct Compartmentalization of the Chemokines CXCL1 and CXCL2 and the Atypical Receptor ACKR1 Determine Discrete Stages of Neutrophil Diapedesis.* Immunity, 2018. **49**(6): p. 1062-1076.e6.
154. Adeli, E.K., et al., *Effects of CXCR1 and CXCR2 inhibition on expansion and differentiation of umbilical cord blood CD133+ cells into megakaryocyte progenitor cells.* Cytokine, 2011. **55**(2): p. 181-187.
155. Tsou, C.-L., et al., *Critical roles for CCR2 and MCP-3 in monocyte mobilization from bone marrow and recruitment to inflammatory sites.* The Journal of clinical investigation, 2007. **117**(4): p. 902-909.

156. Schenk, S., et al., *Monocyte chemotactic protein-3 is a myocardial mesenchymal stem cell homing factor.* Stem Cells, 2007. **25**(1): p. 245-51.
157. Huang, B., et al., *Osteoblasts secrete Cxcl9 to regulate angiogenesis in bone.* Nature Communications, 2016. **7**(1): p. 13885.
158. Verbiest, T., et al., *NOD Scid Gamma Mice Are Permissive to Allogeneic HSC Transplantation without Prior Conditioning.* International journal of molecular sciences, 2016. **17**(11): p. 1850.
159. Tijssen, M.R., et al., *Transplantation of human peripheral blood CD34-positive cells in combination with ex vivo generated megakaryocytes results in fast platelet formation in NOD/SCID mice.* Leukemia, 2008. **22**(1): p. 203-208.
160. Bruno, S., et al., *Fast But Durable Megakaryocyte Repopulation and Platelet Production in NOD/SCID Mice Transplanted with Ex-Vivo Expanded Human Cord Blood CD34+ Cells.* Stem Cells, 2004. **22**(2): p. 135-143.
161. Pasquini, M.C., et al., *Comparative outcomes of donor graft CD34+ selection and immune suppressive therapy as graft-versus-host disease prophylaxis for patients with acute myeloid leukemia in complete remission undergoing HLA-matched sibling allogeneic hematopoietic cell transplantation.* J Clin Oncol, 2012. **30**(26): p. 3194-201.
162. Lang, P., et al., *Transplantation of CD3/CD19 depleted allografts from haploidentical family donors in paediatric leukaemia.* Br J Haematol, 2014. **165**(5): p. 688-98.
163. van Hensbergen, Y., et al., *Ex vivo culture of human CD34+ cord blood cells with thrombopoietin (TPO) accelerates platelet engraftment in a NOD/SCID mouse model.* Experimental hematology, 2006. **34**(7): p. 943-950.
164. Angelopoulou, M., et al., *Cotransplantation of human mesenchymal stem cells enhances human myelopoiesis and megakaryocytopoiesis in NOD/SCID mice.* Experimental Hematology, 2003. **31**(5): p. 413-420.
165. Kim, H.Y., et al., *Romiplostim-related myelofibrosis in refractory primary immune thrombocytopenia: A Case report.* Medicine (Baltimore), 2019. **98**(25): p. e15882.
166. Kuter, D.J., et al., *Evaluation of bone marrow reticulin formation in chronic immune thrombocytopenia patients treated with romiplostim.* Blood, 2009. **114**(18): p. 3748-3756.
167. Liu, C., et al., *Characterization of cellular heterogeneity and an immune subpopulation of human megakaryocytes.* Advanced Science, 2021. **8**(15): p. 2100921.
168. Heemskerk, J.W.M. and J. West, *Emerging Technologies for Understanding Platelet Diversity.* Arteriosclerosis, Thrombosis, and Vascular Biology, 2022. **42**(5): p. 540-552.
169. Jiang, Y., N.R. Zhang, and M. Li, *SCALE: modeling allele-specific gene expression by single-cell RNA sequencing.* Genome Biology, 2017. **18**(1): p. 74.
170. Nagy, M., et al., *Variable impairment of platelet functions in patients with severe, genetically linked immune deficiencies.* Haematologica, 2018. **103**(3): p. 540-549.
171. Campbell, R.A., et al., *Human megakaryocytes possess intrinsic antiviral immunity through regulated induction of IFITM3.* Blood, 2019. **133**(19): p. 2013-2026.
172. Middleton, E.A., et al., *Sepsis alters the transcriptional and translational landscape of human and murine platelets.* Blood, 2019. **134**(12): p. 911-923.
173. Weiss, L.J., et al., *Acquired platelet GPVI receptor dysfunction in critically ill patients with sepsis.* Blood, The Journal of the American Society of Hematology, 2021. **137**(22): p. 3105-3115.
174. Yin, F., et al., *The bone marrow niche components are adversely affected in sepsis.* Molecular Biomedicine, 2020. **1**(1): p. 10.
175. Artoni, A., et al., *Hemostatic abnormalities in patients with Ehlers–Danlos syndrome.* Journal of Thrombosis and Haemostasis, 2018. **16**(12): p. 2425-2431.
176. Estes, J.W., *Platelet abnormalities in heritable disorders of connective tissue.* Annals of the New York Academy of Sciences, 1972. **201**(1): p. 445-450.
177. Gooijer, K., et al., *Bleeding and bruising in Osteogenesis Imperfecta: International Society on Thrombosis and Haemostasis bleeding assessment tool and haemostasis laboratory assessment in 22 individuals.* Br J Haematol, 2019. **187**(4): p. 509-517.
178. Abbonante, V., et al., *Ablation of collagen VI leads to the release of platelets with altered function.* Blood Advances, 2021. **5**(23): p. 5150-5163.

6. Appendix

6.1. Supplemental data

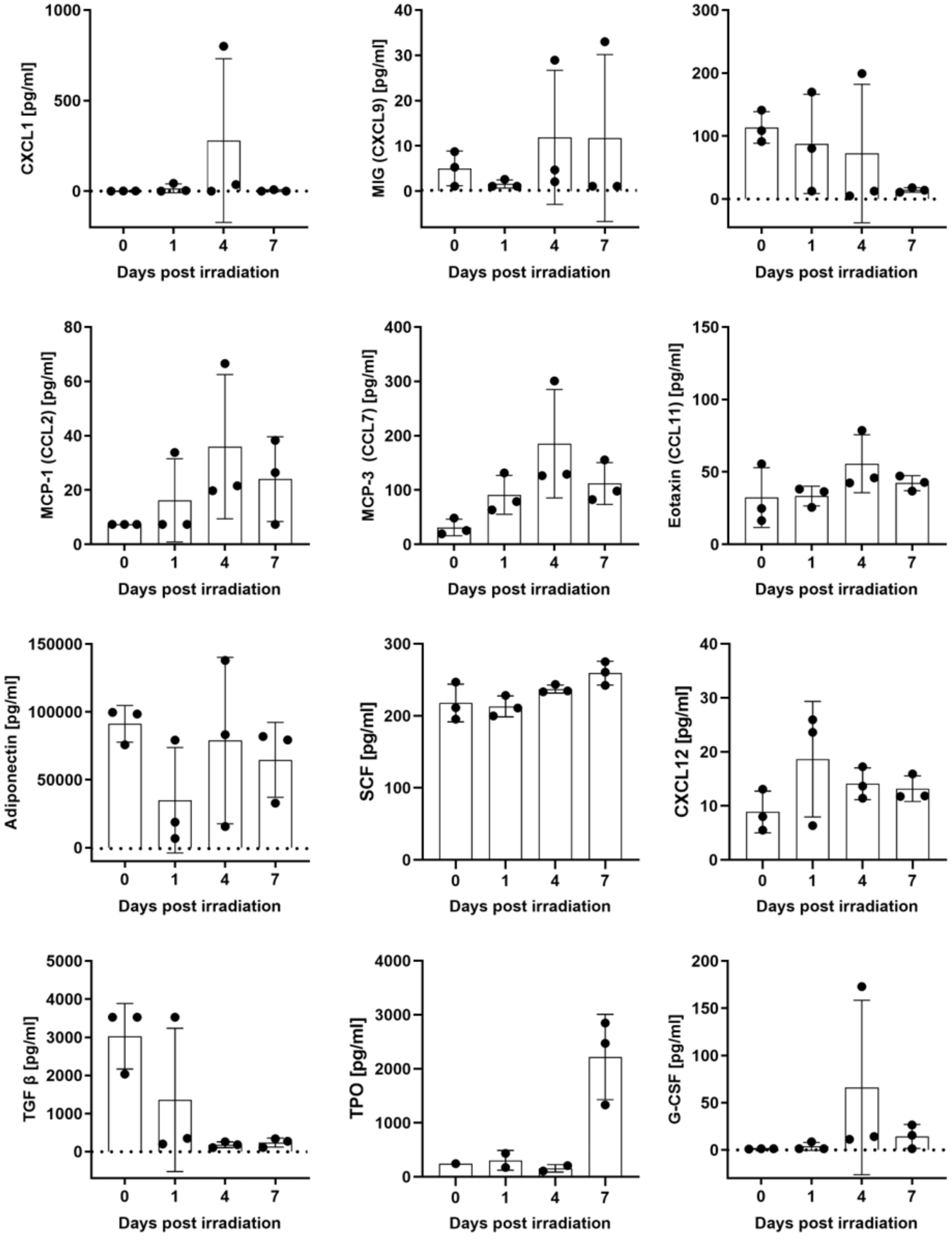

Fig. 35. Chemokine expression after sublethal (5 Gy) TBI. Data is presented as mean ± SD. n=3.

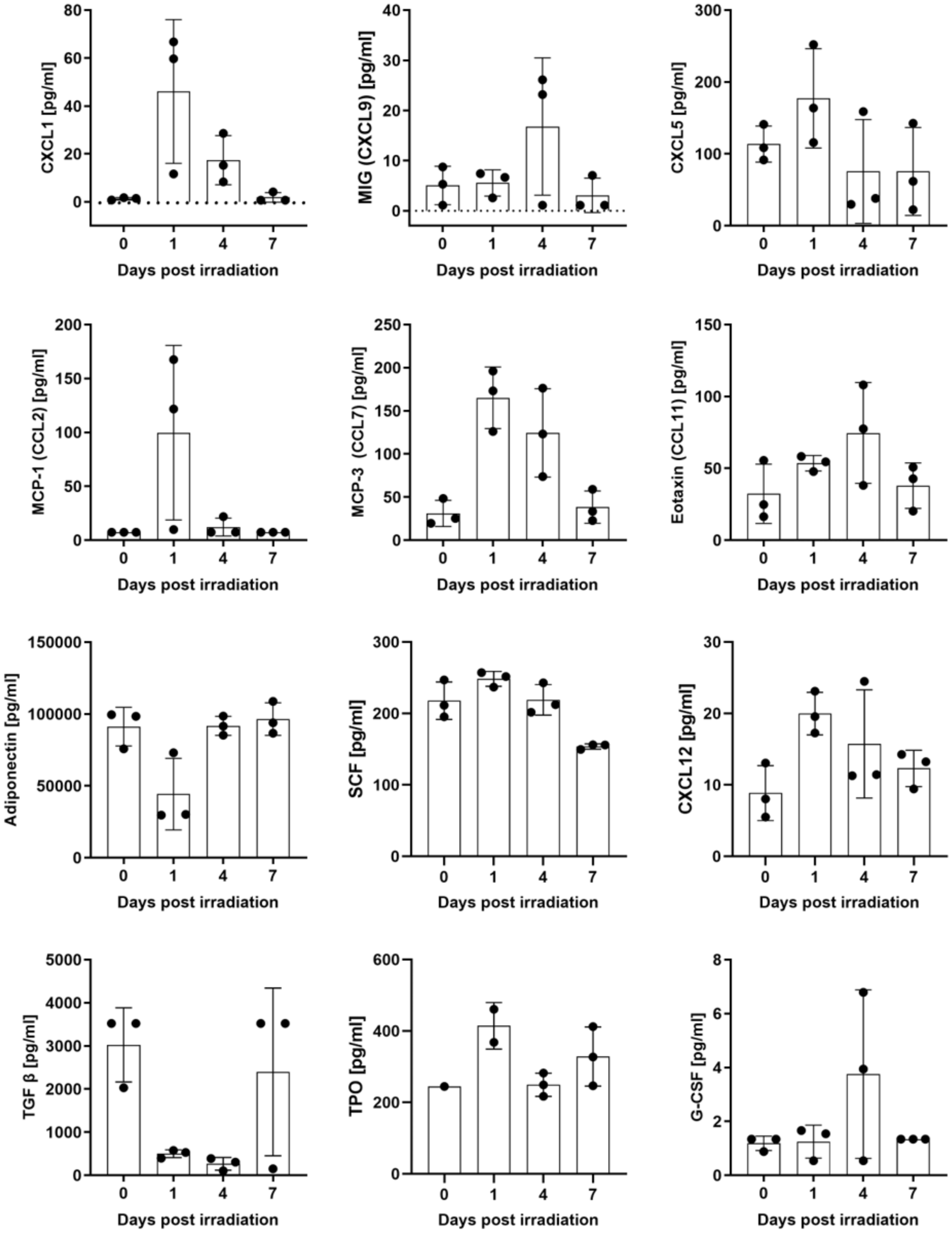

Fig. 36. Chemokine expression after lethal (10 Gy) TBI. Data is presented as mean ± SD. n=3.

6.2. Abbreviations

2D	Two-dimensional
3D	Three-dimensional
5-FU	5-fluorouracil
ACKR3	Atypical chemokine receptor 3
ADP	Adenosine diphosphate
AGM	Aorta-gonad mesonephros
ALL	Acute lymphoblastic leukemia
APMA	p-aminophenylmercuric acetate
APS	Ammonium persulfate
BABB	Benzylalcohol benzylbenzoate
BM	Bone marrow
bp	Base pair
BSA	Bovine serum albumin
CAMT	Congenital amegakaryocytic thrombocytopenia
CAR cell	CXCL12-abundant reticular cell
CCL	CC-motif chemokine ligand
CLEC-2	C-type lectin-like receptor 2
CLP	Common lymphoid progenitor
CLSM	Confocal laser scanning microscopy
CML	Chronic myeloid leukemia
CMP	Common myeloid progenitor
c-Mpl	Myeloproliferative leukemia virus oncogene
CRP-X_L	Collagen related peptide
CXCL	CXC-chemokine ligand
CXCR	CXC chemokine receptor
DAPI	4’, 6-diamidino-2-phenylindole
DDR-1	Discoidin domain receptor 1
DMEM	Dulbecco’s Modified Eagle Medium
DMS	Demarcation membrane system
dNTP	Deoxynucleotide triphosphates
DQ	Dye quenched

dsRed	Discosoma red fluorescent protein
EBMT	European Society for Blood and Marrow Transplantation
EC	Endothelial cell
ECL	Enhanced chemoluminescence
ECM	Extracellular matrix
EDTA	Ethylenediaminetetraacetic acid
EGTA	Ethylene glycol tetra-acetic acid
ELISA	Enzyme-linked immunosorbent assay
Ery	Erythroid
FACS	Fluorescence-activated cell sorting
FcR	Fc receptor
FCS	Fetal calf serum
FITC	Fluorescein
FORUM	For Omitting Radiation Under Majority age study
FSC	Forward scatter
GFP	Green fluorescent protein
GMP	Granulocyte macrophage progenitor
GP	Glycoprotein
GPO	Glycine-proline-hydroxyproline
GvHD	Graft versus host disease
HCT	Hematocrit
HEPES	4-(2-hydroxyethyl)-1-piperazineethanesulfonic acid
HGB	Hemoglobin
HRP	Horseradish peroxidase
HSC	Hematopoietic stem cell
HSCT	Hematopoietic stem cell transplantation
ITAM	Immunoreceptor tyrosine-based activation motif
ITP	Immune thrombocytopenic purpura
JAK	Janus kinase
LAIR-1	Leukocyte-associated immunoglobulin-like receptor 1
LAT	Linker of activated T-cells
LepR	Leptin receptor
LSFM	Light sheet fluorescence microscopy

MCH	Mean corpuscular hemoglobin
MCHC	Mean corpuscular hemoglobin concentration
MCP3	Monocyte-chemotactic protein 3
MCV	Mean corpuscular volume
MEP	Megakaryocyte erythroid progenitor
MFI	Mean fluorescence intensity
MK	Megakaryocyte
MMP	Matrix metalloproteinase
MPP	Multipotent progenitor
MPV	Mean platelet volume
MyRP	Megakaryocyte and myeloid-restricted progenitor
NG2	Neural-glial antigen 2
NMA/RIC	Non-myeloablative/reduced intensity conditioning
NOD/SCID	Non-obese diabetic/severe combined immunodeficient
PBS	Phosphate buffered saline
PBSC	Peripheral blood stem cells
PCR	Polymerase chain reaction
PE	Phycoerythrin
PFA	Paraformaldehyde
PGI2	Prostacyclin
PI	Phosphatidylinositol
PI3K	Phosphatidylinositol 3 kinases
PLCγ2	Phospholipase Cγ2
PLP	Platelet-like particles
PPF	Proplatelet formation
PRP	Platelet-rich-plasma
RBC	Red blood cell count
RC	Reticular cell
RDW	Red blood cell distribution width
rpm	Rotations per minute
RT	Room temperature
SBF-SEM	Serial-blockface scanning electron microscopy
SCF	Stem cell factor

SD	Standard deviation
SDS-PAGE	Sodium dodecyl sulfate polyacrylamide gel electrophoresis
SEC	Sinusoidal endothelial cell
SFKs	Src family kinases
SOS	Sinsusoidal obstruction syndrome
SSC	Side scatter
Syk	Spleen tyrosine kinase
TAE	TRIS acetate EDTA
TAR	Thrombocytopenia with absent radii
TA-TMA	Transplant-associated thrombotic microangiopathy
TBI	Total body irradiation
TBS-T	TRIS-buffered saline containing Tween
TEM	Transmission electron microscopy
TEMED	Tetramethylethylendiamine
TPO	Thrombopoietin
TRIS	Tris(hydroxymethyl)aminomethane
VCAM	Vascular cell adhesion molecule
VEGF	Vascular endothelial growth factor
VLA	Very late antigen
VTE	Venous thromboembolism
vWF	Von Willebrand factor
WBC	White blood cell count

6.3. Acknowledgements

The work presented here was completed at the Institute of Experimental Biomedicine I, University Hospital Würzburg, in the group of Prof. Harald Schulze. During my time as a PhD student from 2018 to 2022, many people helped and supported me, and I would like to thank especially the following persons:

- My supervisor Prof. Harald Schulze, for giving me the opportunity to work on this exciting topic, for helping me to develop this project and myself as a scientist, who always encouraged me and my own ideas and for always having my back.

- My thesis committee members Prof. Katrin Heinze and Prof. Süleyman Ergün for fruitful discussions and great scientific input.

- Prof. Bernhard Nieswandt, who enabled me to benefit from all the advantages of a large research institute.

- Nadine Winter, for supporting me with her excellent technical assistance and who made working in the lab together funnier.
- Our cooperation partners Prof. Nicolas Schlegel, Mariola Dragan, Dr. Zoltan Nagy and PD Dr. Nicole Wagner who helped with great experimental support.

- Markus Spindler, Juliane Baumann and Lukas Weiß, with whom I could share failures but also successes and who provided a very enjoyable working atmosphere.

- All past and present members of the institute.

- Finally, my family, friends, and especially my husband Claus, who supported me since school time. Without you I would not be where I am today.

6.4. Curriculum vitae

Publications

First author publication

Wagner N*, **Mott K***, Upcin B., Stegner D., Schulze H., & Ergün S. CXCL12-Abundant Reticular (CAR) Cells Direct Megakaryocyte Protrusions across the Bone Marrow Sinusoid Wall. Cells (2021)

Co-author publications

Semeniak D., **Faber K**., Öftering P., Manukjan G., & Schulze H. Impact of Itga2-Gp6-double collagen receptor deficient mice for bone marrow megakaryocytes and platelets. PloS one (2019).

Becker I. C., Nagy Z., Manukjan G., Haffner-Luntzer M., Englert M., Heib T., Vögtle T., Gross C., Bharti R., Dietrich S., **Mott K**., Heck J., Jeschke A., Schinke T., Schlegel N., Heckel T., Stegner D., Pleines I., Ignatius A., Schulze H. & Nieswandt B. G6b-B regulates an essential step in megakaryocyte maturation. Blood Advances (2022).

Englert M., Aurbach K., Becker I. C., Gerber A., Heib T., Wackerbarth L. M., Kusch C., **Mott K.,** Araujo G. H. M., Baig A. A., Dütting S., Knaus U. G., Stigloher C., Schulze H., Nieswandt B., Pleines I., & Nagy Z. Impaired microtubule dynamics contribute to microthrombocytopenia in RhoB-deficient mice. Blood Advances (2022).

International oral presentation

“Megakaryocyte Engraftment and altered Platelet Function in a Murine Model of Hematopoietic Stem Cell Transplantation”. 30th Congress of the International Society on Thrombosis and Haemostasis (ISTH); July 2022, London, UK

International poster presentations

“Impaired platelet function after total body irradiation in a mouse model of hematopoietic stem cell transplantation” 66th Annual Meeting of the Society of Thrombosis and Haemostasis Research e. V. (GTH); March 2022, Leipzig, Germany

“The role of Matrix-Metalloproteinase 9 in Bone Marrow Remodeling after Total Body Irradiation and Hematopoietic Stem Cell Transplantation” 29th Congress of the International Society on Thrombosis and Haemostasis (ISTH); July 2021, Philadelphia, USA

“Impact of irradiation on the bone marrow matrix and megakaryopoiesis” 28th Congress of the International Society on Thrombosis and Haemostasis (ISTH); July 2020, Milan, Italy

“Impact of irradiation on the bone marrow matrix” 19th International Eureka! Symposium, October 2019, Würzburg, Germany

International award

Young investigator award from the 30th Congress of the International Society on Thrombosis and Haemostasis (ISTH) for the highly rated abstract: “Megakaryocyte Engraftment and altered Platelet Function in a Murine Model of Hematopoietic Stem Cell Transplantation.” July 2022, London, UK

6.5. Affidavit

I hereby confirm that my thesis entitled “Regulation of platelet biogenesis in the native and myeloablated bone marrow niche” is the result of my own work. I did not receive any help or support from commercial consultants. All sources and/or materials applied are listed and specified in the thesis.

Furthermore, I confirm that this thesis has not yet been submitted as part of another examination process neither in identical nor in similar form.

Würzburg, July 2022 ___________________________________

Kristina Mott

Eidesstattliche Erklärung

Hiermit erkläre ich an Eides statt, die Dissertation „Die Regulation der Thrombozytenbiogenese im nativen und myeloablatierten Knochenmark“ eigenständig, d.h. insbesondere selbständig und ohne Hilfe eines kommerziellen Promotionsberaters, angefertigt und keine anderen als die von mir angegebenen Quellen und Hilfsmittel verwendet zu haben.

Ich erkläre außerdem, dass die Dissertation weder in gleicher noch in ähnlicher Form bereits in einem anderen Prüfungsverfahren vorgelegen hat.

Würzburg, Juli 2022 ___________________________________

Kristina Mott